

**Foreground Detection with the DRAO Synthesis Telescope:
Methods and Models to Measure the
Polarized Cosmic Microwave Background**

by

Anastasia Baran

A Thesis submitted to the Faculty of Graduate Studies of
The University of Manitoba
in partial fulfilment of the requirements of the degree of

Master of Science

Department of Physics and Astronomy
University of Manitoba
Winnipeg, Manitoba, Canada

Copyright © 2009 Anastasia Baran

THE UNIVERSITY OF MANITOBA
FACULTY OF GRADUATE STUDIES

COPYRIGHT PERMISSION

**Foreground Detection with the DRAO Synthesis Telescope:
Methods and Models to Measure the
Polarized Cosmic Microwave Background**

By

Anastasia Baran

A Thesis/Practicum submitted to the Faculty of Graduate Studies of The University of
Manitoba in partial fulfillment of the requirement of the degree

Of

Master of Science

Anastasia Baran©2009

Permission has been granted to the University of Manitoba Libraries to lend a copy of this thesis/practicum, to Library and Archives Canada (LAC) to lend a copy of this thesis/practicum, and to LAC's agent (UMI/ProQuest) to microfilm, sell copies and to publish an abstract of this thesis/practicum.

This reproduction or copy of this thesis has been made available by authority of the copyright owner solely for the purpose of private study and research, and may only be reproduced and copied as permitted by copyright laws or with express written authorization from the copyright owner.

1. Reviewer: Dr. A. R. Taylor

2. Reviewer: Dr. T. Foster

3. Reviewer: Dr. J. Fiege

4. Reviewer: Dr. W. Kocay

Day of the defense: October 13, 2009

Abstract

The ELAIS N-1 deep field is a low column density window into the extragalactic universe. The diffuse galactic foreground of this window must be understood in order to measure anisotropies in the Cosmic Background Radiation Field - a principal goal of the Planck science team. The Dominion Radio Astrophysical Observatory (DRAO) synthesis telescope can be used to distinguish low-level signal from noise in order to map the galactic foreground and improve the accuracy of the Planck CMB measurements. This is accomplished by modeling system temperature noise for the synthesis telescope in order to create a noise map, which allows positive detection of the low-level polarization features that exist in the field. This difficult non-linear optimization problem does not lend itself well to standard local optimization techniques. We have developed software, based on an advanced genetic algorithm (Ferret), to characterize the spatial distribution of noise power in synthesis telescope mosaic images.

For Willy

Acknowledgements

This research would not have been possible without my supervisors, who despite spanning the country seemed to be down the hall. Russ Taylor, for his guidance and kindness and for allowing me to work on such an interesting and challenging project. Tyler Foster for introducing me to astronomy in a most meaningful way (Road Trip!!!), and Jason Fiege for participating in the graduate student adoption process.

Thanks to Julie Grant for being my Calgary counterpart, and my friend, and for providing me with processed data for my research. Also, for all of the guidance and teaching, thanks to Jeroen Stil, without whom this project wouldn't exist.

I would like to thank Roland Kothes, Andrew Gray and Ryan Ransom at DRAO who were present throughout this project and never hesitated to lend a helping hand. I would especially like to thank Tom Landecker for not only being a constant source of information and insight into this project but for agreeing to take me on as a Ph.D. student and allowing me to continue in a field that I love.

I would also like to thank my parents. I promise I'll have a real job someday.

Contents

List of Figures	v
List of Tables	ix
1 Introduction	1
1.1 The Cosmic Microwave Background	2
1.2 The Planck Mission	3
1.3 The ELAIS-N1 Deep Field Survey	4
1.4 Polarization	5
1.5 The DRAO Synthesis Telescope	6
1.5.1 Noise Properties of an Interferometer	8
2 Techniques	11
2.1 Aperture Synthesis	11
2.2 Genetic Algorithms	13
2.3 Ferret	15
2.4 Data	16
2.5 Detecting Foregrounds	16
2.5.1 Deriving System Temperature	16
2.5.2 Bootstrap Monte Carlo Method	17
2.5.3 Noise Characterization in Short Spacings	18
2.5.4 Mosaics	19
2.5.5 Creating Images	19
2.5.6 Mosaic Analysis	19
2.6 Creating and Analyzing Images	20
2.7 Software Outline	20
2.7.1 Initial Setup: init_AllFields.m, DRAO_Constants.m, and CalcVisData.m .	20
2.7.2 Fitting Process: ComputePower.m, fitness.m	22

CONTENTS

2.7.3	Post Processing, makeImage.m	22
2.7.3.1	Making Mosaics	23
2.8	Summary	23
3	Results	25
3.1	Ferret System Temperature Results	25
3.2	Mosaics	28
3.3	Validation of Technique: Trials with other Optimizers	39
3.3.1	Locust	39
3.3.2	Anvil and SAMOSA	41
3.4	Power Spectra: Stokes Q	43
3.5	Power Spectra: Stokes U	51
3.6	Ferret Solution Surfaces: Stokes Q	59
3.7	Ferret Solution Surfaces: Stokes U	67
3.8	Model Fitness Plots: Stokes Q	75
3.9	Model Fitness Plots: Stokes U	83
4	Discussion	91
4.1	CMB Foregrounds in ELAIS-N1	91
4.1.1	Confidence in Results	92
4.2	Versatility of Software and Future Work	93
4.2.1	Other Synthesis Telescopes	95
4.2.2	DRAO Data	95
4.2.3	Square Kilometer Array	95
4.3	Conclusions and Summary	96
	References	97
5	Appendix	99
5.1	System Temperature Derivation Code	99

List of Figures

1.1	ELAIS-N1	4
1.2	The DRAO synthesis array	6
1.3	Frequency bands	7
2.1	The DRAO synthesis telescope	12
2.2	The relationship between the uv-plane and the image plane	14
2.3	Ferret environment	15
2.4	Ferret solution surface and data histogram	17
2.5	Noise at Short Spacings	18
3.1	Stokes Q synthesized mosaic	29
3.2	30 Field ELAIS-N1 mosaic in Stokes Q with positive point sources removed . . .	30
3.3	30 Field ELAIS-N1 mosaic in Stokes Q with negative point sources removed . . .	31
3.4	Stokes Q power spectra where the spectrum of the real data has positive point sources removed. Note the red line is the data mosaic and the blue line is the synthetic mosaic.	32
3.5	Stokes Q power spectra where the spectrum of the real data has negative point sources removed. Note the red line is the data mosaic and the blue line is the synthetic mosaic.	33
3.6	Stokes U synthesized mosaic	34
3.7	30 Field ELAIS-N1 mosaic in Stokes U with positive point sources removed . . .	35
3.8	30 Field ELAIS-N1 mosaic in Stokes U with negative point sources removed . . .	36
3.9	Stokes U power spectra where the spectrum of the real data has positive point sources removed. Note the red line is the data mosaic and the blue line is the synthetic mosaic.	37

LIST OF FIGURES

3.10 Stokes U power spectra where the spectrum of the real data has negative point sources removed. Note the red line is the data mosaic and the blue line is the synthetic mosaic.	38
3.11 Locust and Anvil optimizers	41
3.12 Comparison of power spectra EN02-EN05, Stokes Q	43
3.13 Comparison of power spectra EN06-EN09, Stokes Q.	44
3.14 Comparison of power spectra EN10-EN13, Stokes Q.	45
3.15 Comparison of power spectra EN14-EN17, Stokes Q.	46
3.16 Comparison of power spectra EN18-EN21, Stokes Q.	47
3.17 Comparison of power spectra EN22-EN24, Stokes Q.	48
3.18 Comparison of power spectra EN25-EN27, Stokes Q.	49
3.19 Comparison of power spectra EN28-EN30, Stokes Q.	50
3.20 Comparison of power spectra EN2-EN5, Stokes U	51
3.21 Comparison of power spectra EN06-EN09, Stokes U.	52
3.22 Comparison of power spectra EN10-EN13, Stokes U.	53
3.23 Comparison of power spectra EN14-EN17, Stokes U.	54
3.24 Comparison of power spectra EN18-EN21 Stokes U.	55
3.25 Comparison of power spectra EN22-EN24, Stokes U.	56
3.26 Comparison of power spectra EN25-EN27, Stokes U.	57
3.27 Comparison of power spectra EN28-EN30, Stokes U.	58
3.28 Family of solutions EN02-EN05, Stokes Q.	59
3.29 Family of solutions EN06-EN09, Stokes Q.	60
3.30 Family of solutions EN10-EN13, Stokes Q.	61
3.31 Family of solutions EN14-EN17, Stokes Q.	62
3.32 Family of solutions EN18-EN21, Stokes Q.	63
3.33 Family of solutions EN22-EN24, Stokes Q.	64
3.34 Family of solutions EN25-EN27, Stokes Q.	65
3.35 Family of solutions EN28-EN30, Stokes Q.	66
3.36 Family of solutions EN02-EN05, Stokes U.	67
3.37 Family of solutions EN06-EN09, Stokes U.	68
3.38 Family of solutions EN10-EN13, Stokes U.	69
3.39 Family of solutions EN14-EN17, Stokes U.	70
3.40 Family of solutions EN18-EN21, Stokes U.	71
3.41 Family of solutions EN22-EN24, Stokes U.	72
3.42 Family of solutions EN25-EN27, Stokes U.	73

LIST OF FIGURES

3.43	Family of solutions EN28-EN30, Stokes U.	74
3.44	Visibility fitness plot EN02-EN05, Stokes Q. The plot shows the final result of the model (blue) fitting data (red).	75
3.45	Visibility fitness plot EN06-EN09, Stokes Q.	76
3.46	Visibility fitness plot EN10-EN13, Stokes Q.	77
3.47	Visibility fitness plot EN14-EN17, Stokes Q.	78
3.48	Visibility fitness plot EN18-EN21, Stokes Q.	79
3.49	Visibility fitness plot EN22-EN24, Stokes Q.	80
3.50	Visibility fitness plot EN25-EN27, Stokes Q.	81
3.51	Visibility fitness plot EN28-EN30, Stokes Q.	82
3.52	Visibility fitness plot EN02-EN05, Stokes U.	83
3.53	Visibility fitness plot EN06-EN09, Stokes U.	84
3.54	Visibility fitness plot EN10-EN13, Stokes U.	85
3.55	Visibility fitness plot EN14-EN17, Stokes U.	86
3.56	Visibility fitness plot EN18-EN21, Stokes U.	87
3.57	Visibility fitness plot EN22-EN24, Stokes U.	88
3.58	Visibility fitness plot EN25-EN27, Stokes U.	89
3.59	Visibility fitness plot EN28-EN30, Stokes U.	90
4.1	Removing baselines	93

LIST OF FIGURES

List of Tables

3.1	Ferret system temperature results: Stokes Q	26
3.2	Ferret system temperature results: Stokes U	27
3.3	Locust system temperature results: Stokes Q	40
3.4	Locust system temperature results: Stokes U	40
3.5	SAMOSa system temperature results: Stokes U	42
3.6	Anvil system temperature results: Stokes U	42
4.1	Testing the fitting process	94

Introduction

Since its discovery in 1964, the Cosmic Microwave Background (CMB), a field of electromagnetic radiation which fills the universe, has been essential to Big Bang theory. The presence of this radiation field, which emits most strongly in the microwave region, has been vital in supporting early Universe theories. The Universe shortly after time zero can be described by an extremely hot (4000K to 3000K) plasma-filled space from which photons escaped as the Universe cooled. This cooling began as the rapid expansion of space at time 10^{-43} s. Current data suggests that inflation, or something similar, occurred during the evolution of the Universe as we know it. These photons now present themselves as the CMB which is nearly isotropically present throughout space (1).

The Planck satellite has been launched by the European Space Agency with the intention of providing the most accurate CMB study to date. Planck will measure both the temperature and polarization properties of the CMB, which have been shown to correlate in previous observations (2). This study, along with the European Large Area ISO Survey N1 (ELAIS-N1) deep field survey which has been carried out at the Dominion Radio Astrophysical Observatory, can provide us with essential foreground information to improve the accuracy of Planck's CMB measurements. Using these tools to study the CMB will potentially provide the most accurate picture of the early Universe to date (3).

1.1 The Cosmic Microwave Background

The Big Bang model predicts that small fluctuations in the early universe have grown into the large scale structure that we see today. Under this model, we can unfold primordial fluctuations in the early Universe by measuring the temperature anisotropies around us. If we are indeed measuring fluctuations in the early Universe, this means that the temperature anisotropies were present at last scattering and we are able to observe a polarized CMB (2).

Scientists have measured polarization features in the CMB, meaning that we have some certainty that our predictors stand, but there are still several things that an accurate study of CMB polarization could tell us. These are the science goals of the Planck CMB project, which are outlined in the next section.

The polarized components of the CMB exist in E-mode and B-mode polarization. Theorists state that E mode polarization arises naturally from the Thomson scattering in an inhomogeneous plasma. In the CMB case, the E-modes are detections of the remnants of last-scattering.

B-mode polarization has a vanishing curl, and a maximum amplitude of $0.1\mu\text{K}$. It is believed that B-modes are determined by the density of gravitational waves in the primordial plasma which existed before inflation. This type of polarization has not yet been detected because of technological restrictions. Detection would require sensitivities lower than $1\mu\text{K}$ at frequencies around 70GHz (where the Galactic synchrotron signal is ten times this value) (4). B-modes give us vital information of the early Universe and would provide support for current inflation theories.

The gravitational waves that B-mode polarization would allow us to detect should exist everywhere in the Universe. These waves would have been created in the primordial plasma when gravitons came into existence but were pulled apart by inflation before being annihilated by an anti-particle. At this time, virtual gravitons became real gravitons and, as the Universe expanded, the gravitational waves were stretched to large wavelengths.

Gravitational waves would be useful to astronomers because they are not absorbed by media as are other types of radiation, meaning that gravitational waves would allow us to observe previously undetectable objects. This is also true of the early Universe. Gravitational waves produced during the Big Bang would not be impeded by anything in the early Universe plasma, making them the clearest record of the Universe after the Big Bang. Measuring the polarization of the CMB allows us to ‘see’ these waves because there was nothing else present in the early universe that had the ability to polarize radiation. The mass anisotropies had no left or right hand orientations, meaning that gravitational waves, which propagate in a screw motion, must have polarized the CMB (5).

1.2 The Planck Mission

Planck, a European Space Agency satellite, was launched in May 2009 to measure CMB anisotropies in both temperature and polarization. The third mission of its kind after COBE and WMAP, Planck is designed to collect data with improved sensitivity and angular resolution to create the most accurate CMB maps to date. New implications for cosmological science include (1):

- Improved test of early Universe models
- Accurate estimates of cosmological parameters
- Test of non-Gaussianity in CMB fluctuations
- New secondary science probes (eg. lensing, dark energy)
- Measurements of polarization power spectra

Early polarization measurements of the CMB have been consistent with the predicted level, supporting the case for adiabatic perturbations in the decoupling era of cosmology as well as reinforcing inflation. However, current CMB polarization data does not begin to match the certainty of the temperature data. For example, WMAP has an angular resolution of 14 arcmin while Planck has a resolution of 5 arcmin, and while WMAP had only five frequency channels, Planck is able to measure in nine. This makes the addition of Planck data exceptionally valuable to early universe cosmology, with the first possibility of measuring B-mode polarization (2).

Knowledge of the Galactic foreground is invaluable to CMB scientists. The higher the accuracy of the foreground determination, the higher the accuracy of the CMB measurement itself. At 50 GHz, Planck is equipped with an onboard foreground detector which is capable of 3 arcmin resolution. For the purpose of foreground study, a group of Canadian scientists, using the Dominion Radio Astrophysical Observatory, launched the DRAO Planck deep fields (DPDF) project in preparation for the Planck mission. This foreground study, which uses data with one arcminute resolution, is the main goal of this project, with the intention of aiding Planck in increasing the accuracy of its polarization measurements.

Full details of Planck construction and measurement capabilities in polarization can be found in the Planck primer (1).

1. INTRODUCTION

1.3 The ELAIS-N1 Deep Field Survey

The European Large Area ISO Survey N1 (ELAIS-N1) deep field is a window into the extragalactic universe, containing very low amounts of Galactic emission (6). The field is located at 50 degrees Galactic latitude and 80 degrees Galactic longitude. A Survey of this field was carried out by the Dominion Radio Astrophysical Observatory (DRAO) synthesis telescope in 1420MHz HI, total intensity, and Stokes Q and U. The deep field consist of 40 fields (30 of which are considered for this project) which are spaced very close together and observed for long integration times, providing high sensitivity for a small region of sky.

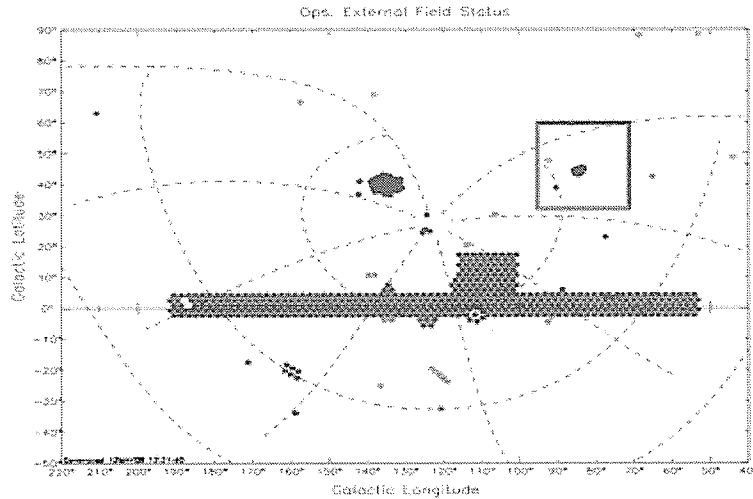


Figure 1.1: ELAIS-N1 - Field location upper right in relation to the Canadian Galactic Plane Survey and the Planck Deep Field (upper left). (7)

Its low level diffuse foreground makes it ideal for observing the extragalactic Universe. For this reason, this region will be analyzed for cosmological purposes, including the most accurate measurement of the Cosmic Background Radiation Field which is to be carried out by the Planck project. Although this field is considered to be relatively empty, there does exist some low level diffuse emission in the field. Planck, which intends to look through this window to map the CMB, must have knowledge of the location and intensity of this diffuse emission in order to accurately measure CMB anisotropies.

1.4 Polarization

Radio emission is measured by a telescope as an electric field \vec{E} . This electric field can be observed using Stokes parameters in different polarization and intensities. The Stokes parameters are given as follows (8):

$$I = E_1^2 + E_2^2 \quad (1.1)$$

$$Q = E_1^2 - E_2^2 \quad (1.2)$$

$$U = 2E_1E_2\cos\theta \quad (1.3)$$

$$V = 2E_1E_2\sin\theta \quad (1.4)$$

Restrictions in bandwidth mean we are not necessarily measuring radiation that is 100% polarized. This is because Stokes parameters are defined in terms of mean quantities, therefore,

$$I^2 \geq Q^2 + U^2 + V^2 \quad (1.5)$$

These equations describe monochromatic radiation where E_1 and E_2 are the amplitudes of field components E_x and E_y and $\theta = \theta_x - \theta_y$ is the phase offset between E_x and E_y . These vectors can describe both circular and linear polarization. Circular polarization occurs when $E_1 = E_2$, $\theta = \frac{\pi}{2}$ and $U = Q = 0$. Linear polarization occurs when $V = 0$ and $E_1 \neq E_2$, which shows that \vec{E} is oscillating with time. As it does so it traces out an ellipse on the xy-plane. This is elliptical polarization. Linear polarized intensity is described by,

$$PI = \sqrt{Q^2 + U^2} \quad (1.6)$$

with fraction of polarization given by,

$$m = \frac{\sqrt{Q^2 + U^2}}{I} \quad (1.7)$$

Angle of polarization is measured from North towards East on the sky and is given by,

$$\Phi = \frac{1}{2}\tan^{-1}\frac{Q}{U} \quad (1.8)$$

Synthesis telescope antennas cannot directly detect Stokes parameters. Instead the synthesis telescope receives both hands, R and L, of circular polarization. Stokes parameters in terms of these quantities are

$$I = \frac{RR + LL}{2} \quad (1.9)$$

1. INTRODUCTION

$$Q = \frac{RL + LR}{2} \quad (1.10)$$

$$U = \frac{i(LR - RL)}{2} \quad (1.11)$$

$$V = \frac{RR - LL}{2} \quad (1.12)$$

More detailed information can be found in Rohlfs and Wilson, Tools of Radio Astronomy, Chapter 3.

1.5 The DRAO Synthesis Telescope

The DRAO synthesis telescope is a seven element antenna array. The parabolic reflector antennas make up an east-west interferometer with a maximum baseline of 617.18m and a minimum baseline of 12.86m. A synthesis telescope with only seven elements cannot take a complete sample of the uv-plane in one synthesis, and therefore, in order to maximize the telescopes sampling, the array consists of four stationary antennas (1,5,6,7) and three antennas (2, 3, 4) which move along a rail track. Two of the antennas (1,7) have a diameter of 9.14m while the remaining 5 (2, 3, 4, 5, 6) have a diameter of 8.53m (9).

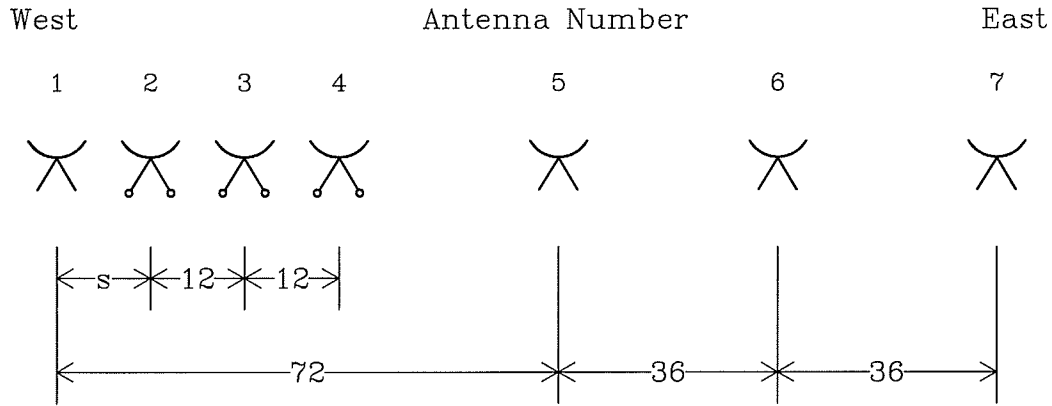


Figure 1.2: The DRAO synthesis array - The figure shows the seven element interferometer configuration displayed on the lower axis with baselines in units of $L=4.286\text{m}$. Displayed on the upper axis, s , is the spacing number for a particular antenna pair. (9)

The telescope observes atomic hydrogen emission using the 21-cm HI spectral line and continuum with two bands centred at 408MHz and 1420MHz in four sub-bands as shown in

1.5 The DRAO Synthesis Telescope

figure 1.3. The 1420MHz band, which observes in Stokes I, Q and U is the one being considered for this project. The total field of view of this band is 2.65 degrees.

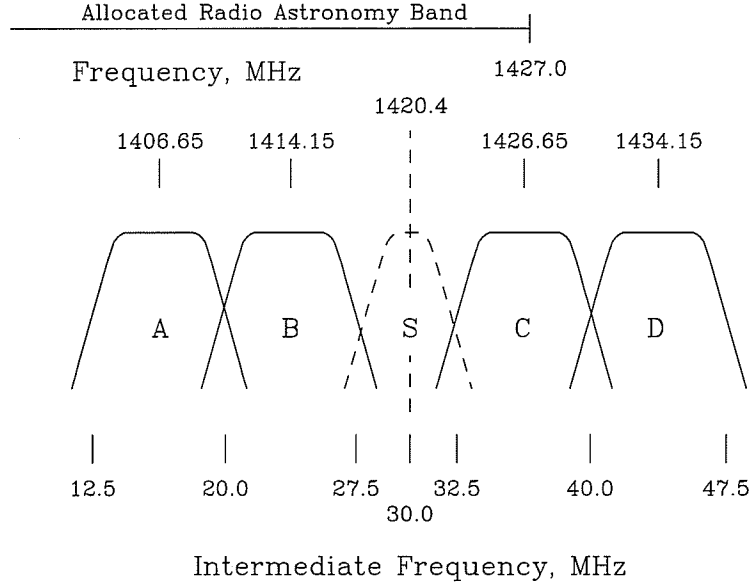


Figure 1.3: Frequency bands - Frequency sub-bands of the DRAO synthesis array. (9)

In order to complete a full observation, a complete synthesis consists of twelve 12-hour observations for each baseline configuration of the telescope. As in Figure 1.2, the movable dishes are moved in increments of $L=4.29\text{m}$. Each synthesis maps out the uv-plane. This plane can be Fourier transformed to obtain the spacial distribution of emission on the sky.

1. INTRODUCTION

1.5.1 Noise Properties of an Interferometer

As a telescope detects astronomical signal, it also picks up a certain amount of noise from thermal origins and from electronic processes with spectra similar to thermal spectra. This is a common form of additive noise that manifests itself as the system temperature of a radio telescope. The contributions to system temperature are:

- **Receiver noise-** The 1420MHz receiver under consideration has a sensitivity which is primarily determined by a low-noise amplifier, having a noise temperature of $T_R \approx 35\text{K}$, or $18\text{K} < T_R < 38\text{K}$ and $\langle T_R \rangle = 33.4\text{K}$ for 16 amplifiers built.
- **Ground noise-** Antenna sidelobes detect spillover and scattering from ground. For the DRAO synthesis telescope this occurs at 3K-8K depending on the antenna being considered.
- **Atmospheric emission-** Radio spectrum contribution from the atmosphere. At 1420MHz this contributes 2K at the zenith and 3K at a zenith angle of 45 degrees.
- **Cosmic Microwave Background-** Low level background contributor to noise which contributes 2.7K.
- **Galactic emission-** Additional background noise contribution from our own Galaxy which typically contributes 0.5K-1.5K to the overall system temperature.

All of these contributors present themselves in the images we observe as the r.m.s. noise:

$$\Delta S = \frac{W\sqrt{2kT_s}}{\eta_c\eta_A A\sqrt{N_b N_{IF}}\Delta f\tau} \quad (1.13)$$

Where W is a weighting factor applied during imaging, k is the Boltzmann constant, η_c is the correlator efficiency, η_A is the aperture efficiency of the array, which when multiplied by the collecting area A which gives the effective area A_e , N_b is the number of baselines, N_{IF} is the number of IF channels with bandwidth Δf (Hz), τ is the integration time and T_s is the system temperature (K). This temperature is characterized for the DRAO synthesis telescope by the technique described in the next chapter.

The goal of this work is to determine if we are able to reliably detect diffuse Galactic emission in the foreground of the ELAIS-N1 field. This emission is of such low intensity that it can be difficult to distinguish from the system temperature noise of the DRAO synthesis telescope, making it necessary to characterize the system temperature, a secondary goal of this project. The following chapters describe:

1.5 The DRAO Synthesis Telescope

- How genetic algorithms are used to derive the system temperatures of the 7 antennas of the DRAO interferometer (Chapter 2).
- Error analysis of synthesis telescope observations of the ELAIS-N1 field (Chapter 2).
- How synthetic images are made from derived system temperatures (Chapter 2).
- Temperature results for 30 ELAIS-N1 fields in Stokes Q and U (Chapter 3).
- Power spectra of Mosaics of ELAIS-N1 data vs. synthetic data in Stokes Q and U (Chapter 3).
- Other applications of the software used and how it is relevant to industry and other branches of astronomy (Chapter 4)

1. INTRODUCTION

2

Techniques

The ELAIS-N1 field is an ideal region through which to view the universe beyond our Galaxy. However, despite its low column density, there still exists some low level emission in the field. This signal is of such a low intensity that it is difficult to distinguish from the system noise of the synthesis telescope. If the signal were of higher intensity, we could simply apply conventional imaging techniques to analyze the field, however, the signal is so weak that new methods must be used to determine what the noise looks like. To separate this weak signal most effectively from the noise, a new technique has been developed to characterize the noise of an interferometer. Once this noise is characterized, it will be possible to differentiate real astronomical signal from what is created by the telescope.

This chapter describes the analytic technique that was developed to complete this task, a genetic algorithm based model interferometer. Also described are the error analysis techniques as well as details of the data used in this analysis.

2.1 Aperture Synthesis

In radio astronomy, resolution is limited by the extent of a telescope. The larger the physical size, the higher the angular resolution of the image. This means that we are limited by our inability to create larger telescopes. The solution to this problem is the technique of aperture synthesis.

In aperture synthesis, several telescopes are used to simulate a large collecting area. This array of telescopes measures the spatial coherence function (8):

$$V(\mathbf{r}_1, \mathbf{r}_2) = \int I e^{\frac{-2i\pi v \mathbf{S}(\mathbf{r}_1 - \mathbf{r}_2)}{c}} d\Omega \quad (2.1)$$

2. TECHNIQUES

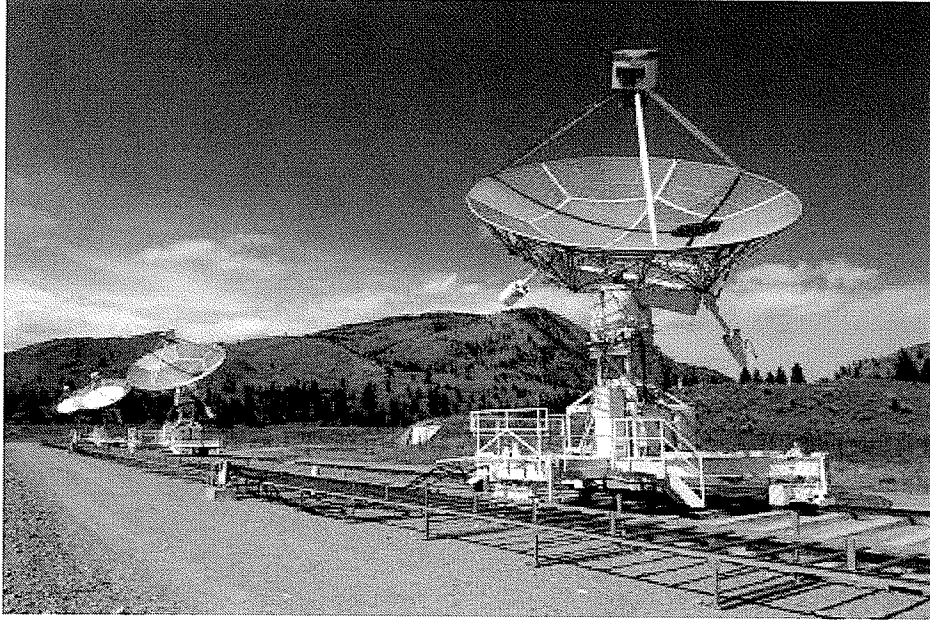


Figure 2.1: The DRAO synthesis telescope - The DRAO telescope which uses aperture synthesis to simulate a large effective area. (7)

where I is the specific intensity and $\mathbf{r}_1 - \mathbf{r}_2$ is the spherical separation vector. This separation vector, known as a baseline, represents the separation of two antennas in the array. The function, $V(\mathbf{r}_1, \mathbf{r}_2)$, known as the visibility, is measured by correlator output of individual interferometers (pairs of antennas). The visibilities are written on to the uv-plane where u and v are rectangular coordinates that project in a plane. Dominance of data in short spacing suggest broad structure, while higher data levels in long spacing suggest fine detail.

As the Earth rotates beneath a synthesis telescope, the antennas map out the uv-plane, a Fourier space which can be transformed to create the image of a field. The number of data points collected by the array during an observation determines the completeness of an image. This effect is shown in figure 2.2, which compares the uv-plane and image plane for an observation of a supernova remnant.

Similar to the way signal is distributed across a baseline, the system temperature noise is as well. Each antenna is equipped with two receivers, one for each hand of circular polarization. These receivers are not identical, so each contributes a different noise level to the visibility data. A consequence of this is that the noise is not distributed uniformly throughout the uv-plane, making the noise from each antenna difficult to disentangle. This is evident in the visibility plane images that will be shown in sections 3.8 and 3.9. Each plateau represents the temperature of a particular pair and it is clear from the figures that they are not equal. There is no analytical

way to derive the system temperature noise of each of the DRAO antennas, therefore, a model must be created which can characterize the noise generated by an interferometer. To arrive at a set of system temperatures, we can compare the noise generated by a model, to the measured noise which occurs from the antenna pairs.

2.2 Genetic Algorithms

In this project a genetic algorithm is used to derive system temperatures for the synthesis telescope. Genetic algorithms are a form of evolutionary computing inspired by biological paradigms such as natural selection and genetic variation. These methods are used to evolve a population of solutions and optimize a large number of parameters. These types of algorithms are ideal for searching through computational problems with a large number of possible solutions, which are typically found in science and engineering (10).

Genetic algorithms rely on three types of operators :

- Selection - gives preference to individuals with good fitness. Fitter individuals are more likely to be selected to reproduce.
- Crossover - chooses two individuals which are exchanged. This offspring is then introduced into the population. Crossover can take two good individuals and create a better individual.
- Mutation - In most GA's this is done by randomly flipping some of the bits of an individual. In Ferret, discussed in the next section, this is done with real number representations. This occurs with a very low probability but ensures diversity in the population. Mutation promotes random searches throughout the parameter space preventing premature convergence.

These operators are common in most genetic algorithms, however, basic to a genetic algorithm is an operator that combines solutions, taking two parents solutions and creating children with similar properties, and a mutation operator which introduces a random kick to the system. A common application of genetic algorithms, and the one applied in this case, is optimization. In the case of this problem the objective is to obtain the most favorable set of solutions by finding the global minimum of some fitness value.

2. TECHNIQUES

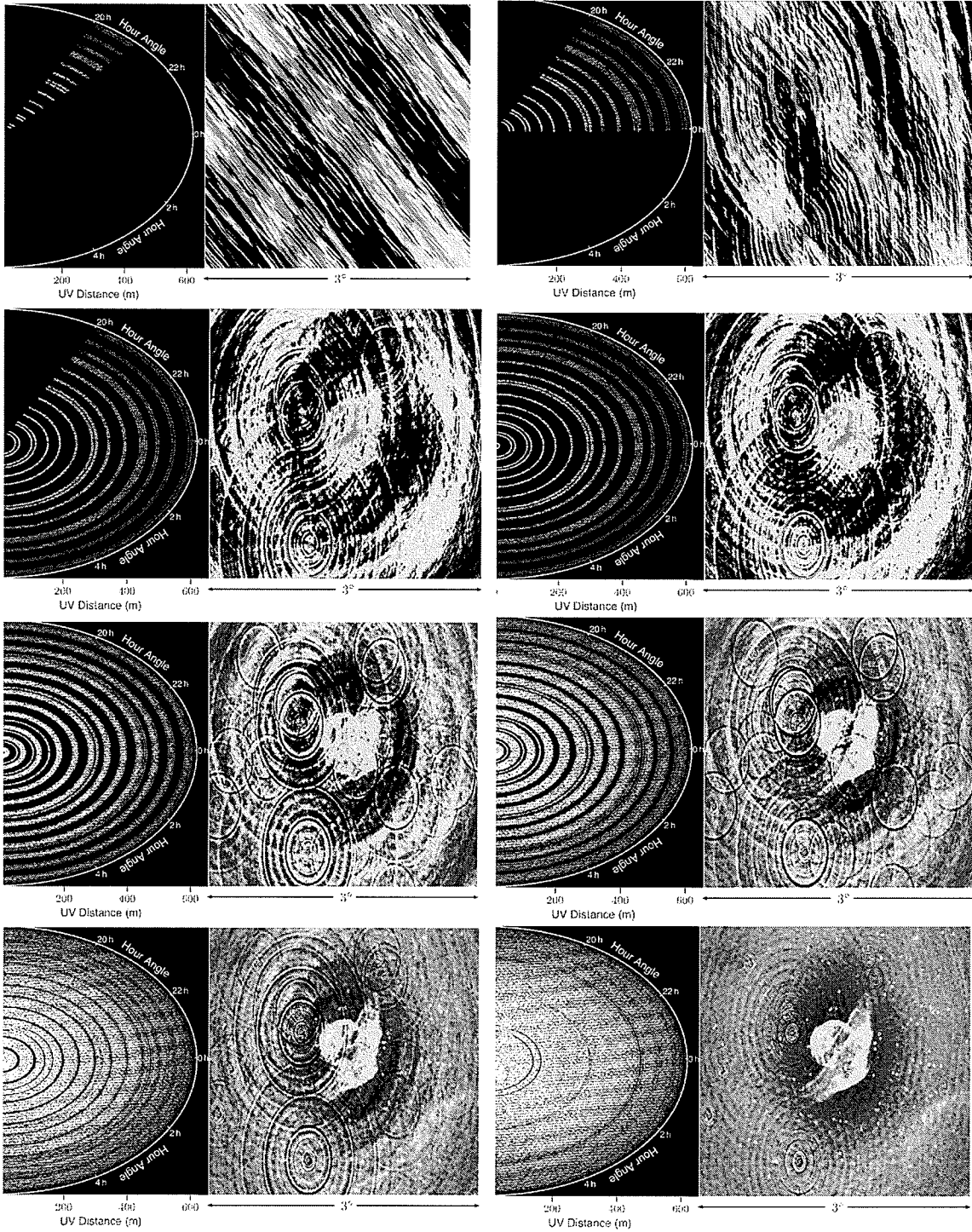


Figure 2.2: This image shows the uv-plane and image plane for various stages of synthesis. From the top going right, these represent images after 1 hour, 4 hours, 10 hours, 12 hours, 4 days, 8 days, 10 days and 12 days. These images are of a super nova remnant and were created by Roland Kothes, DRAO.

2.3 Ferret

Ferret, an advanced genetic algorithm, written by Dr. Jason Fiege, can efficiently solve difficult optimization problems with many parameters. Ferret extends the basic genetic algorithm by identifying non-linearities in the search space and using this information to divide large problems into several small ones that can be solved more easily(3).

Ferret has the ability to stretch beyond the capability of most traditional genetic algorithms because of improvements built into the code. These include but are not limited to •Multi-objective search and parameter space mapping •Simple handling of discrete and cyclic parameters •Automatic zooming •Critical Parameter Detection •Linkage-Learning •Advanced Lethal Suppression •Strategy Auto-Adaptation •Pausing, stopping, and resuming runs •Analysis and integration of polishers and •Integrated visualization (3). The Ferret environment is shown in Figure 2.3.

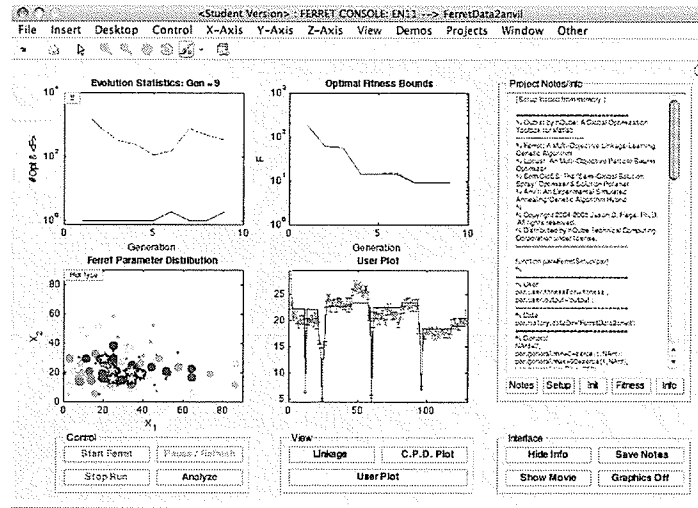


Figure 2.3: Ferret environment - The figure shows the Ferret window during a run. **Top left** : Evaluation statistics: Number of individuals and average fitness value is shown for each generation. **Top right** : Optimal fitness bounds, maximum and minimum, throughout the run. **Bottom left** : Distribution of parameters, in this case T_1 and T_2 , in 2-D. **Bottom Right** :User plot showing the fit between DRAO visibility data and modeled visibility data.

Ferret is able to return a family of solutions within σ of the minimum. In this case σ refers to a tolerance set by the user for a particular problem. For this model, Ferret returns solutions within one of the minimum. These solutions map out a surface in the parameter space that displays the confidence of our minimized parameters (3). Figure 2.4 shows an ellipse-like surface representing the possible solutions while optimizing antenna temperature for ELAIS-N1-7 in

2. TECHNIQUES

Stokes Q.

2.4 Data

The DRAO synthesis telescope, shown in figure 2.1, observes in ninety second intervals over twelve hours for each of its configurations. Each field is observed for 12 hours in each of 12 telescope configurations for a total observing time of 144 hours. The deep field data used for this project includes 30 deep fields which are located near $\alpha=16^{\text{h}} 11^{\text{m}}$, $\delta=55^{\text{d}}$.

The data used for the model is polarization data in the visibility plane. In order to prepare the data for the fitting process, the visibility data for a complete field is sorted by baseline and averaged over the 12 hour observing time. This process is done by the program *srtavg* written by Andrew Gray, DRAO (11). Data sorted in this way can be fit to equation 2.2. It is an ordered representation of quantities read directly from an antenna.

2.5 Detecting Foregrounds

In order to determine whether a significant signal is detected, it will need to be compared to the signal of the system noise. The most effective way of doing this is by analyzing the power spectrum of both of these quantities. A power spectrum is a measure of power against spectral frequency. Power spectra will be created for each of the individual fields as well as the lower noise central region of the complete image mosaic.

In order to create a power spectrum, an image must first be transformed back into the uv-plane. This will revert the image to an ellipse representing the plane of the telescope at the declination of the field being considered. The pixel values along each track of the ellipse are averaged for a complete synthesis, and sorted in order of spacing. The power spectra of data vs. noise will show us where the real signal in the field lies.

2.5.1 Deriving System Temperature

Pure noise from the synthesis telescope is approximated by subtracting bands A and B of the DRAO interferometer, which have frequency 1406.65 MHz and 1414.15 MHz. These adjacent bands are close enough in frequency that subtracting them removes practically all astronomical signal, leaving only signal produced by the system temperature of the telescope. The variance, σ^2 of a particular baseline i, j can be described by:

$$\sigma^2 = \frac{\sum_{i \neq j} g_{ij} T_i T_j}{\sum_{i=j} g_{ij}} \quad (2.2)$$

where T_i is the system temperature of the i^{th} antenna, T_j is the system temperature of the j^{th} antenna, and $g_{i,j}$ is the redundancy (how many times a spacing is measured in a complete observation) of the antenna pair i, j . It is this equation that is used in our code to derive antenna temperature. The basis of the code is fitting the equation to pure noise visibility data using Ferret in order to derive the seven temperature parameters. After completing the number of generations specified by the output file (for the case of this project 200, or typically 150 past convergence), Ferret returns a seven parameter solution which is equivalent to the system temperatures of the seven antennas.

The software for this project is written in Matlab. A detailed description of the code can be found in the last section of this chapter and the software can be found in its entirety in the appendix.

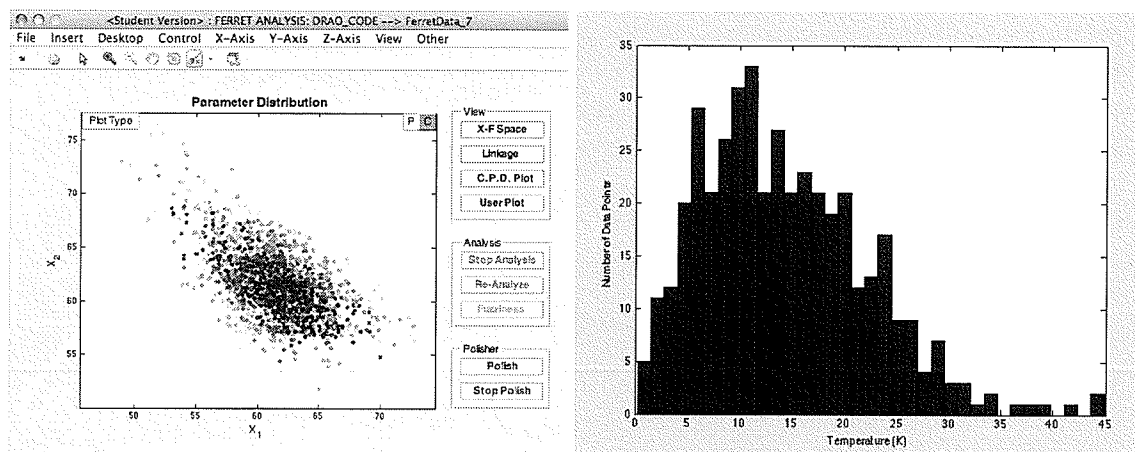


Figure 2.4: Left: Analysis window of solution surface returned by Ferret. This surface is produced after 100 generations. Right: Histogram of the 480 band A minus band B data points that are averaged into one baseline. The distribution suggests standard gaussian error analysis cannot be applied. The temperature values differ from the final results by an arbitrary factor of approximately 2.

2.5.2 Bootstrap Monte Carlo Method

As is shown in figure 2.4, the data that are averaged to one visibility data point are not visually gaussian. This distribution is common to all data sets which make up the visibility plot being considered as the fit for our model. This means that in order to properly analyze the errors in our data and results, a method independent of distribution must be used.

2. TECHNIQUES

For unknown distributions, the bootstrap method is a good estimator of errors. This method uses the data set being considered to generate a new, synthetic data set with any number of points. That is, considering some data set, D_i which contains N data points, we can obtain any number n data sets $D_1, D_2 \dots D_n$ from the original set. This is possible because replacement is allowed, therefore returning a resampling of the original data set with a random fraction of data points, on which we can carry out commonly known error analysis techniques and statistics (12).

2.5.3 Noise Characterization in Short Spacings

It is common for interferometric data to be unusable at short spacings. These spacings contain large amounts of noise because of the proximity of the telescopes that make up these baselines. Though it is not really known, it is suspected that these antennas “talk” to each other and create greater noise because they detect spillover from each others sidelobes and share common ground noise. This effect is shown in figure 2.5.

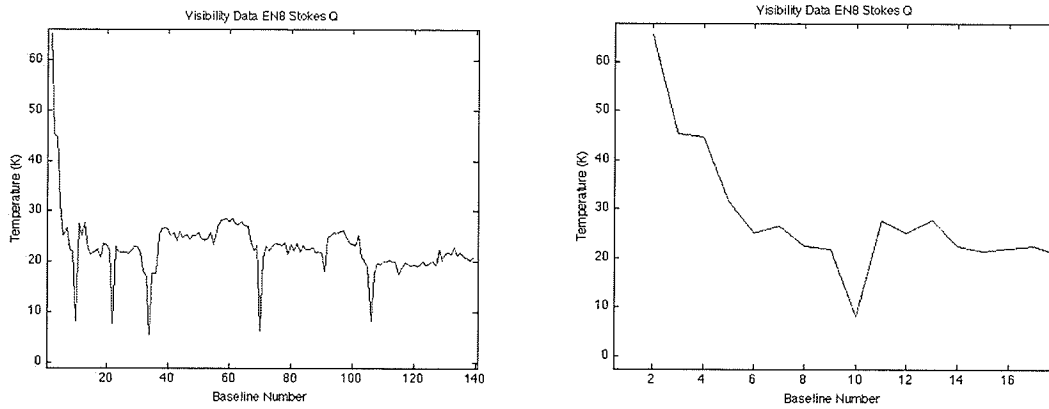


Figure 2.5: Noise at Short Spacings - Visibility data for EN08 Stokes Q, in which we can see a large spike in the signal at short spacings.

The figure shows a large spike at short spacings which contain information about the broad structure in the sky. Often, in order to compensate for this unusable data, single dish observations are used to supplement the synthesis telescope data because of their ability to resolve broad structure.

For the purposes of this experiment, these short spacings have been removed. Because of the robust genetic algorithm technique being used, very little information is lost due to this

removal, when deriving system temperature.

2.5.4 Mosaics

In order to achieve a high sensitivity level, the 30 fields of the ELAIS-N1 deep field are observed close together. A technique designed to increase sensitivity is producing a tiled image of the total field called a Mosaic. This mosaic is created by averaging data from each field and weighting that value by a value that is determined by distance from the field centre. The weighting factor is given as (13):

$$w_m = \left(\frac{A(\rho_m)}{\sigma_m} \right)^2 \quad (2.3)$$

Where A is the primary beam attenuation, ρ_m is the offset of the pixel in field m , and σ_m is the rms noise level at the centre of the field. The rms noise in the final mosaic is (13):

$$\sigma = \left(\sum_{m=1}^N w_m \right)^{-\frac{1}{2}} \quad (2.4)$$

The centre of the mosaic is close to the centre of several fields, meaning that this area of the mosaic has the least noise.

Note: Polarization images and data mosaics of the ELAIS-N1 field were processed by Julie Grant, University of Calgary.

2.5.5 Creating Images

When an image plane is created by Fourier transforming the simulated visibility data, it needs to be output into a readable format in order for a mosaic to be created. The MATLAB package *mfitsio* (14), which contains a fits writing package, is used to create fits files of each of the individual fields. These fits files, are then converted into *madr* format so that a mosaic can be made using the DRAO *supertile* routine. The output of *supertile* is a 1024x1024 Mosaic image. This process is done on the synthetic system temperature data. The mosaics of the entire 30 ELAIS-N1 fields which are used for comparison were created by Julie Grant, University of Calgary. For more information see “Compact Polarized Radio Sources in the ELAIS-N1 Field”

2.5.6 Mosaic Analysis

In order to get an idea of what type of noise is present in a large portion of the sky, the mosaic of both the synthetic system temperature field and the ELAIS-N1 field are compared in both Stokes Q and U. For this purpose, point sources are removed from the real data mosaics so that

2. TECHNIQUES

the signal we are left with is mainly diffuse structure. This can only be done for either positive or negative point sources at a time, so, four different mosaics have been considered for this project.

During the mosaicing process, images are tiled in order to reduce the noise level in the field centre. The best data from which to take a power spectrum would be near the image centre and not the sides of the mosaic (which are much noisier than the centre.) Therefore, a section of the image centre is transformed into the uv-plane, and a power spectrum is taken along this plane. This allows us to determine if there is any detectable diffuse emission in the centre of the field. The results of these processes are shown in the following section.

2.6 Creating and Analyzing Images

In this section, the software which was developed throughout the course of this project is described in detail. The previous sections of this chapter are intended to provide information which makes the scientific processes in the code understandable. This section is supplemented by the Appendix which contains a printed version of code with comments.

2.7 Software Outline

The following description of the software written for this project follows the actual code shown in the Appendix. This description will explain initial setup files, the fitting process, and any post processing done to the results.

2.7.1 Initial Setup: `init_AllFields.m`, `DRAO_Constants.m`, and `CalcVisData.m`

`init_AllFields.m` is an initial program which loads all the data files that are required for calculating visibility data for the model. This program also calls `DRAO_constants.m`, which contains all of the constants relevant to the DRAO synthesis telescope and its observation of the ELAIS-N1 fields considered for this project. Also contained in this file is the information about the redundancies of each baseline, and which antennas make up particular baselines. This information is used to create a synthetic visibility plane and to properly assign a temperature to each pair, so that the individual temperatures can be extracted by the model.

After loading the data and constants, the visibility data must be prepared so it can be fit by the model. This is done in the program `CalcVisData.m` by the following methods. First, visibility data from bands A and B of the synthesis telescope are subtracted and divided by $\sqrt{2}$ to remove all astronomical signal and produce a visibility plane that consists entirely of noise.

$$Response = \frac{BandA - BandB}{\sqrt{2}} \quad (2.5)$$

Flagged data points (bad data) are removed and the visibility plane is converted into units Kelvin. The data must now be sorted into a usable form, so it is placed in baseline order and the standard deviation of the 480 observations that make up a full synthesis is taken. The value at each baseline now represents the variance of that antenna pair. The error in this baseline value is determined by using bootstrap Monte Carlo methods on these 480 observations. This is the type of data that we wish to fit our model to, but the problem at this stage is that we are missing a calibration factor that is characteristic of synthesis telescopes.

This factor arises from the subtleties of the Fourier relationship between the uv-plane and the image plane; More specifically, the fact that no uv-plane is complete unless all baselines are present, which is not true in the case of DRAO because spacings 141, 142 and 143 are not filled in during synthesis. Limitations in image resolution can also allow for gaps or missing pixels in the plane. If a uv-plane is to be represented as a large image, say 1024x1024, this means more zero value pixels than an image of size 256x256. The uv-plane translates to power on the sky, and therefore a uv-plane which contains only noise should have the same value when averaged as the noise of the image it creates. So, when data is taken by the telescope and is in its unprocessed visibility form, the power lost to missing spacings is not accounted for. Because the data being used for the fitting is unprocessed, the missing power factor must be derived by some means before the true system temperature can be determined.

In order to derive this factor, a uv-plane is created from the visibility data. This is done by distributing the data along an ellipse that is geometrically defined by the declination of the field. The data is distributed along one quadrant, simulating an observation, and then that quadrant is placed on all corners of a grid. This forms an image of the uv-plane.

The non-zero tracks on the uv-plane created should have the same standard deviation as a noise image created by subtracting bands A and B in the image plane. Therefore in order to calibrate the visibility data, a noise image is simulated by subtracting the single band image data. The ratio of its standard deviation and the standard deviation of the created uv-plane is the calibration factor.

The visibility data is then multiplied by the calibration factor. The short spacings are removed to eliminate unexplainable noise spikes in the data (see section 2.5.3). The data is now ready to be fit by the model.

2. TECHNIQUES

2.7.2 Fitting Process: ComputePower.m, fitness.m

In the code ComputePower.m, derivation of the antenna temperatures is carried out by allowing the seven temperatures to be free parameters during the fitting process. A visibility plane is modeled by use of the variance equation:

$$Var_{model} = \sqrt{\frac{\sum_{i \neq j} g_{ij} T_i T_j}{\sum_{i=j} g_{ij}}} \quad (2.6)$$

As the temperatures are varied this equation is fit to the data described in the previous section. The model is fit to the data using the Ferret genetic algorithm and reduced in fitness.m using reduced χ^2 equation:

$$\chi^2 = \frac{Var_{model}^2 - Var_{data}^2}{\sigma^2 n_d n_p} \quad (2.7)$$

Where Var_{model} is the variance value evaluated by Ferret, Var_{data} is the variance value of the data, σ is the error in the data, n_d is the number of data points and n_p is the number of parameters. For this problem, Ferret was run for 100 generations for each field in Stokes Q and U polarizations. The outputs are a surface of possible solutions, and a plot of the model to data. These are shown for each field in the results chapter.

2.7.3 Post Processing, makeImage.m

The post processing code takes the seven temperatures which are derived and uses them to make a synthetic noise image. The seven temperatures are converted from Kelvin to mJy and distributed across the uv-plane in quadrants by the same method as in 2.7.1. This uv-plane is sampled in the same way as the DRAO interferometer. That is, each twelve hour observation contains 480 observed data points, meaning each quadrant contains 240 sampled points per baseline. These sampled points are placed on a uv-plane which contains random gaussian noise. The ellipse that is created is then analyzed to show a power spectra of the synthetic temperature data. It is important to note that, as with the DRAO synthesis telescope software, each elliptical baseline is considered to contain the same number of points regardless of the physical length of the track. This presents itself as the slight tapering of the power spectra at higher spacings and can be seen in the figures presented in the next section.

The synthetic power spectrum is compared to one taken from the data. The fast fourier transform of the image of the field is taken, and then a power spectrum is taken of the resulting ellipse. The difference in the two spectra shows where the signal in the field is located relative to the noise.

2.7.3.1 Making Mosaics

A mosaic allows us to reduce the noise in an image, which is why the ultimate goal is to compare the synthetic and real data at that level. In order to create a mosaic of the synthetic data, the uv-plane which is created purely from derived temperatures is fast fourier transformed to create an image that is entirely system temperature noise. These images are made in fits format files that are turned into mosaics using DRAO software. A 256x256 section is selected from both the synthetic and real images, and a power spectrum is taken in the same manner as in makeImage.m. The results are shown in the next chapter.

2.8 Summary

Software, written in Matlab, uses the Ferret genetic algorithm to derive the seven system temperatures of the DRAO antennas. It does so by fitting a model interferometer to visibility data from which all signal has been removed, leaving data which contains only noise. Images are then created from this data and a mosaic is made.

The individual field images are compared by power spectra to the real data. The same is done for a low-noise section of the mosaics, from which either positive or negative point sources have been removed. These power spectra show the level of noise of the synthesis telescope in relation to the real data. From these spectra it can be deduced if there is any detectable diffuse emission in the field.

2. TECHNIQUES

3

Results

There is no analytical way to measure the system temperature of a synthesis telescope because no two antennas can be completely identical. This is especially true of the DRAO interferometer. The results presented in this chapter show the derived system temperatures for the DRAO synthesis telescope for 29 ELAIS-N1 fields in Stokes Q and U polarizations. Also included are the power spectra for each field taken from an image created by the temperature data, and an image of real data. It is from this image we can deduce the foreground contribution in each field. These spectra can be found at the end of the chapter. In addition, the quality of the Ferret results will be demonstrated in this chapter by comparing temperature and χ^2 quantities to those obtained using other optimizers.

For the purpose of this experiment, the visibility data for EN01 was not complete enough to be fit by the software within confidence. Because EN01 lays on the outside of the ELAIS-N1 field, it will not be present in the final power spectrum (which only includes a mosaic of the field centre), and therefore will not impact the final result.

Mosaics of the system temperature noise for Stokes Q and U are presented, as well as a power spectrum of this mosaic vs. the ELAIS-N1 mosaics.

While optimizing system temperature, Ferret outputs an error surface representing all possible solutions within one of the optimal, as well as a user plot which has been specified to show the fit between the model and data. These plots are included at the end of this chapter.

3.1 Ferret System Temperature Results

3. RESULTS

Field Name	Antenna Temperatures (K)	Chi-squared
EN02	76.41, 61.78, 50.91, 52.00, 97.95, 80.11, 57.58	2.98
EN03	73.91, 59.39, 48.20, 49.79, 89.98, 74.08, 55.21	2.51
EN04	56.68, 53.40, 47.02, 49.29, 80.76, 64.97, 45.98	8.54
EN05	64.18, 47.49, 43.33, 44.23, 86.57, 69.25, 49.41	2.69
EN06	67.63, 49.21, 45.62, 45.78, 89.01, 75.78, 51.43	1.90
EN07	65.99, 57.17, 47.24, 47.99, 85.67, 69.40, 48.66	2.40
EN08	76.52, 58.75, 48.66, 50.32, 98.22, 78.75, 57.70	2.59
EN09	64.69, 49.29, 42.28, 46.55, 84.93, 66.18, 48.24	2.11
EN10	62.24, 54.19, 48.42, 51.17, 76.68, 59.94, 44.30	2.30
EN11	67.20, 52.92, 43.05, 43.32, 90.04, 72.99, 51.52	1.83
EN12	65.35, 55.02, 43.83, 43.69, 86.99, 70.43, 49.75	1.34
EN13	61.42, 50.25, 42.89, 45.42, 80.04, 61.73, 44.86	1.89
EN14	54.26, 56.94, 44.39, 45.00, 71.05, 57.08, 41.52	2.27
EN15	56.81, 54.36, 42.41, 42.92, 74.43, 59.93, 43.39	2.33
EN16	78.46, 53.38, 45.09, 44.96, 96.55, 78.13, 59.02	2.38
EN17	65.27, 58.68, 48.87, 50.95, 84.10, 69.60, 50.41	2.09
EN18	62.50, 52.80, 46.81, 47.63, 76.93, 63.50, 45.37	2.46
EN19	58.28, 52.07, 45.05, 48.05, 72.81, 58.51, 43.28	2.80
EN20	59.69, 51.38, 44.59, 45.84, 76.27, 60.35, 45.03	2.42
EN21	59.90, 56.17, 43.01, 43.63, 76.71, 60.91, 44.74	1.58
EN22	62.68, 50.31, 44.91, 45.31, 84.85, 68.45, 47.98	2.07
EN23	60.47, 54.52, 48.29, 49.65, 74.00, 59.10, 44.16,	3.00
EN24	62.46, 53.99, 47.33, 48.32, 78.59, 63.06, 47.66	3.81
EN25	60.09, 52.94, 44.28, 45.92, 79.10, 63.81, 46.45	2.77
EN26	68.35, 50.92, 39.63, 39.79, 88.26, 68.22, 51.34	1.73
EN27	64.64, 49.79, 43.67, 44.86, 84.43, 65.89, 47.82	2.50
EN28	66.47, 50.52, 43.71, 45.13, 85.25, 66.47, 48.55	4.72
EN29	65.57, 58.58, 45.99, 45.69, 83.71, 65.44, 49.24	2.04
EN30	59.04, 69.15, 54.83, 54.89, 77.50, 63.52, 44.42	1.59

Table 3.1: Temperature and fitness values obtained by using the Ferret genetic algorithm, Stokes Q. The temperatures are shown to vary from field to field as the factors which contribute to system temperature are not constant between observations. There are also randomizations present in genetic algorithms that can contribute to small differences between runs.

3.1 Ferret System Temperature Results

Field Name	Antenna Temperatures (K)	Chi-squared
EN02	78.71, 59.11, 49.18, 49.96, 100.00, 83.03, 58.91	2.30
EN03	73.28, 60.08, 49.46, 51.70, 91.86, 72.50, 54.47	2.50
EN04	57.12, 54.72, 47.43, 49.51, 78.60, 63.75, 45.10	9.01
EN05	66.99, 44.56, 42.08, 41.41, 93.85, 73.81, 51.99	2.81
EN06	64.77, 50.66, 47.51, 46.97, 85.16, 74.10, 49.68	2.69
EN07	67.69, 55.96, 46.32, 47.07, 87.66, 71.29, 50.06	2.49
EN08	70.70, 63.99, 52.75, 54.59, 90.00, 72.87, 53.42	2.63
EN09	67.91, 46.47, 40.12, 42.16, 91.47, 69.98, 50.53	1.86
EN10	63.44, 53.03, 46.18, 49.05, 78.75, 63.15, 46.20	2.40
EN11	66.76, 52.48, 42.60, 42.66, 89.99, 73.51, 51.47	1.57
EN12	63.95, 57.55, 45.68, 44.44, 84.28, 68.83, 48.40	2.10
EN13	64.22, 46.34, 40.45, 41.81, 85.88, 67.07, 49.48	1.69
EN14	64.61, 47.34, 41.44, 43.68, 86.06, 68.74, 51.23	5.77
EN15	65.18, 48.41, 37.36, 38.82, 85.83, 67.33, 49.04	1.99
EN16	80.14, 52.89, 44.65, 44.44, 98.49, 79.50, 59.97	2.39
EN17	64.14, 59.17, 49.27, 51.49, 82.89, 68.71, 49.75	2.15
EN18	63.68, 51.55, 45.78, 46.60, 78.59, 65.14, 46.31	2.45
EN19	57.08, 55.06, 46.39, 49.99, 69.71, 57.78, 42.53	3.99
EN20	64.84, 48.89, 41.53, 43.64, 80.32, 65.20, 48.49	2.36
EN21	60.25, 54.61, 43.01, 43.49, 77.12, 61.12, 45.28	1.87
EN22	62.97, 49.42, 43.43, 44.59, 86.36, 69.77, 48.95	1.60
EN23	57.27, 56.74, 50.74, 51.95, 71.39, 56.42, 42.61	2.56
EN24	67.51, 49.63, 42.83, 44.26, 85.11, 70.39, 53.13	3.01
EN25	66.20, 47.53, 40.70, 41.61, 86.32, 70.37, 51.80	3.01
EN26	66.59, 52.13, 41.34, 41.23, 84.21, 67.71, 50.27	2.01
EN27	62.05, 50.43, 44.47, 46.34, 82.24, 64.09, 47.34	2.20
EN28	69.77, 47.50, 41.59, 43.03, 92.01, 70.85, 51.46	3.18
EN29	66.85, 56.80, 44.51, 44.48, 86.70, 67.63, 51.34	2.20
EN30	67.36, 59.48, 48.21, 47.67, 89.88, 72.64, 51.46	1.92

Table 3.2: Temperature and fitness values obtained by using the Ferret genetic algorithm, Stokes U.

3. RESULTS

3.2 Mosaics

Shown in this section are the Mosaics created from images synthesized using the system temperature derived, which are shown in the previous section. A power spectrum of the centre 256x256 pixels is then taken and compared to the same section of the real data mosaic, which was created by Julie Grant. Those power spectra are also presented here.

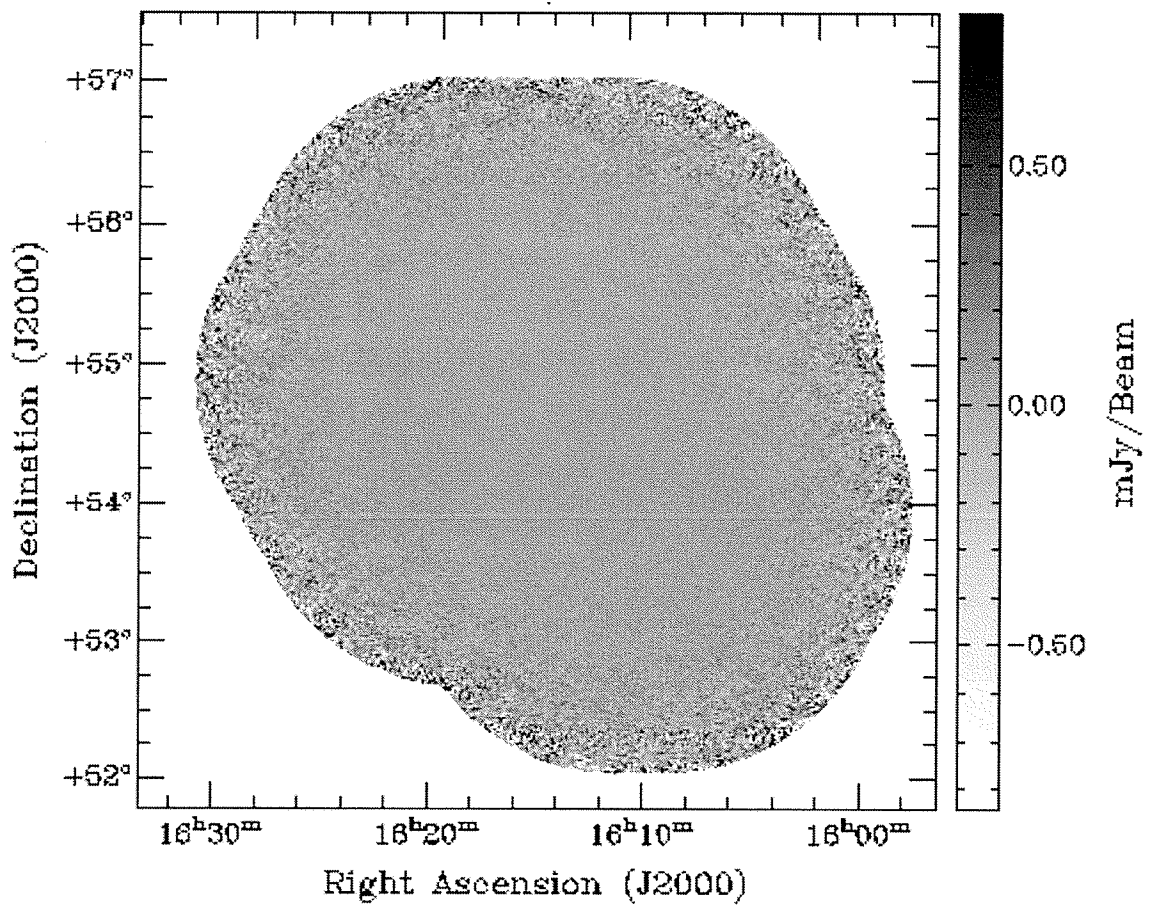


Figure 3.1: Stokes Q synthesized mosaic

3. RESULTS

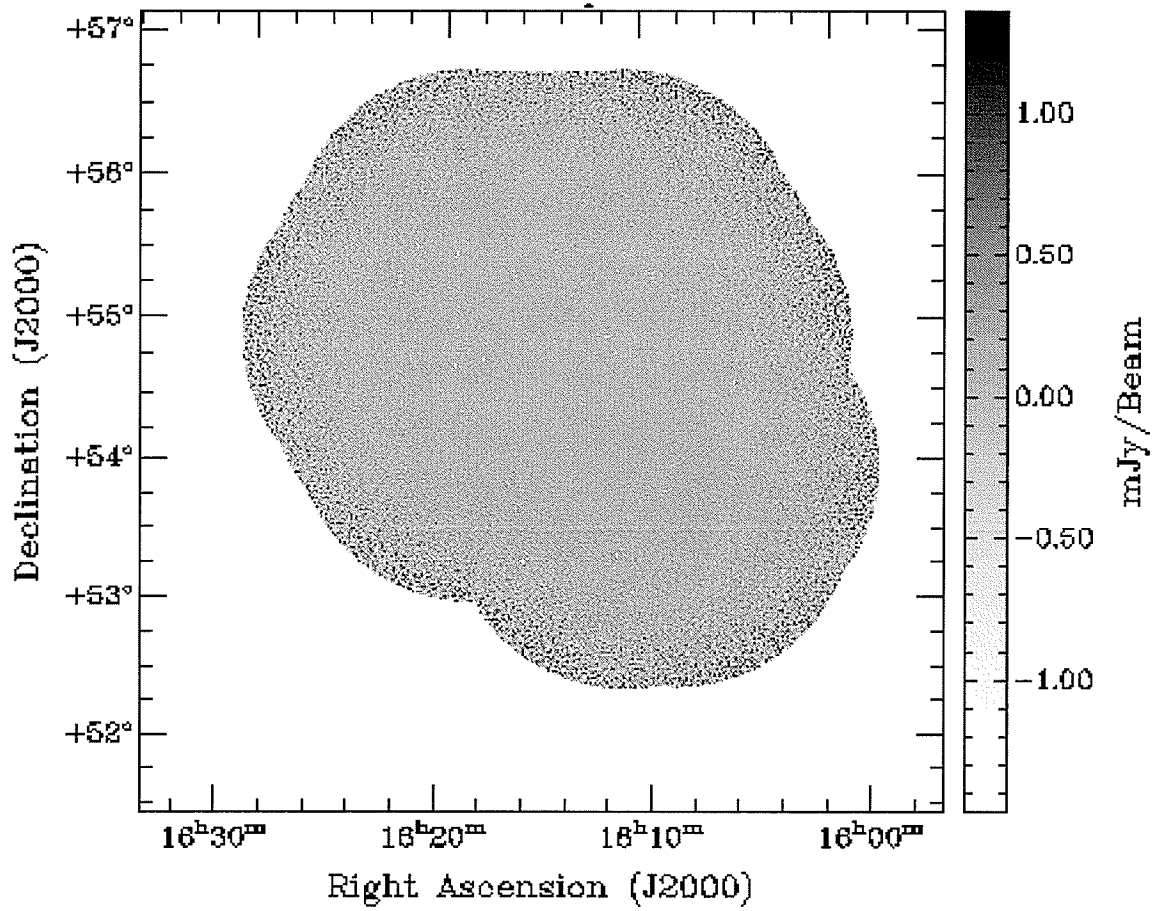


Figure 3.2: 30 Field ELAIS-N1 mosaic in Stokes Q with positive point sources removed. This mosaic was made by Julie Grant, University of Calgary

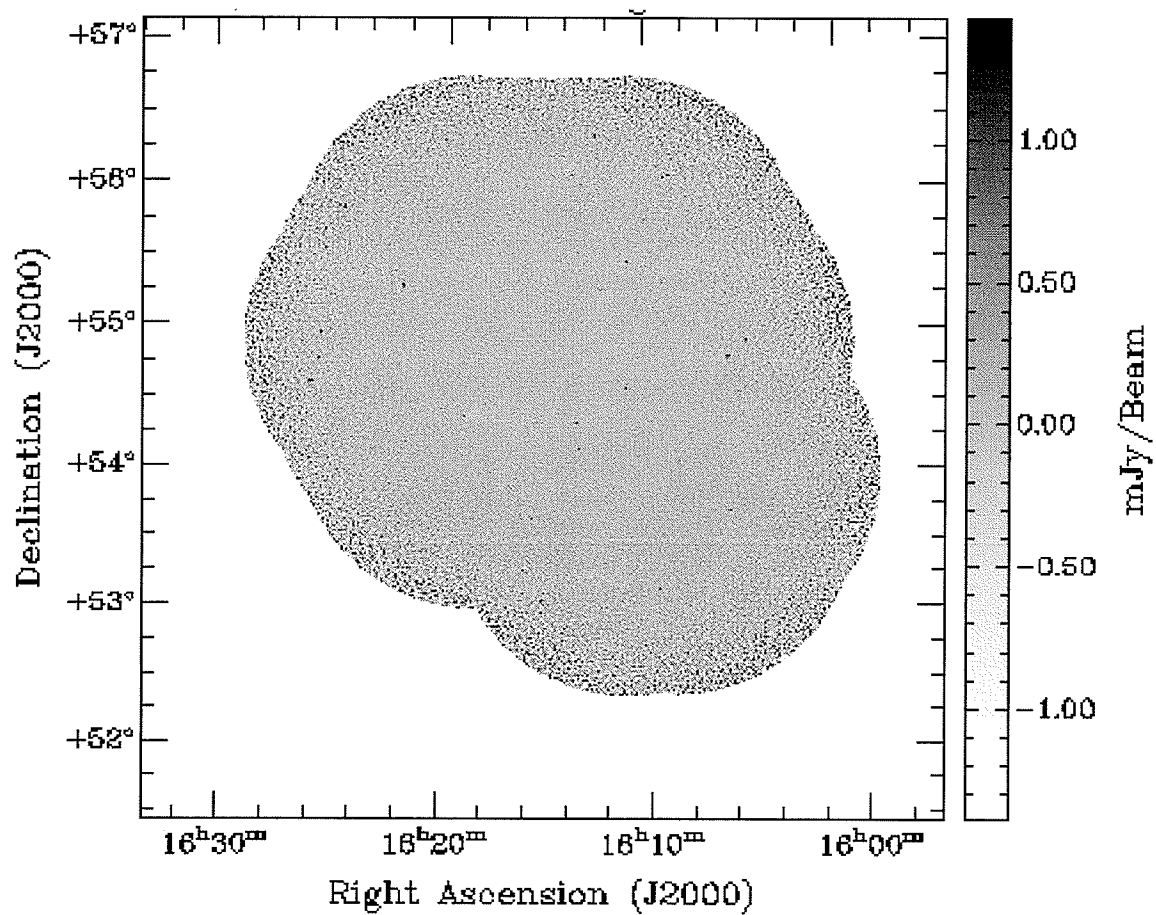


Figure 3.3: 30 Field ELAIS-N1 mosaic in Stokes Q with negative point sources removed. This mosaic was made by Julie Grant, University of Calgary

3. RESULTS

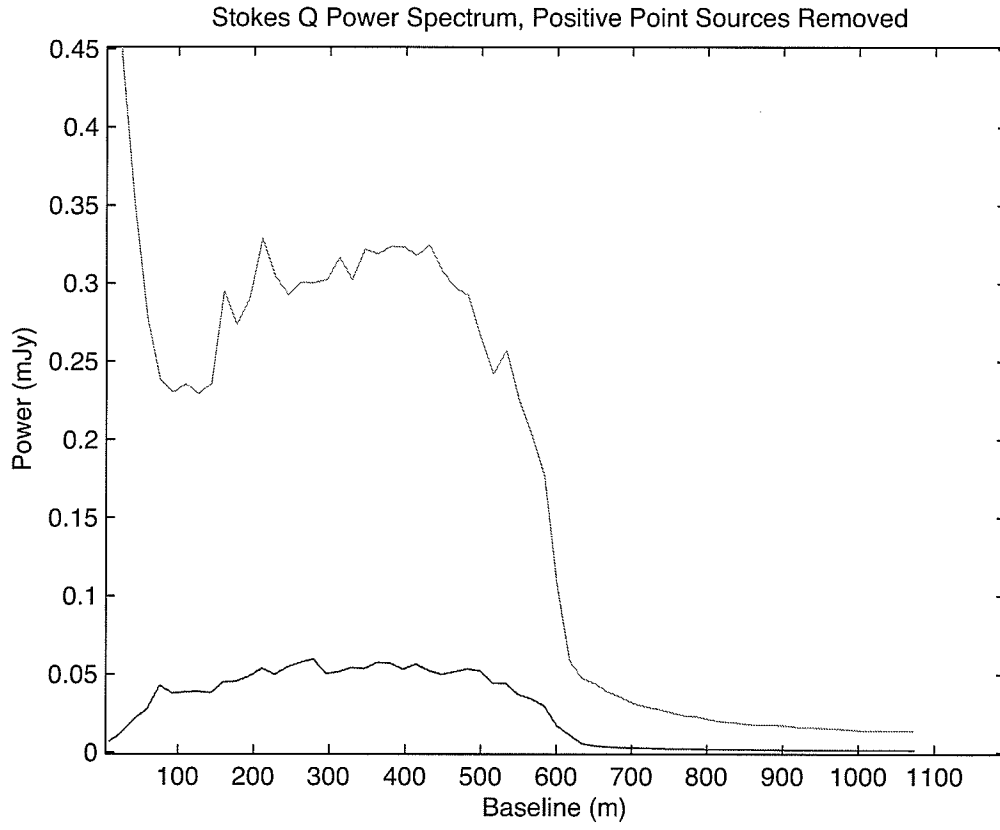


Figure 3.4: Stokes Q power spectra where the spectrum of the real data has positive point sources removed. Note the red line is the data mosaic and the blue line is the synthetic mosaic.

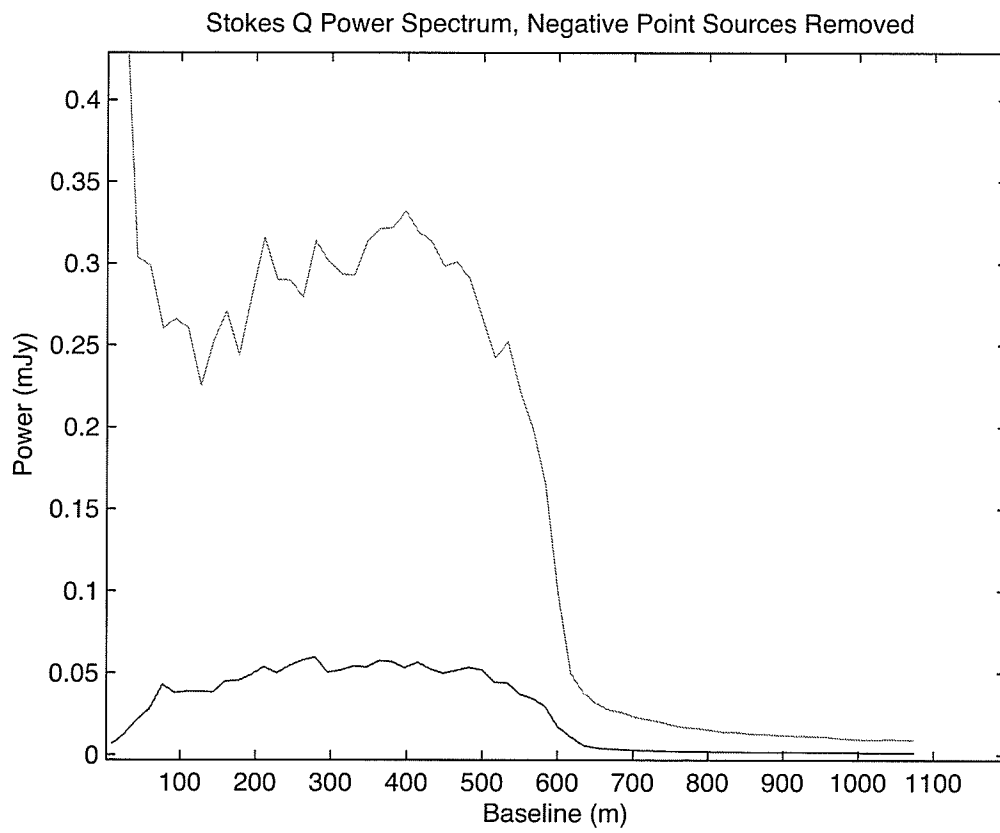


Figure 3.5: Stokes Q power spectra where the spectrum of the real data has negative point sources removed. Note the red line is the data mosaic and the blue line is the synthetic mosaic.

3. RESULTS

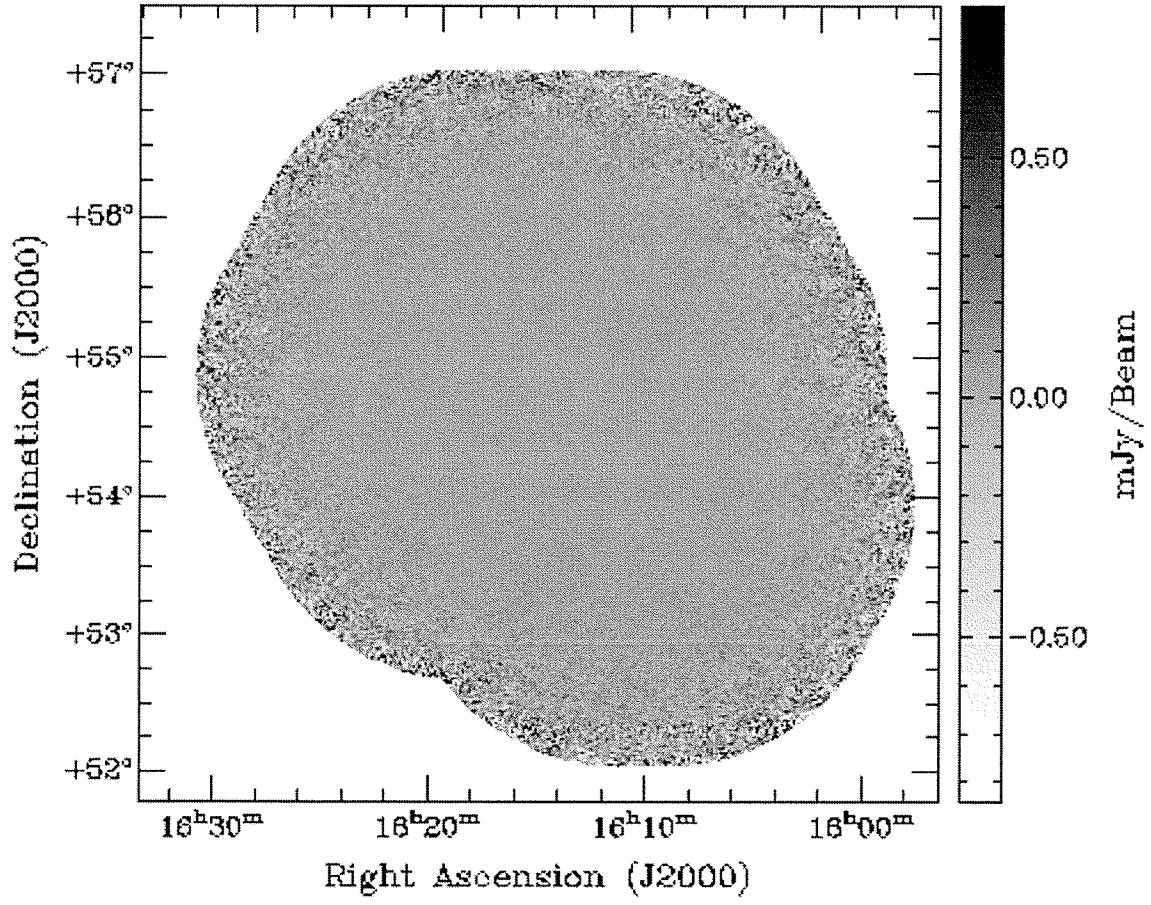


Figure 3.6: Stokes U synthesized mosaic

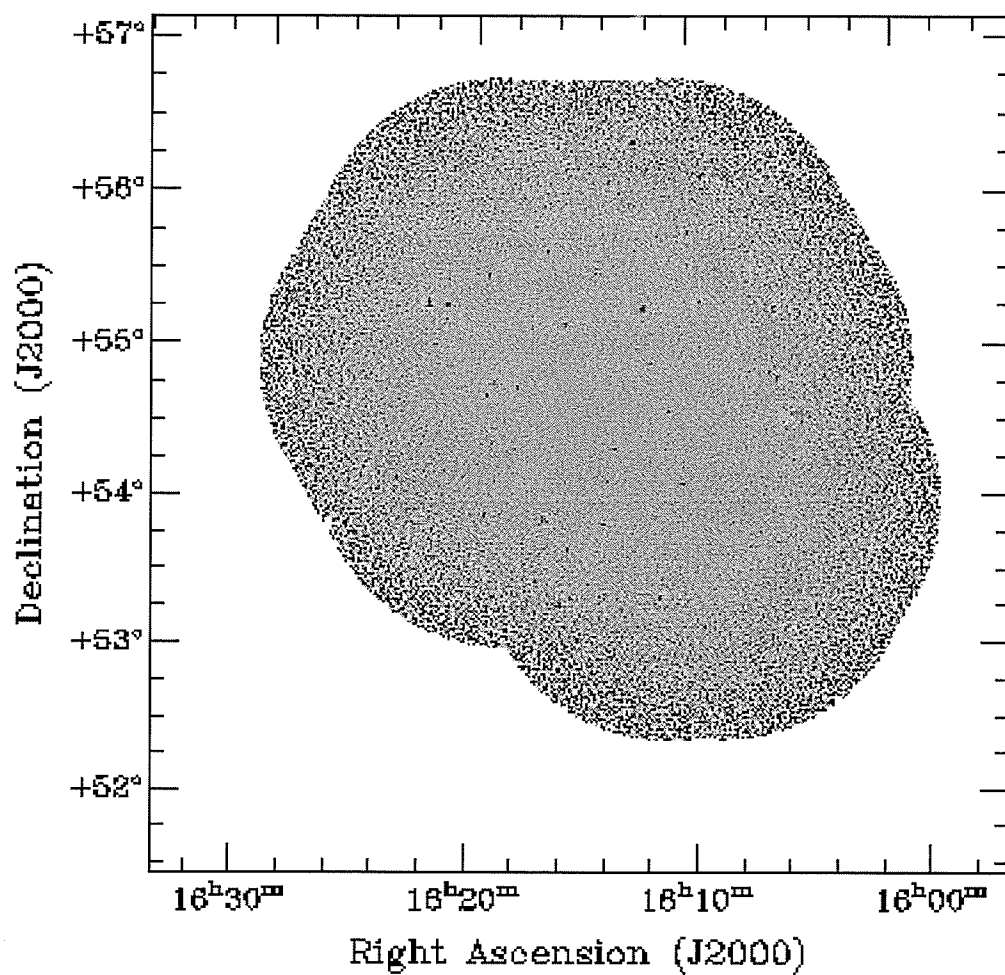


Figure 3.7: 30 Field ELAIS-N1 mosaic in Stokes U with positive point sources removed. This mosaic was made by Julie Grant, University of Calgary

3. RESULTS

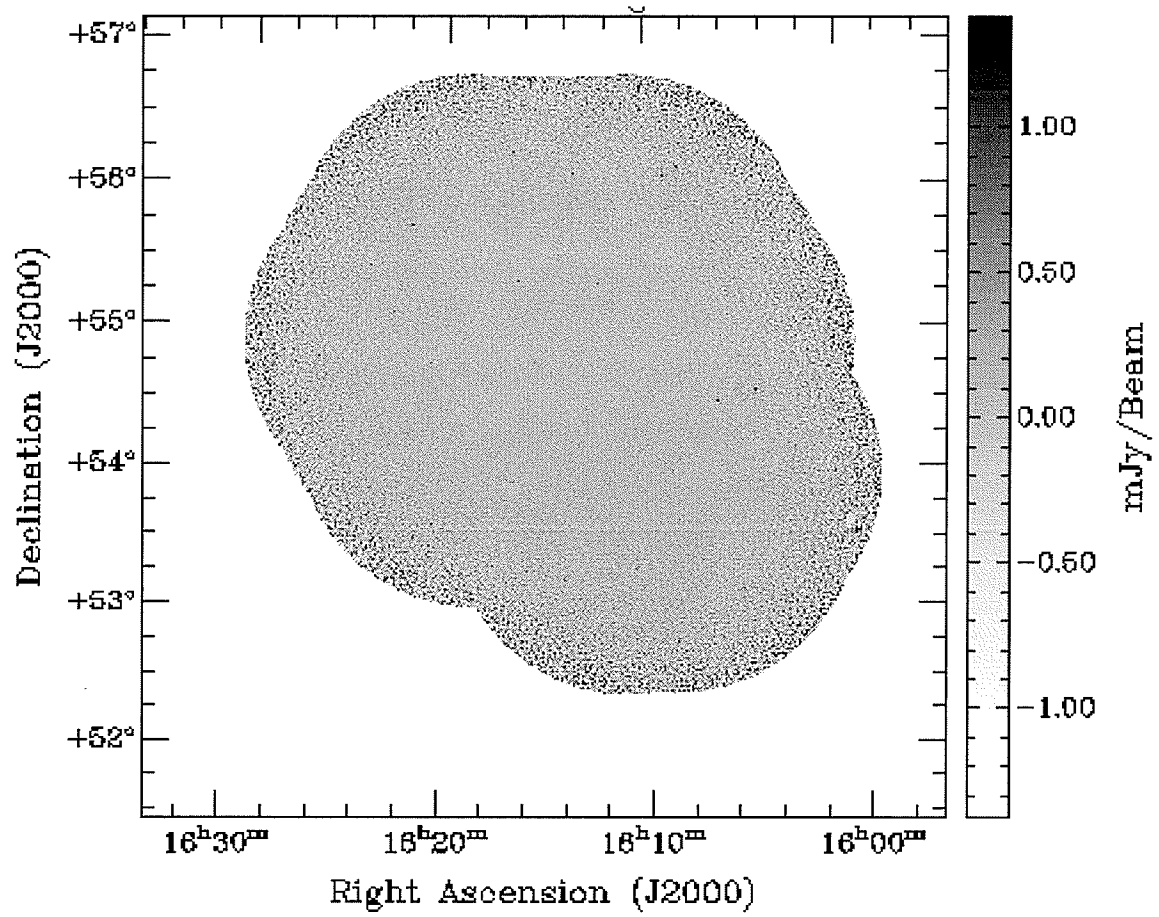


Figure 3.8: 30 Field ELAIS-N1 mosaic in Stokes U with negative point sources removed. This mosaic was made by Julie Grant, University of Calgary

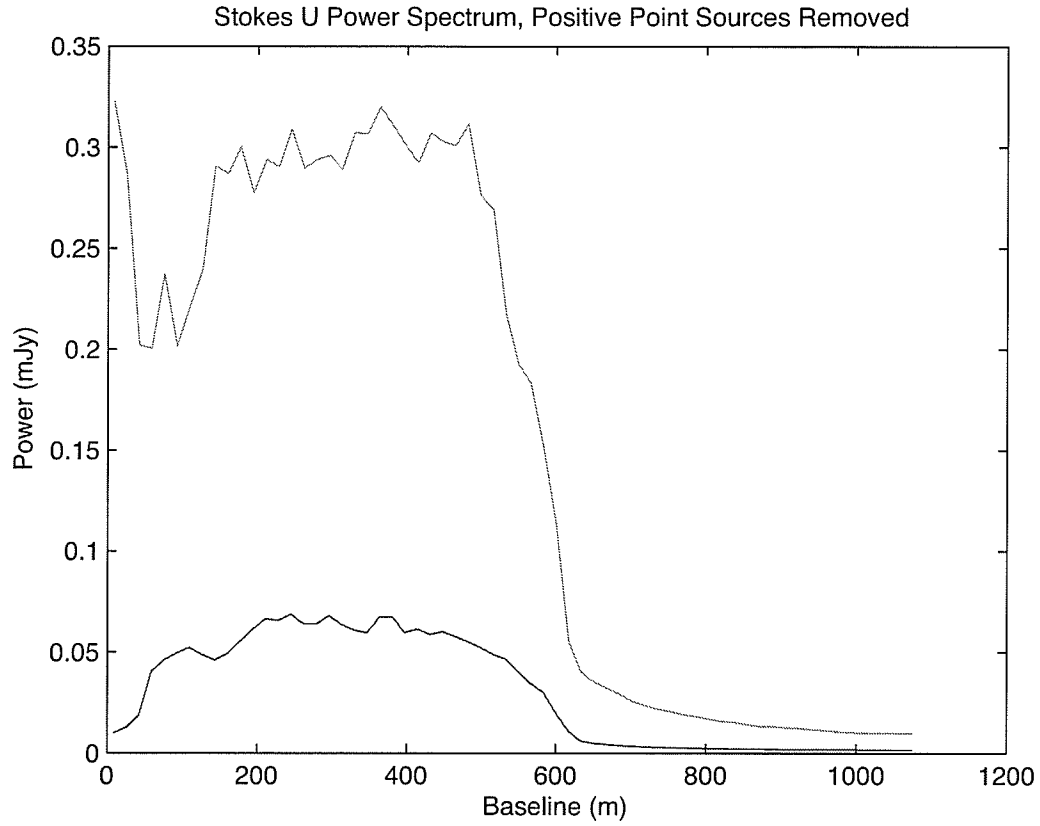


Figure 3.9: Stokes U power spectra where the spectrum of the real data has positive point sources removed. Note the red line is the data mosaic and the blue line is the synthetic mosaic.

3. RESULTS

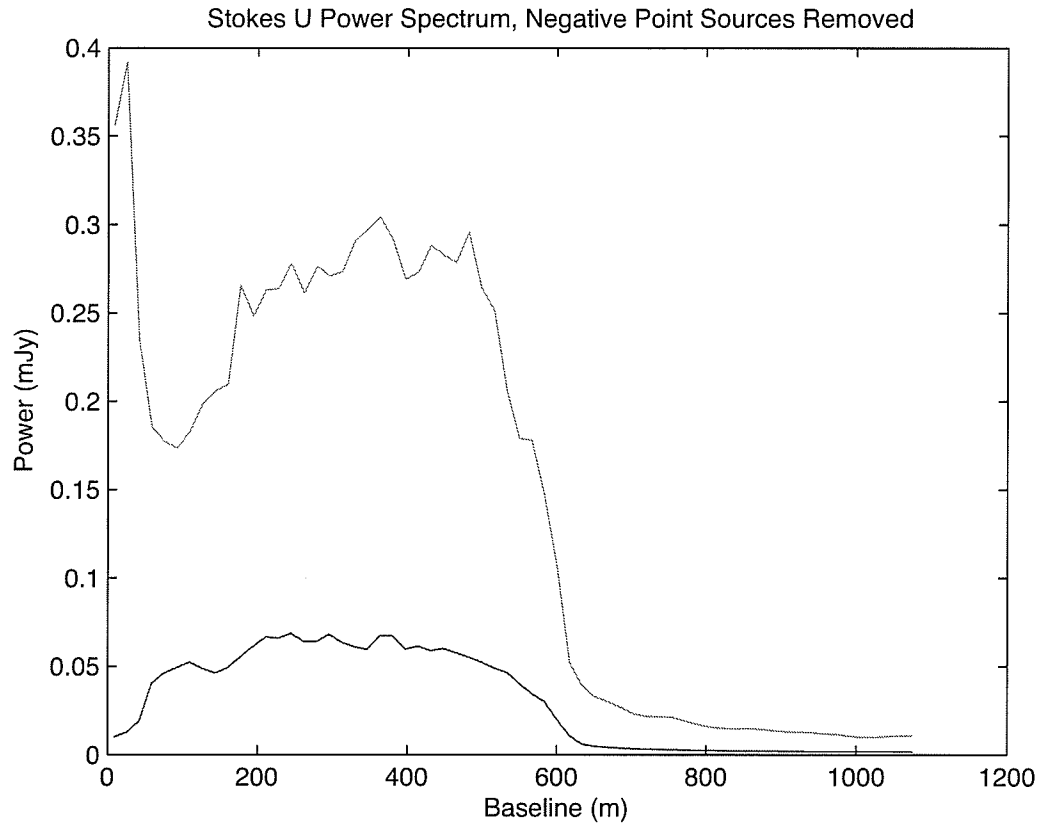


Figure 3.10: Stokes U power spectra where the spectrum of the real data has negative point sources removed. Note the red line is the data mosaic and the blue line is the synthetic mosaic.

3.3 Validation of Technique: Trials with other Optimizers

The Qubist package includes other optimizers which could be effective in solving the seven-parameter problem which is presented. To demonstrate the robust nature of genetic algorithms, the problem was approached with the other optimizers available. Results from the other optimizers in the package are compared to those of Ferret in the following sections.

Details about the type of optimizer used as well as the features of the optimizers in the Qubist package will be discussed. A more detailed description of the package and its contents can be found in the Qubist user guide (3).

3.3.1 Locust

Particle swarm optimizers (PSO) are based on swarm intelligence and the social behavior of flocking birds or schools of fish. Like a genetic algorithm, PSOs begin with a population of random solutions and search a space generation by generation, however in a PSO potential solutions swarm the space as particles and find the best solution by (15):

- Keeping track of the position of the best solution a particle has achieved in the solution space.
- Knowing the best solution found in the particles neighborhood.
- Keeping track of the best solution that any particle in the solution space has achieved so far.

Locust is a PSO in the Qubist package which is capable of solving multi-objective problems. While not as sophisticated as Ferret, it serves as one of the primary optimizers in the package, and is able to obtain solutions for this problem which are nearly, or as good, as those produced by ferret. These results are displayed in tables 3.3 and 3.4, and are done for ten fields in Stokes Q and U.

3. RESULTS

Field Name	Antenna Temperatures (K)	Chi-squared
EN02	69.02, 68.03, 55.64, 56.85, 88.80, 72.83, 52.25	3.25
EN03	70.33, 62.29, 50.46, 52.04, 85.63, 71.60, 52.97	2.70
EN04	55.22, 54.29, 48.04, 50.04, 79.23, 64.19, 45.66	8.46
EN05	63.71, 48.20, 43.73, 44.52, 85.49, 68.76, 49.34	2.76
EN06	61.70, 54.01, 49.96, 50.49, 82.23, 69.39, 46.26	2.11
EN07	67.27, 56.07, 46.20, 46.79, 86.88, 71.41, 49.82	2.48
EN08	70.14, 63.46, 52.52, 54.26, 89.94, 72.53, 52.93	2.63
EN09	61.77, 51.80, 44.51, 48.79, 80.41, 62.32, 45.96	2.27
EN10	66.85, 50.57, 45.045, 47.78, 83.68, 65.12, 47.96	2.53
EN11	63.10, 56.01, 45.19, 45.72, 84.75, 68.47, 48.46	1.94

Table 3.3: Locust System Temperature Results: Stokes Q - Temperature and fitness values obtained by using the Locust optimizer.

Field Name	Antenna Temperatures (K)	Chi-squared
EN02	71.86, 65.20, 53.66, 54.56, 89.50, 75.43, 53.55	2.61
EN03	66.31, 65.98, 54.59, 56.76, 81.82, 65.80, 49.22	2.64
EN04	57.45, 53.92, 46.82, 47.93, 79.97, 65.45, 45.42	8.81
EN05	62.82, 47.77, 45.20, 43.79, 83.80, 68.83, 48.64	2.79
EN06	62.17, 53.20, 49.21, 48.80, 81.68, 70.89, 47.48	2.57
EN07	64.09, 58.77, 48.39, 49.39, 83.70, 67.63, 47.61	2.53
EN08	71.25, 63.64, 52.48, 54.44, 89.99, 73.56, 53.22	2.64
EN09	61.39, 51.73, 44.69, 47.04, 80.93, 62.89, 45.84	2.06
EN10	68.86, 49.00, 42.41, 45.06, 86.10, 68.76, 50.07	2.54
EN11	66.02, 52.84, 43.21, 43.05, 89.14, 72.61, 51.29	1.52

Table 3.4: Locust: Stokes U - Temperature and fitness values obtained by using the Locust optimizer.

3.3.2 Anvil and SAMOSA

Anvil, which is also a multi-objective optimizer, is a simulating annealing (SA) code. Simulated annealing is based on annealing in metallurgy, in which the cooling of metal is slow to minimize lattice imperfections. In the code, particles are at a high energy and as they ‘cool’ they are able to search the space for a global solution.

SAMOSA or “Simple Approach to a Multi-Objective Simplex Algorithm” is based on a Nelder-Mead simplex algorithm. In these types of algorithms, a simplex, or polygon which has $n+1$ sides searches n dimensions by contorting itself throughout the search space. SAMOSA’s advantage is it’s speed. It is mainly used as a polisher for Ferret and Locust.

The Anvil and SAMOSA optimizers were used to derive system temperatures for ten EN fields in Stokes U. While they don’t produce results with as favorable a χ^2 value as Ferret or Locust, which are more suited to this type of problem, they do produce reasonable results (3).

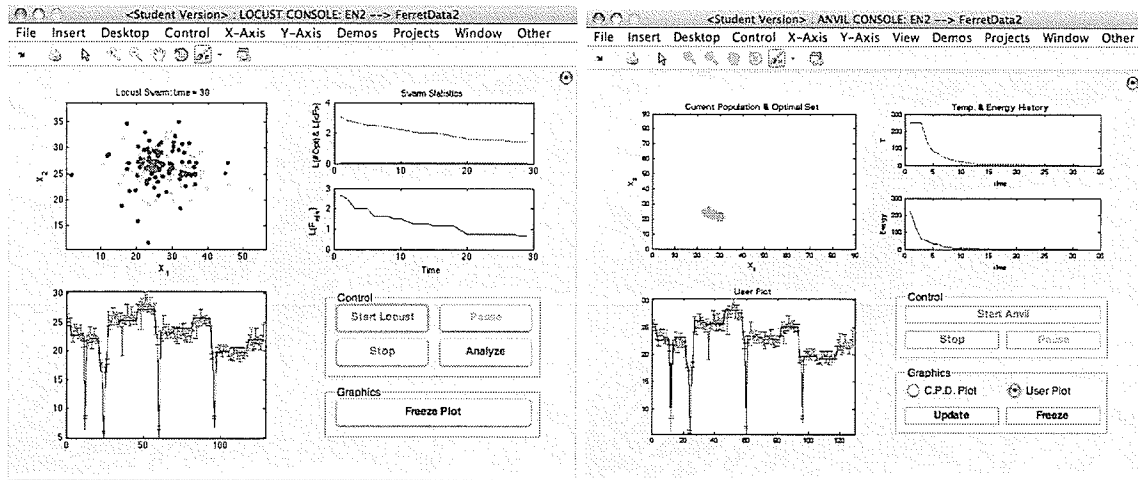


Figure 3.11: Left: The Locust optimizer environment. Right: The Anvil optimizer environment.

3. RESULTS

Field Name	Antenna Temperatures (K)	Chi-squared
EN02	67.52, 66.63, 56.87, 57.54, 87.81, 71.43, 50.43	2.59
EN03	68.67, 63.28, 52.82, 55.06, 84.31, 67.95, 50.60	2.48
EN04	40.26, 76.87, 65.70, 66.87, 56.13, 47.09, 32.02	11.26
EN05	44.71, 66.68, 62.66, 63.17, 61.49, 49.34, 33.90	4.15
EN06	51.36, 62.57, 58.88, 59.04, 68.95, 59.47, 40.54	3.15
EN07	56.26, 66.96, 55.49, 55.64, 73.39, 59.12, 42.06	2.75
EN08	68.28, 66.00, 54.61, 55.76, 86.56, 70.68, 52.11	2.57
EN09	49.41, 62.82, 54.76, 57.27, 66.10, 51.23, 37.42	2.56
EN10	52.55, 65.18, 55.93, 59.47, 64.38, 51.77, 38.08	2.64
EN11	45.76, 77.10, 63.08, 62.40, 62.02, 49.76, 35.29	2.47

Table 3.5: SAMOSA System Temperature Results: Stokes U - Temperature and fitness values obtained by using the Locust optimizer.

Field Name	Antenna Temperatures (K)	Chi-squared
EN02	67.25, 69.82, 57.24, 58.68, 83.97, 72.30, 49.71	2.74
EN03	64.49, 73.44, 62.38, 62.32, 79.23, 64.18, 47.98	2.98
EN04	51.98, 57.64, 51.26, 52.48, 71.98, 62.35, 40.43	9.78
EN05	46.65, 66.32, 60.61, 60.80, 61.06, 51.23, 35.59	4.05
EN06	52.33, 59.27, 54.59, 55.74, 72.95, 67.40, 42.97	3.48
EN07	62.36, 61.52, 54.15, 52.69, 77.46, 59.78, 44.09	3.41
EN08	60.30, 74.68, 61.91, 64.37, 75.40, 62.53, 44.39	3.05
EN09	46.78, 62.44, 56.09, 59.50, 67.64, 51.57, 36.38	3.06
EN10	59.15, 57.00, 49.34, 51.73, 76.77, 60.98, 43.78	2.61
EN11	65.55, 42.76, 33.03, 33.84, 84.98, 68.74, 49.18	2.27

Table 3.6: Anvil System Temperature Results: Stokes U - Temperature and fitness values obtained by using the Anvil optimizer.

3.4 Power Spectra: Stokes Q

For each ELAIS-N1 field, a power spectrum of an image created from the derived system temperatures of that field, is compared to a spectrum of the real field. These results are presented for this section in Stokes Q.

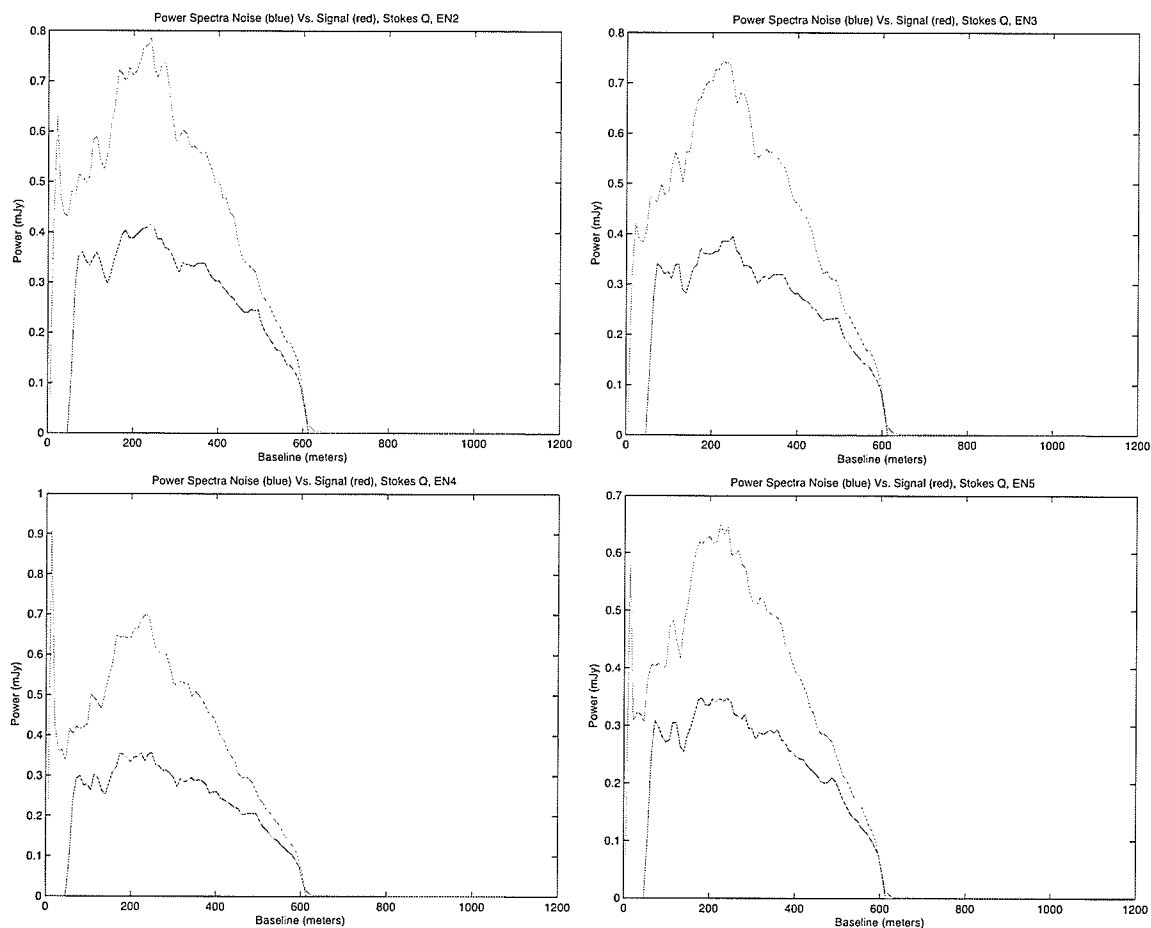


Figure 3.12: Comparison of power spectra EN02-EN05, Stokes Q.

3. RESULTS

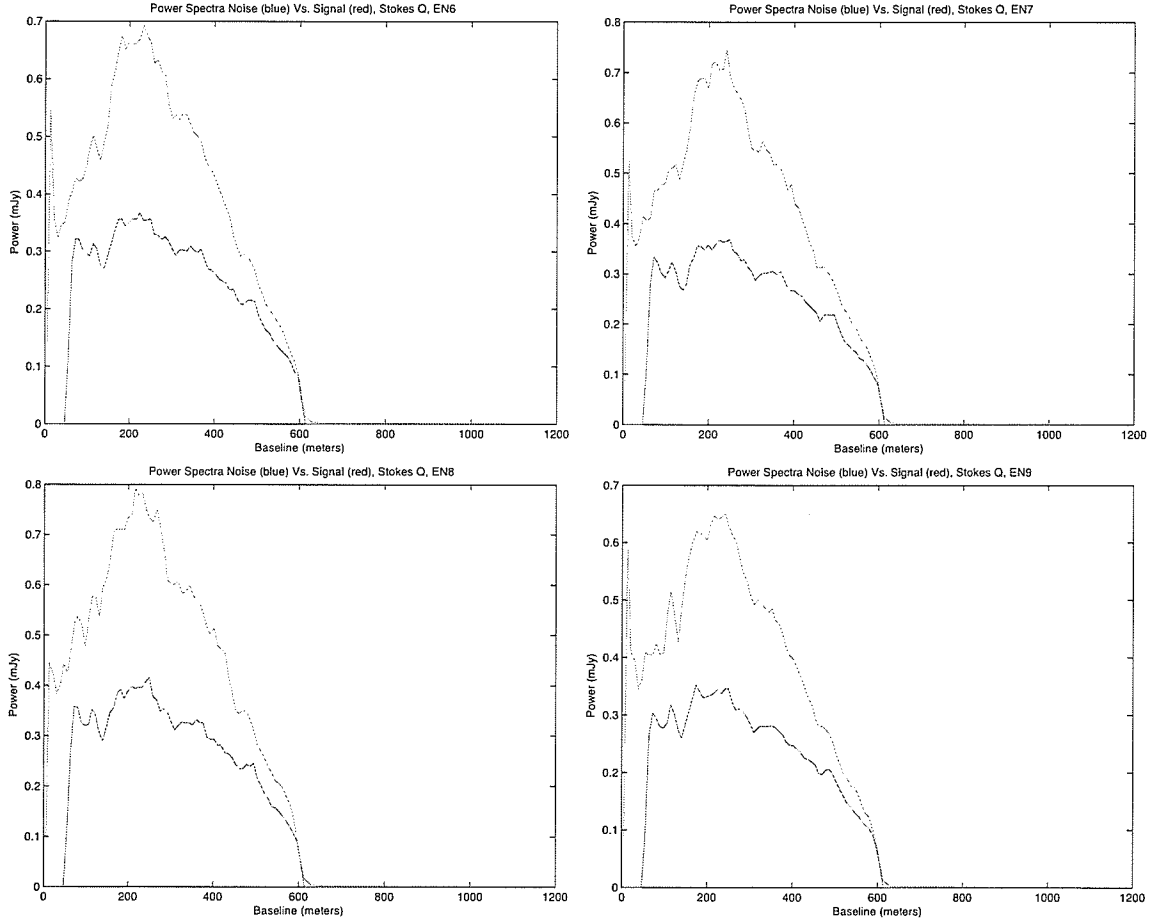


Figure 3.13: Comparison of power spectra EN06-EN09, Stokes Q.

3.4 Power Spectra: Stokes Q

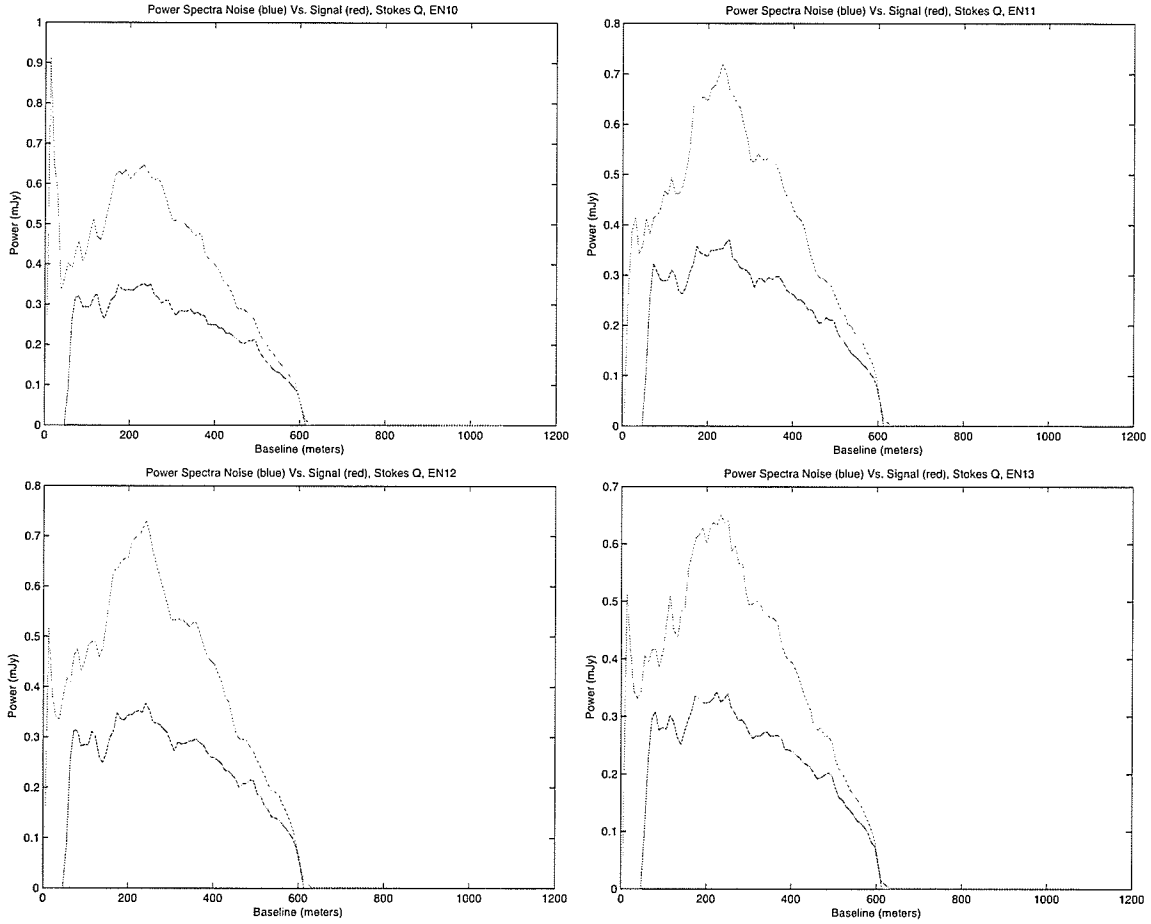


Figure 3.14: Comparison of power spectra EN10-EN13, Stokes Q.

3. RESULTS

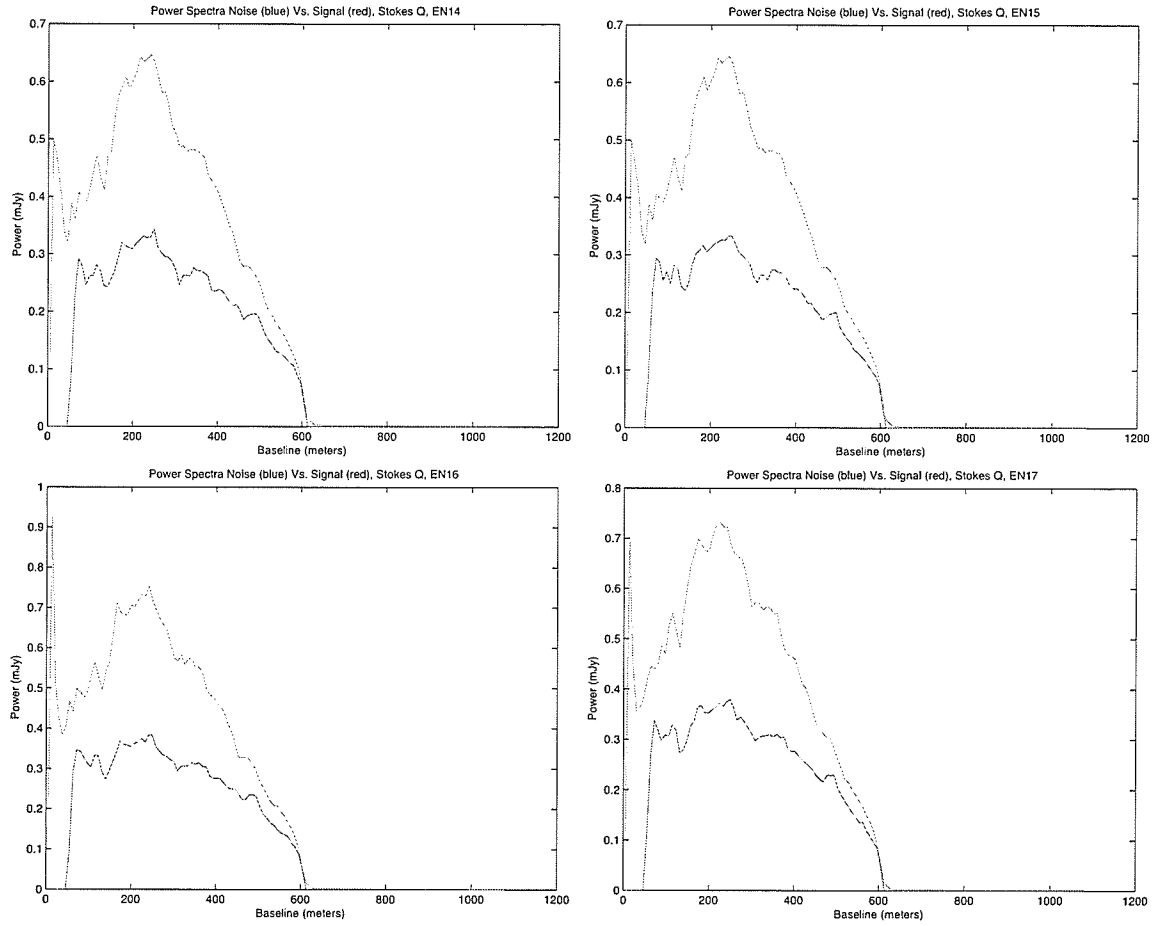


Figure 3.15: Comparison of power spectra EN14-EN17, Stokes Q.

3.4 Power Spectra: Stokes Q

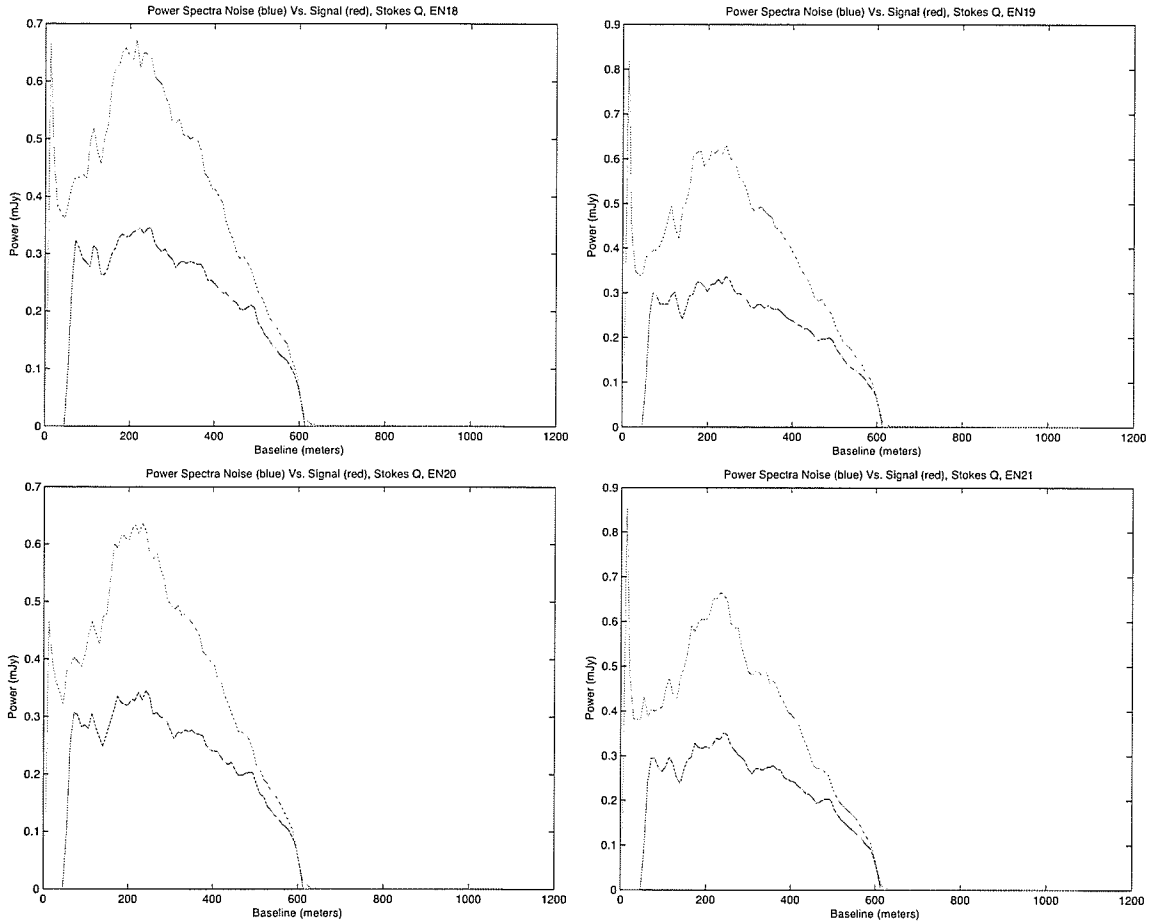


Figure 3.16: Comparison of power spectra EN18-EN21, Stokes Q.

3. RESULTS

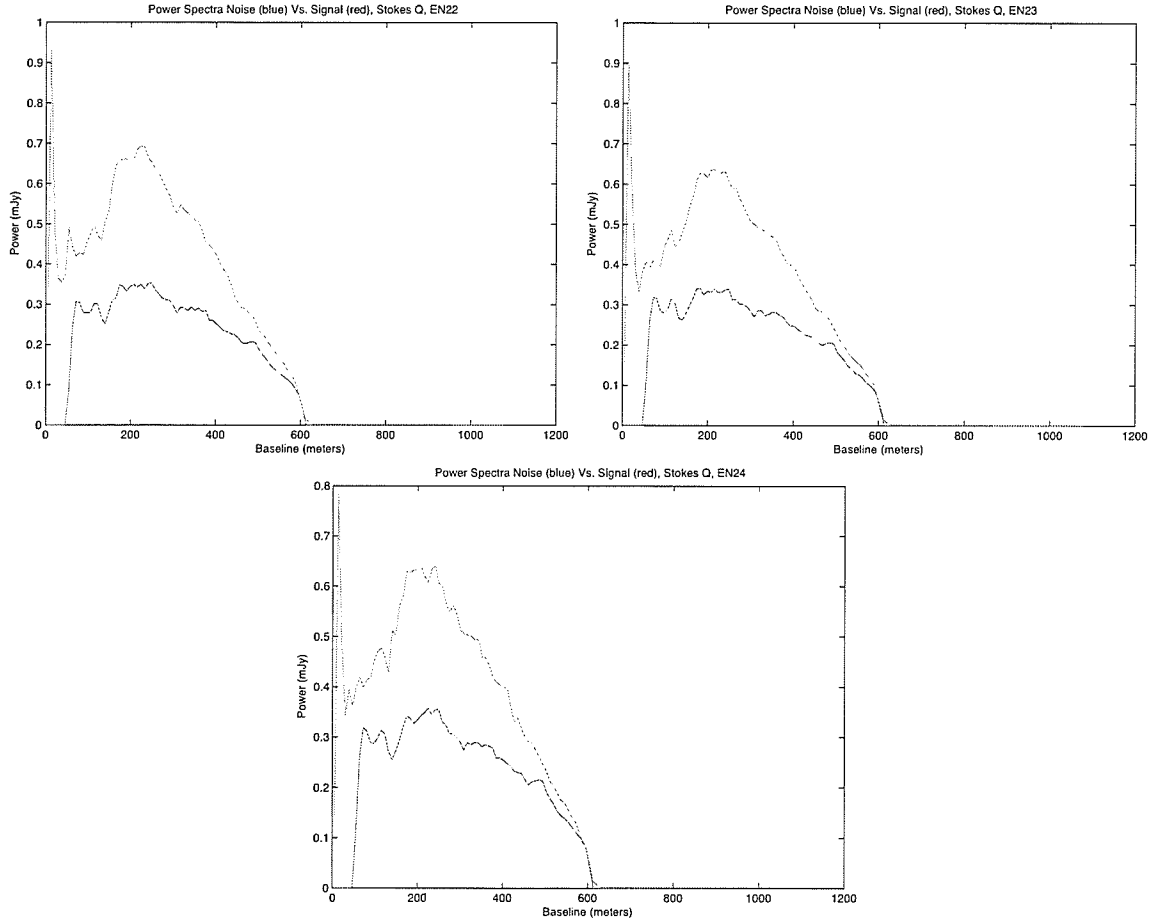


Figure 3.17: Comparison of power spectra EN22-EN24, Stokes Q.

3.4 Power Spectra: Stokes Q

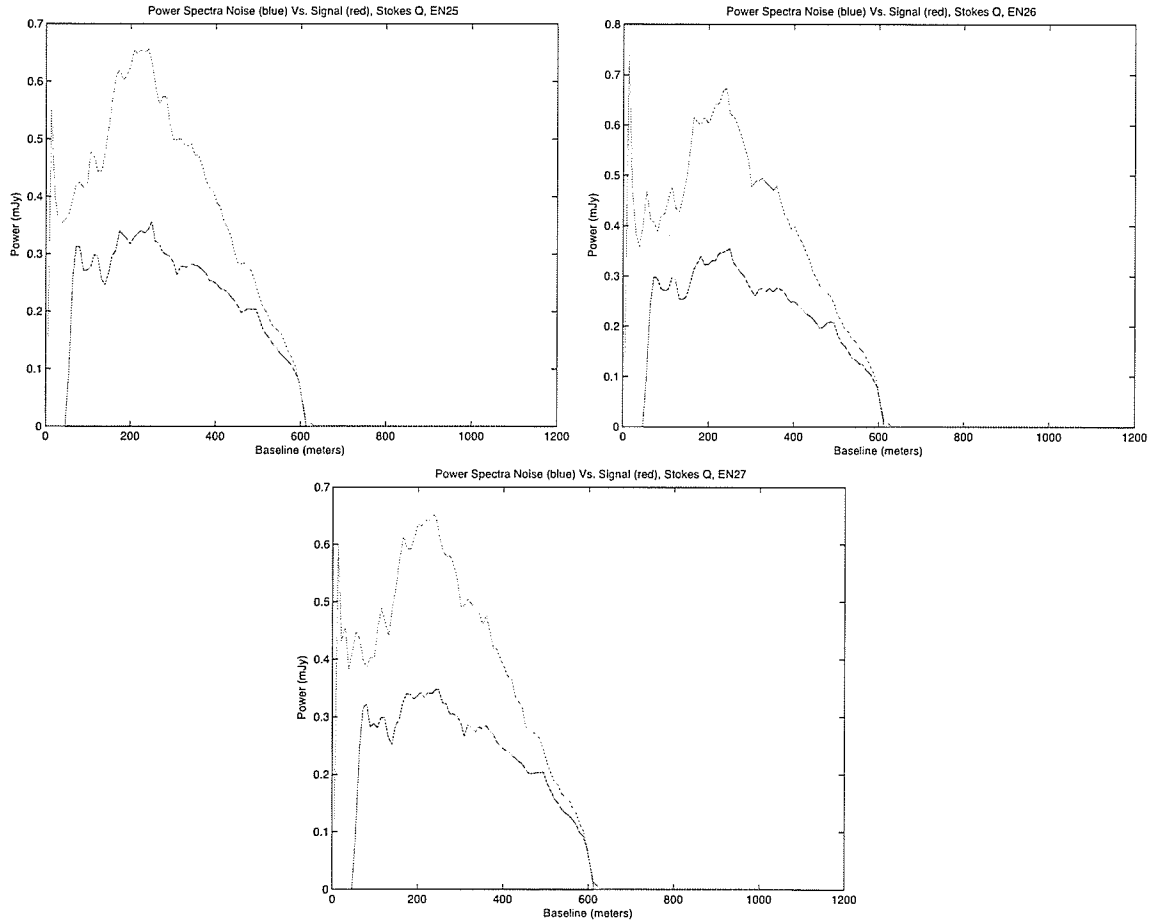


Figure 3.18: Comparison of power spectra EN25-EN27, Stokes Q.

3. RESULTS

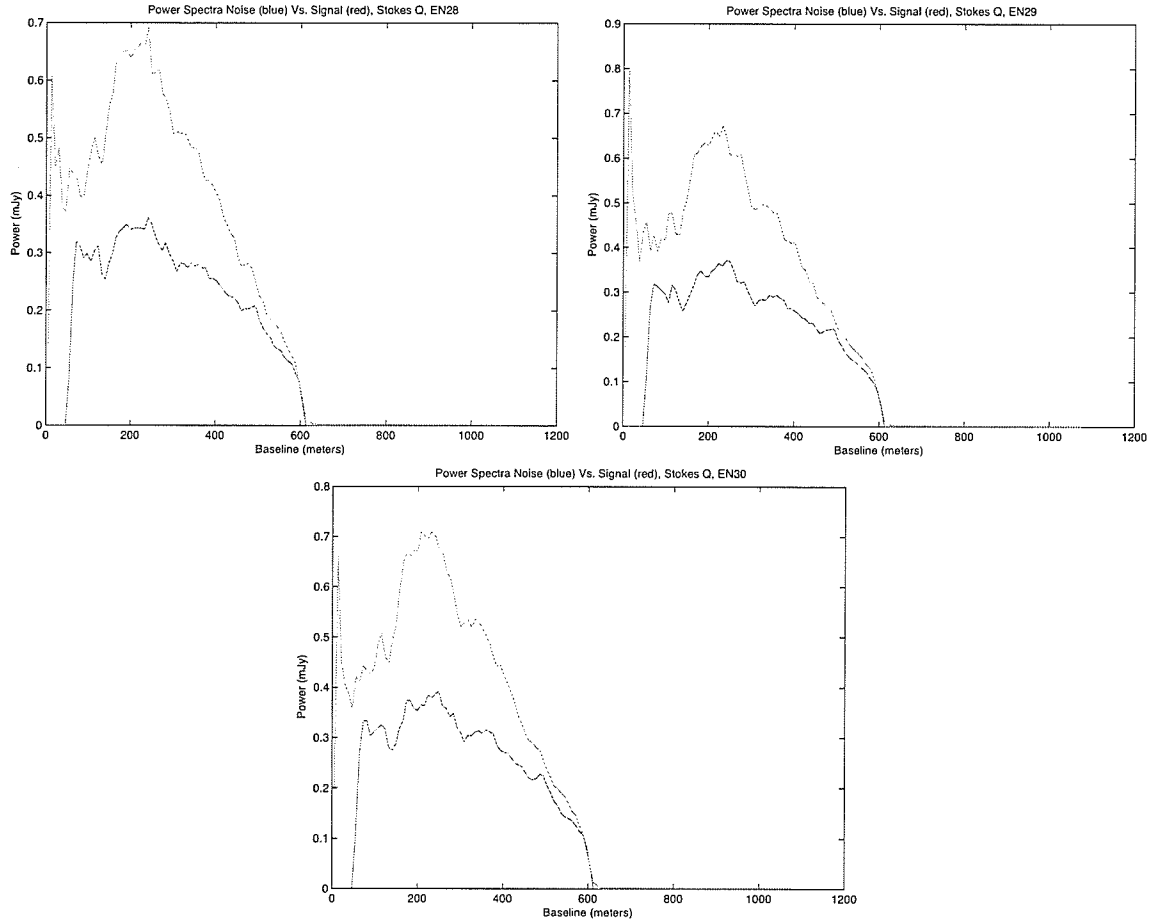


Figure 3.19: Comparison of power spectra EN28-EN30, Stokes Q.

3.5 Power Spectra: Stokes U

The same power comparison of power spectra is done for Stokes U.

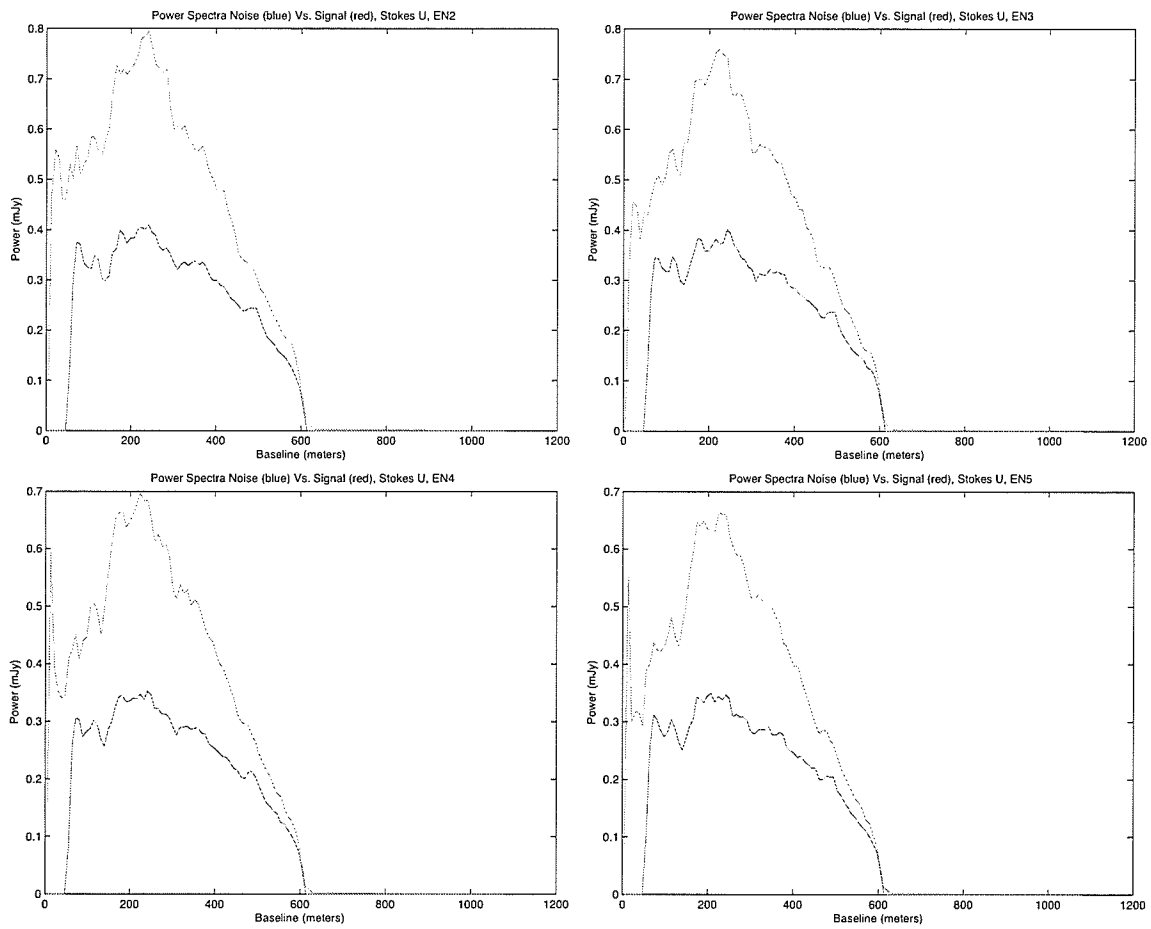
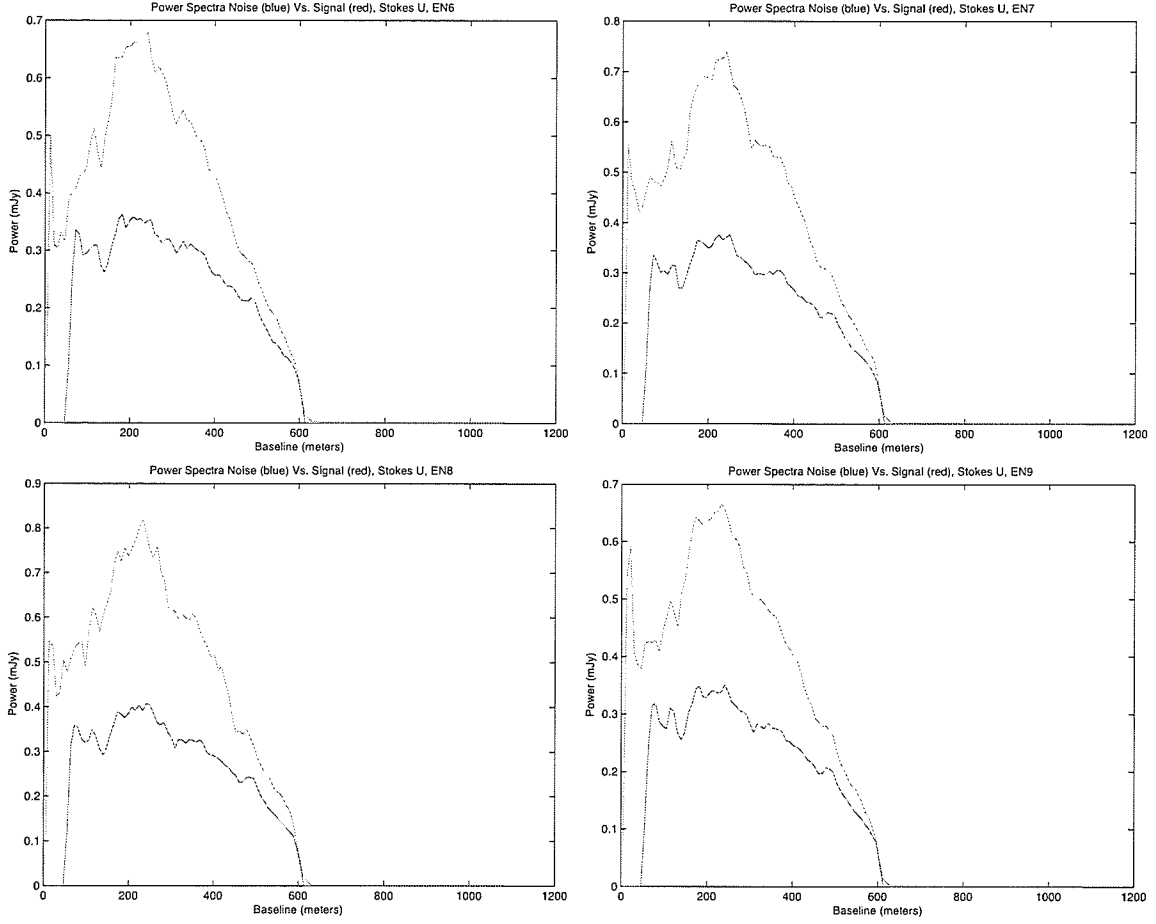


Figure 3.20: Comparison of power spectra EN02-EN05, Stokes U.

3. RESULTS



1

Figure 3.21: Comparison of power spectra EN06-EN09, Stokes U.

3.5 Power Spectra: Stokes U

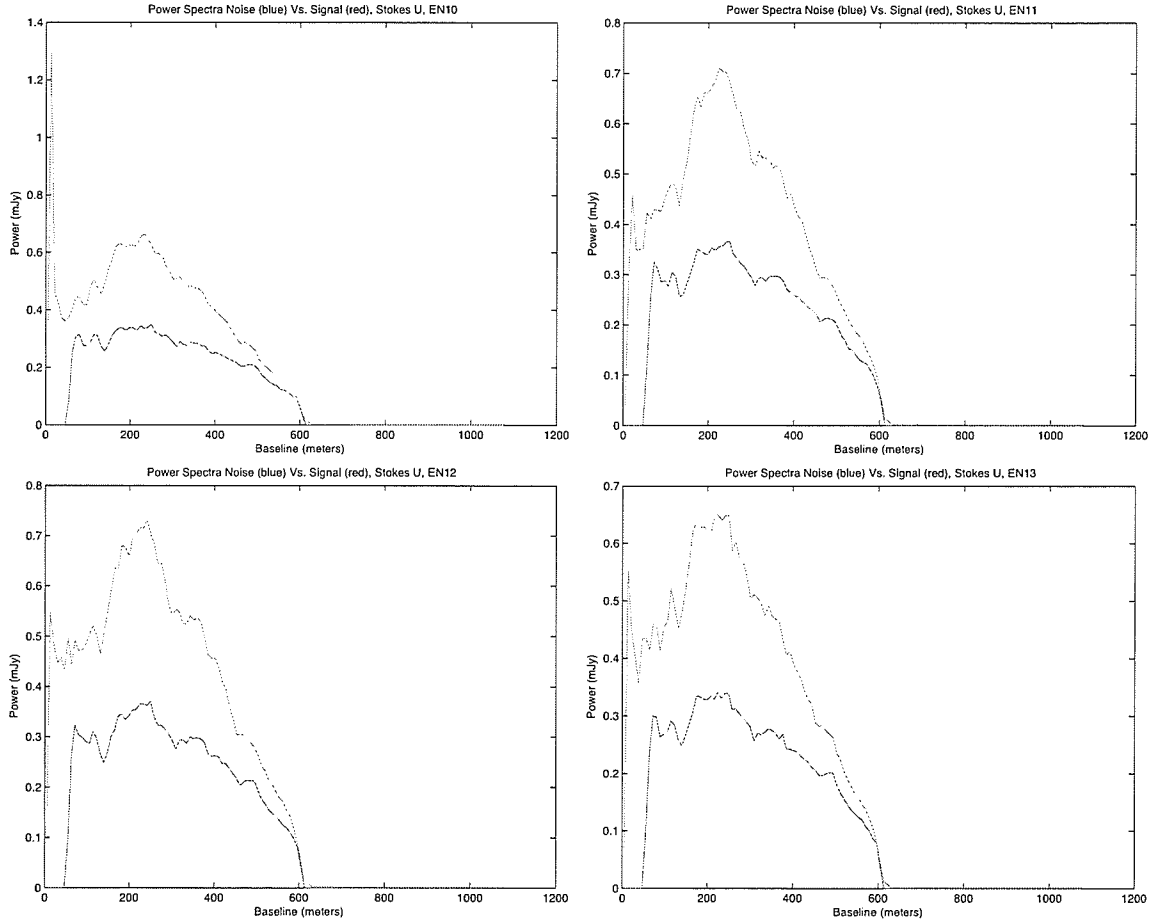


Figure 3.22: Comparison of power spectra EN10-EN13, Stokes U.

3. RESULTS

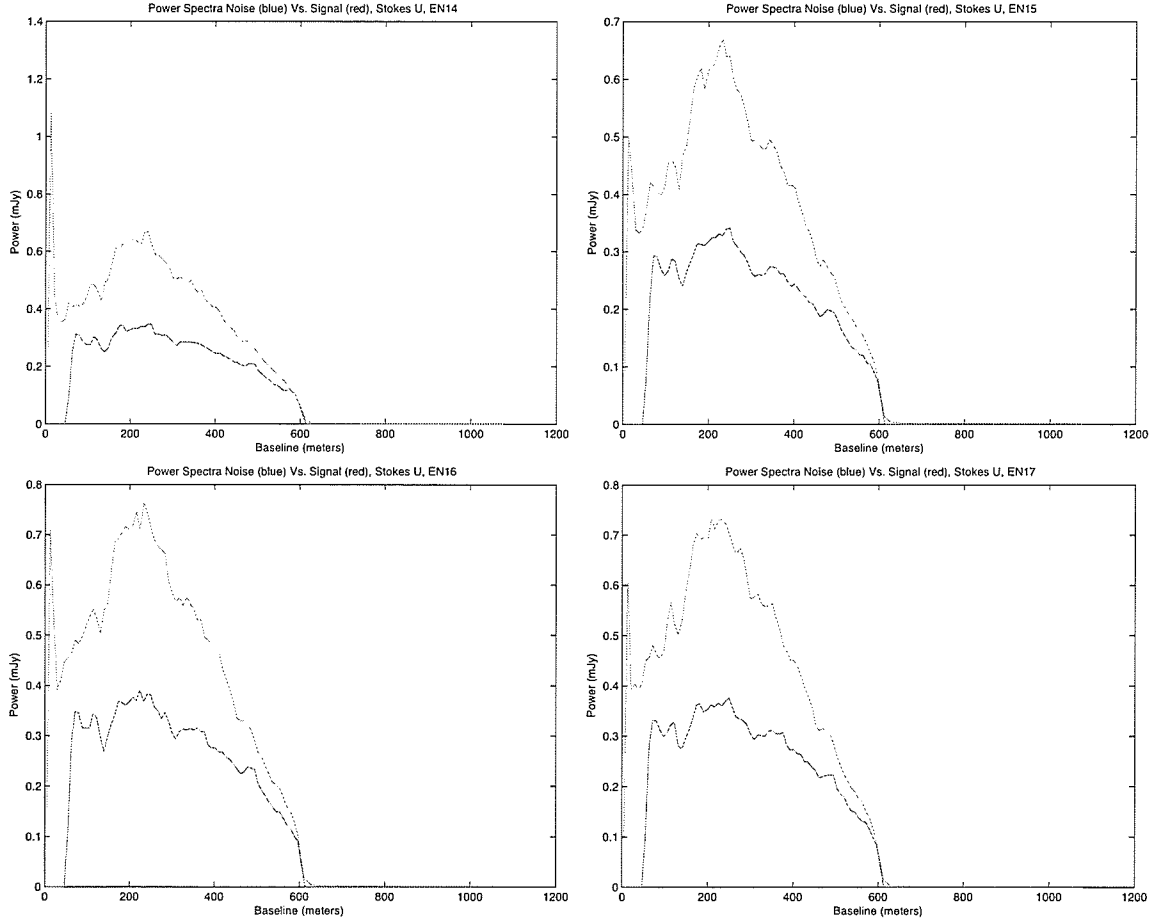


Figure 3.23: Comparison of power spectra EN14-EN17, Stokes U.

3.5 Power Spectra: Stokes U

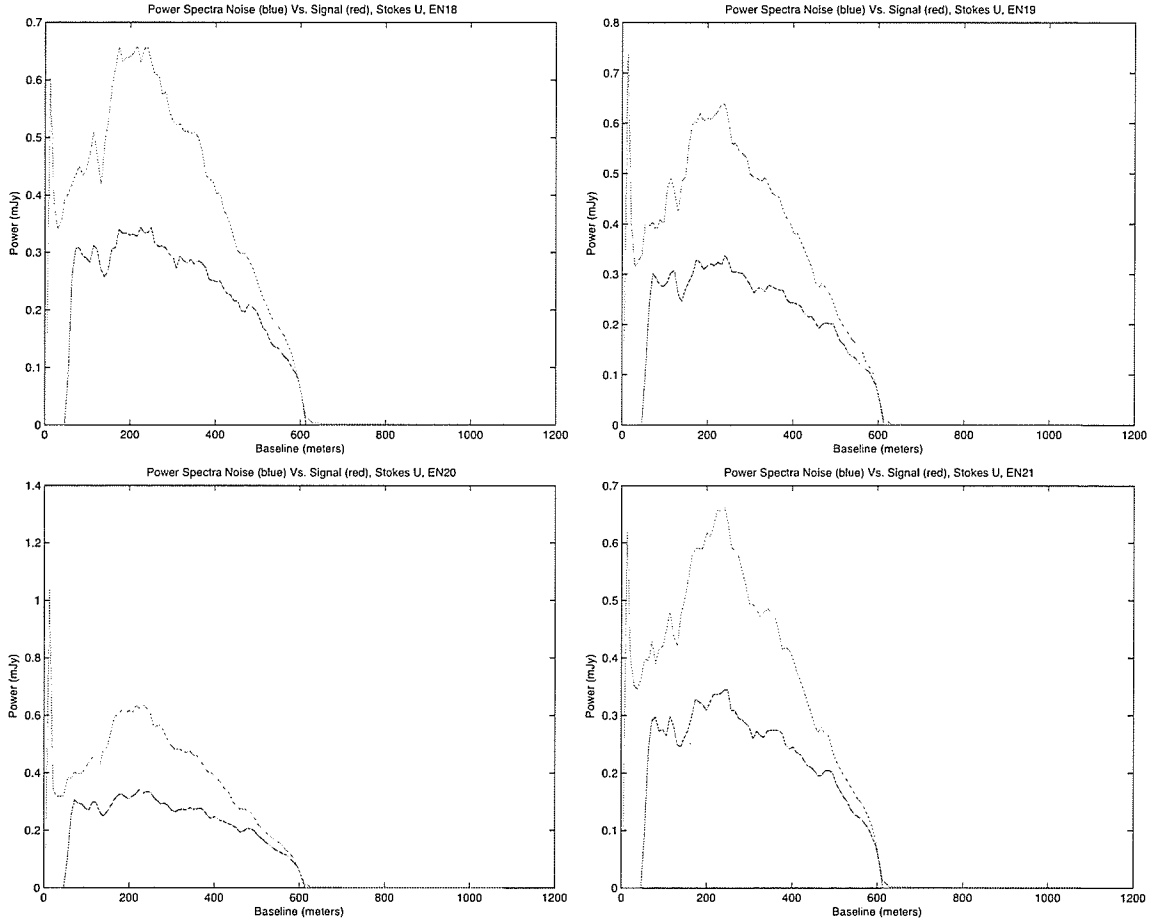


Figure 3.24: Comparison of power spectra EN18-EN21 Stokes U.

3. RESULTS

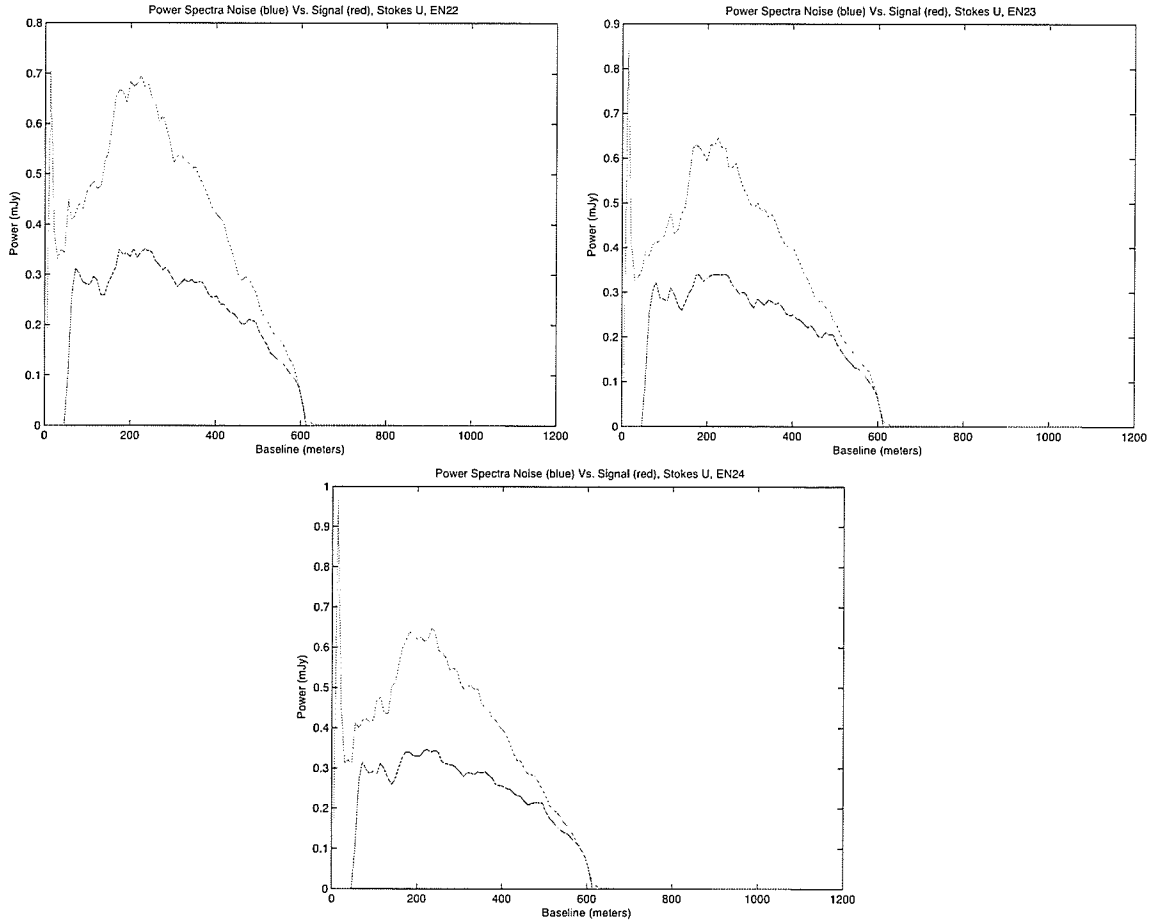


Figure 3.25: Comparison of power spectra EN22-EN24, Stokes U.

3.5 Power Spectra: Stokes U

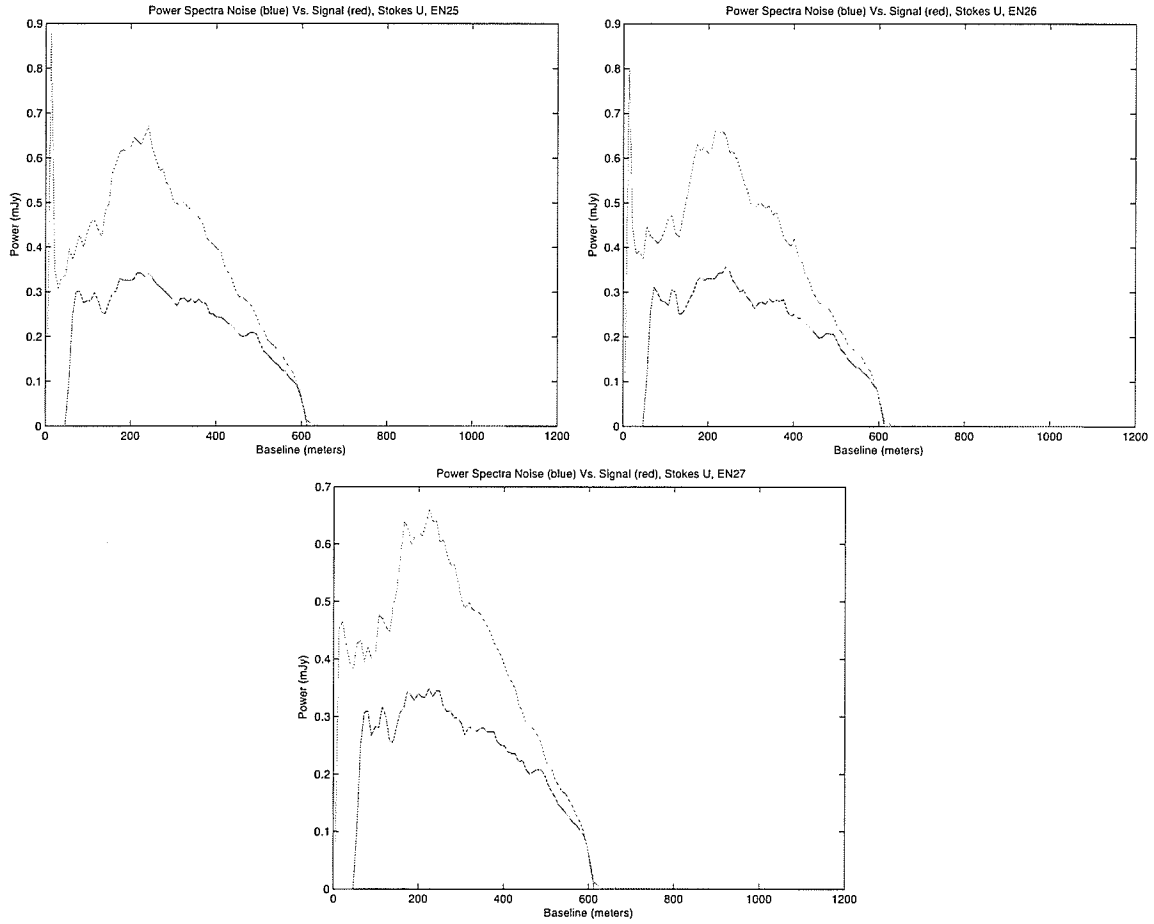


Figure 3.26: Comparison of power spectra EN25-EN27, Stokes U.

3. RESULTS

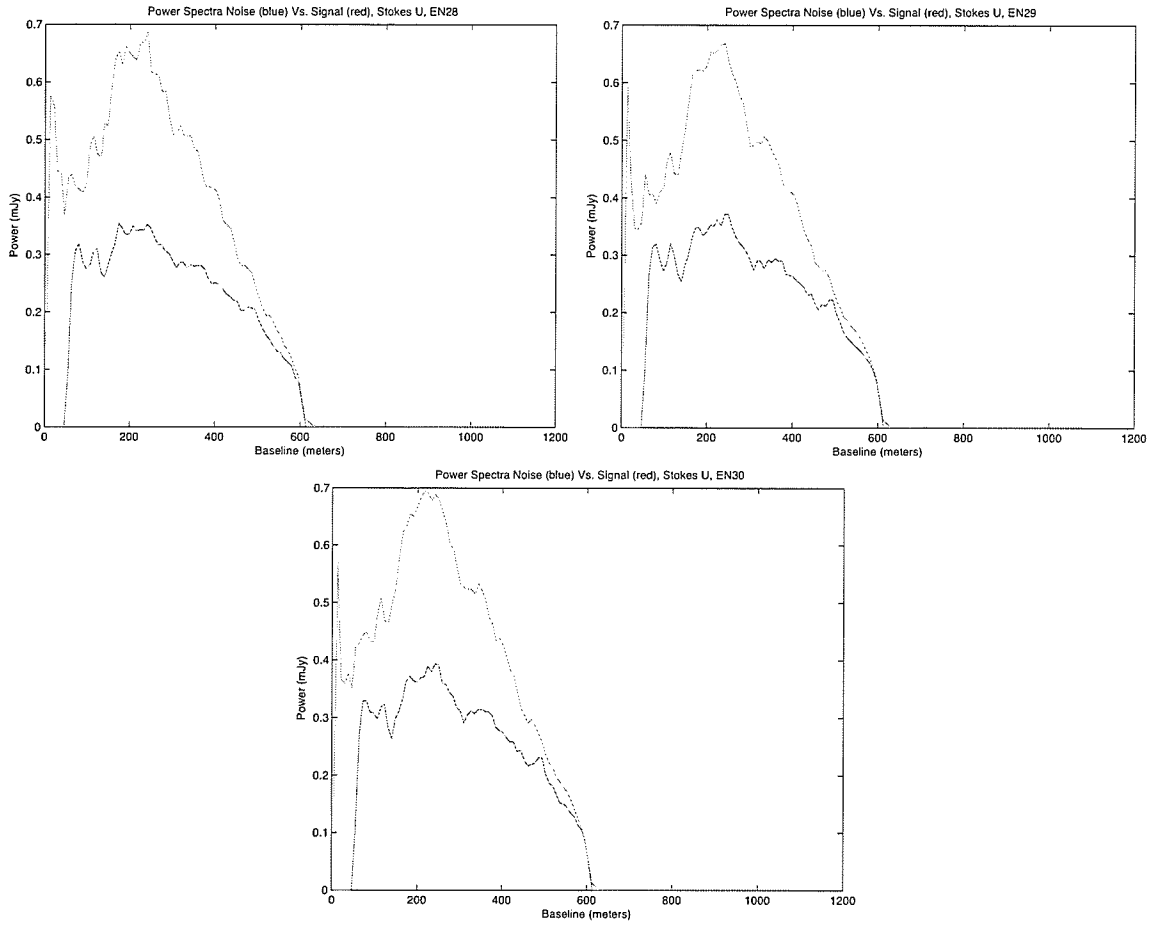


Figure 3.27: Comparison of power spectra EN28-EN30, Stokes U.

3.6 Ferret Solution Surfaces: Stokes Q

For problems with multiple parameters, Ferret is able to output a family of solutions within a user specified value of the optimal (in this case, one). These surfaces are mapped out generation by generation as Ferret searches the parameter space.

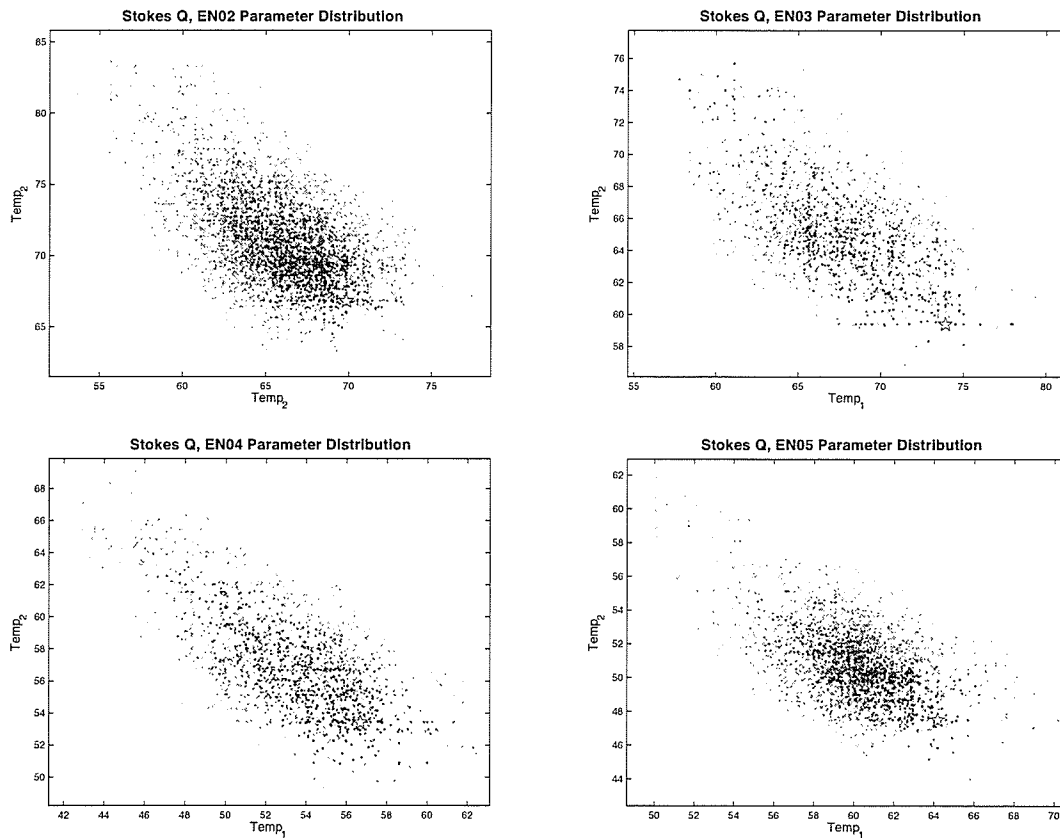


Figure 3.28: Family of solutions EN02-EN05, Stokes Q.

3. RESULTS

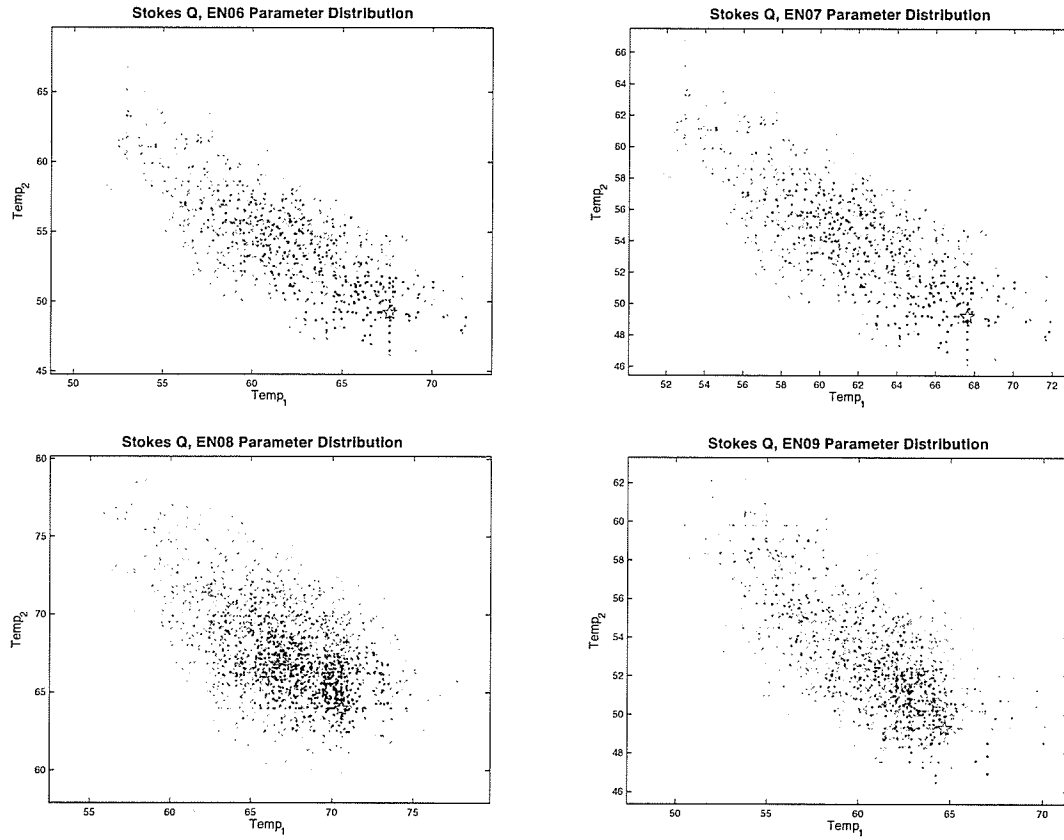


Figure 3.29: Family of solutions EN06-EN09, Stokes Q.

3.6 Ferret Solution Surfaces: Stokes Q

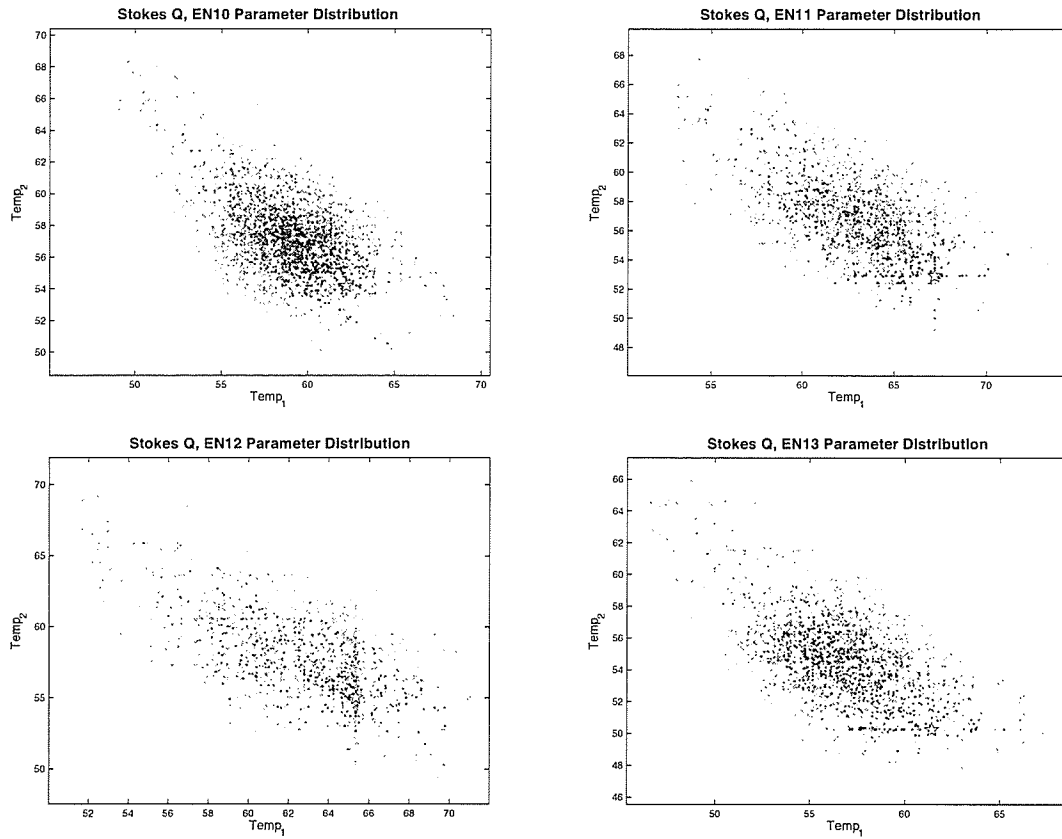


Figure 3.30: Family of solutions EN10-EN13, Stokes Q.

3. RESULTS

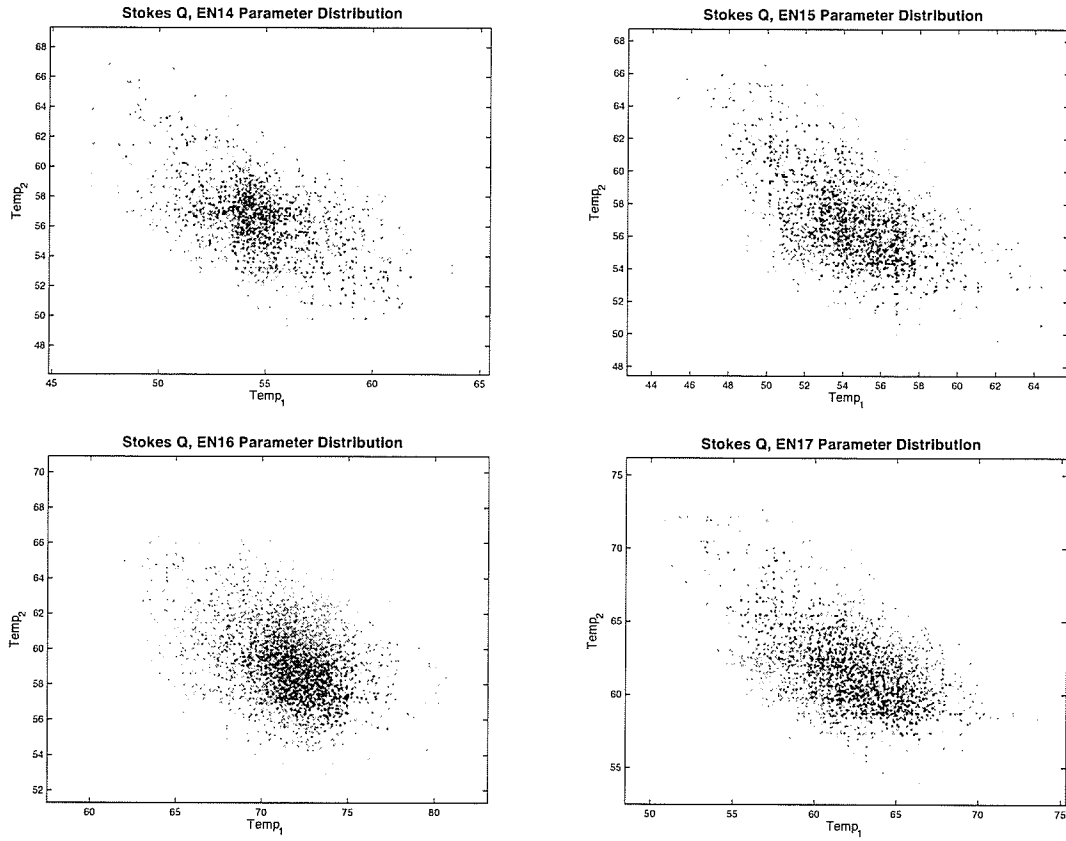


Figure 3.31: Family of solutions EN14-EN17, Stokes Q.

3.6 Ferret Solution Surfaces: Stokes Q

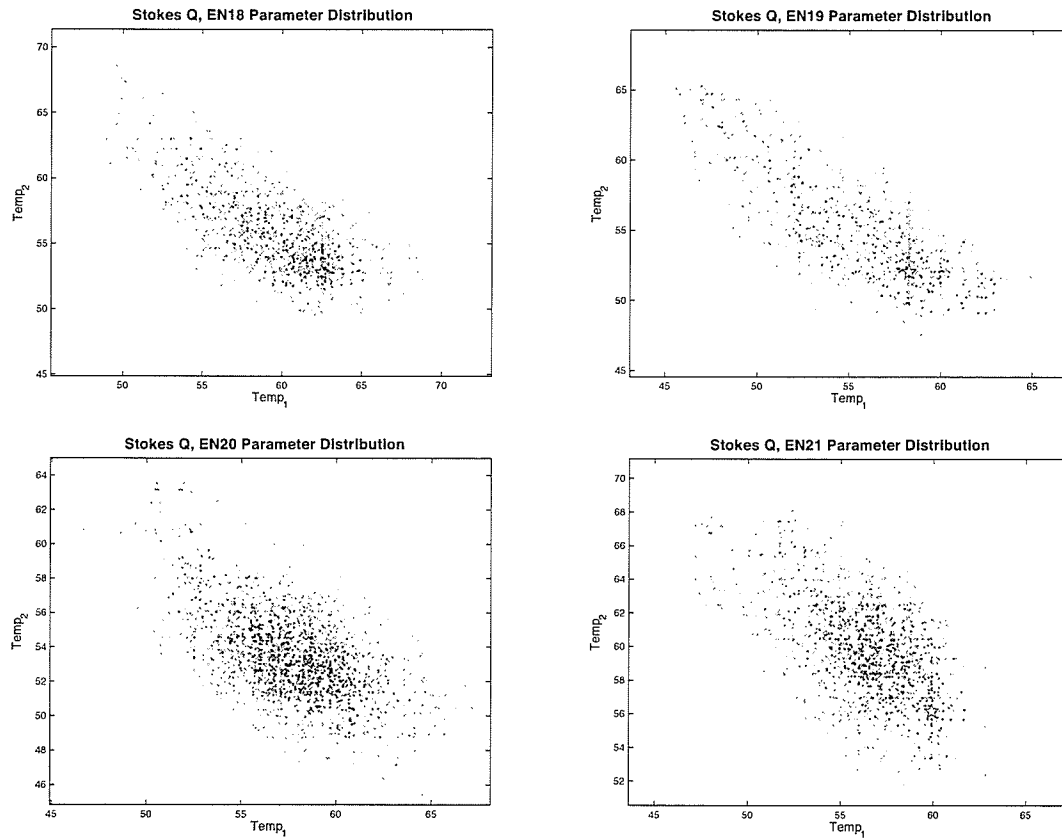


Figure 3.32: Family of solutions EN18-EN21, Stokes Q.

3. RESULTS

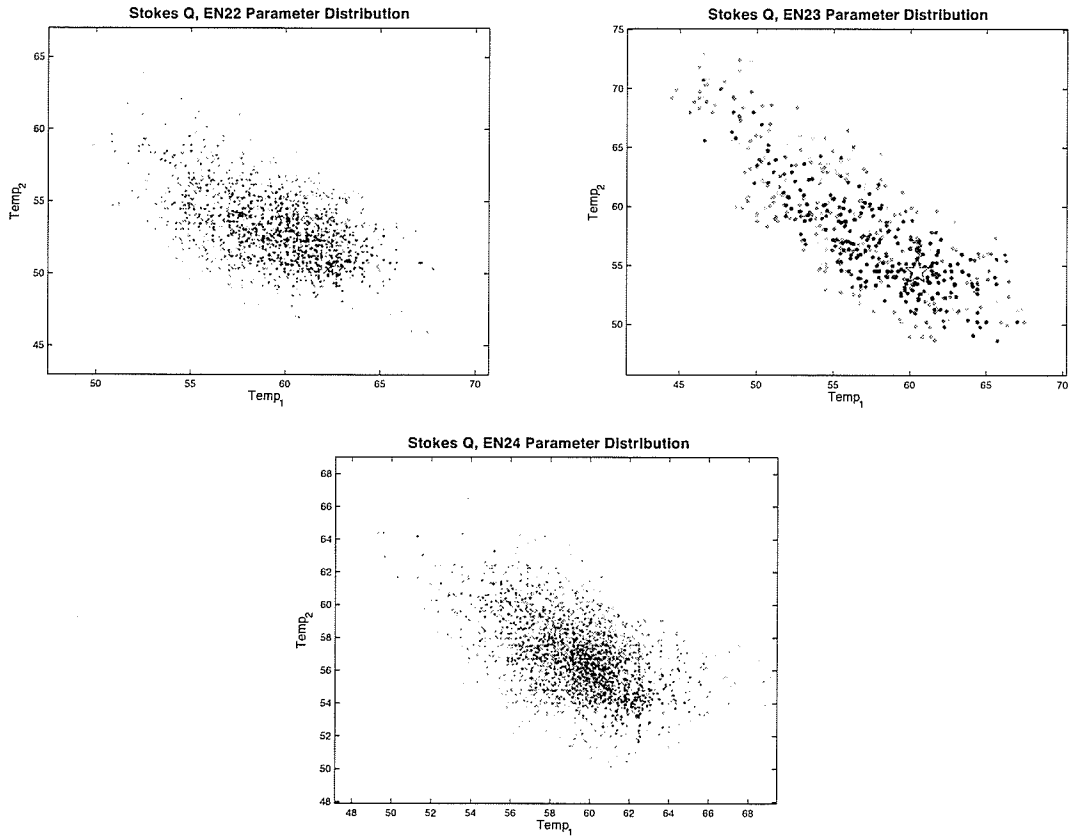


Figure 3.33: Family of solutions EN22-EN24, Stokes Q.

3.6 Ferret Solution Surfaces: Stokes Q

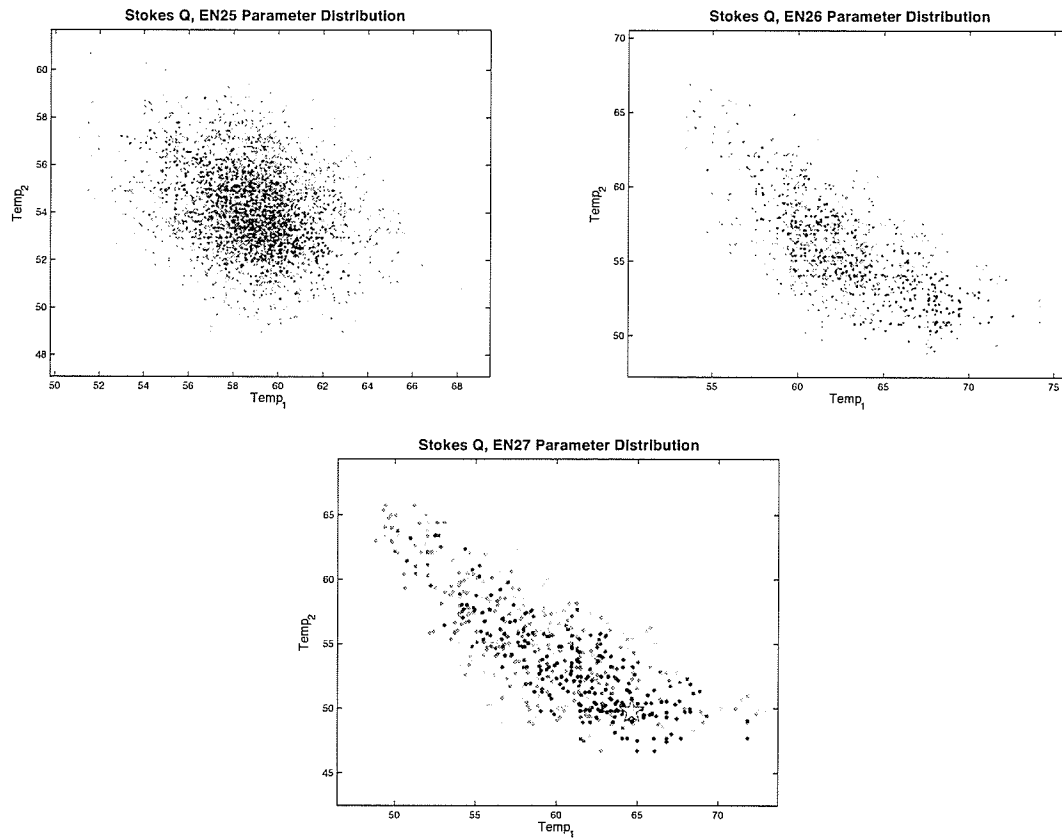


Figure 3.34: Family of solutions EN25-EN27, Stokes Q.

3. RESULTS

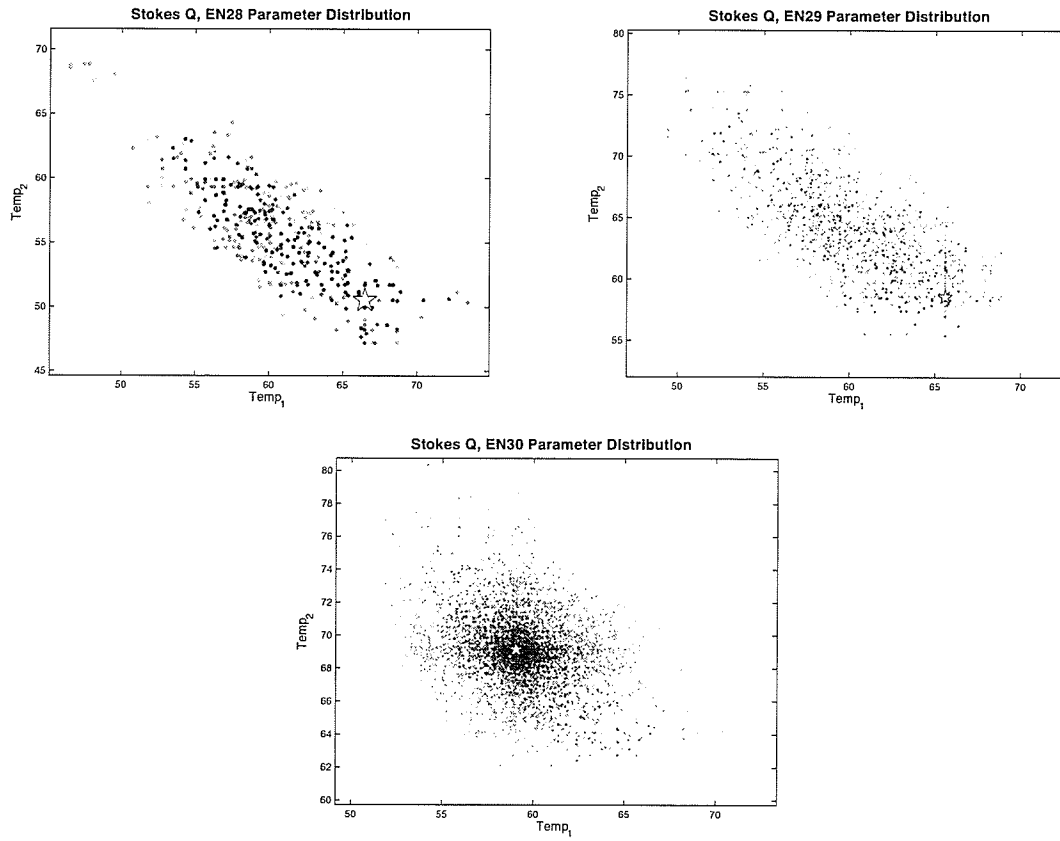


Figure 3.35: Family of solutions EN28-EN30, Stokes Q.

3.7 Ferret Solution Surfaces: Stokes U

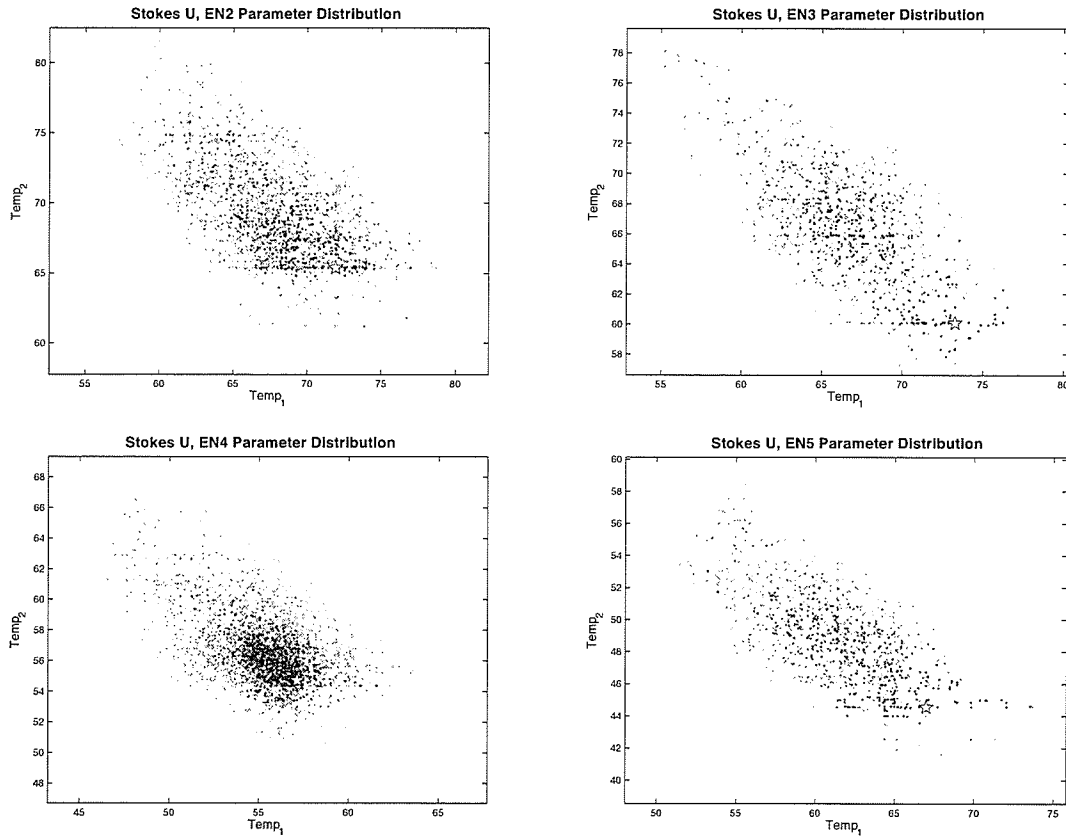


Figure 3.36: Family of solutions EN02-EN05, Stokes U.

3. RESULTS

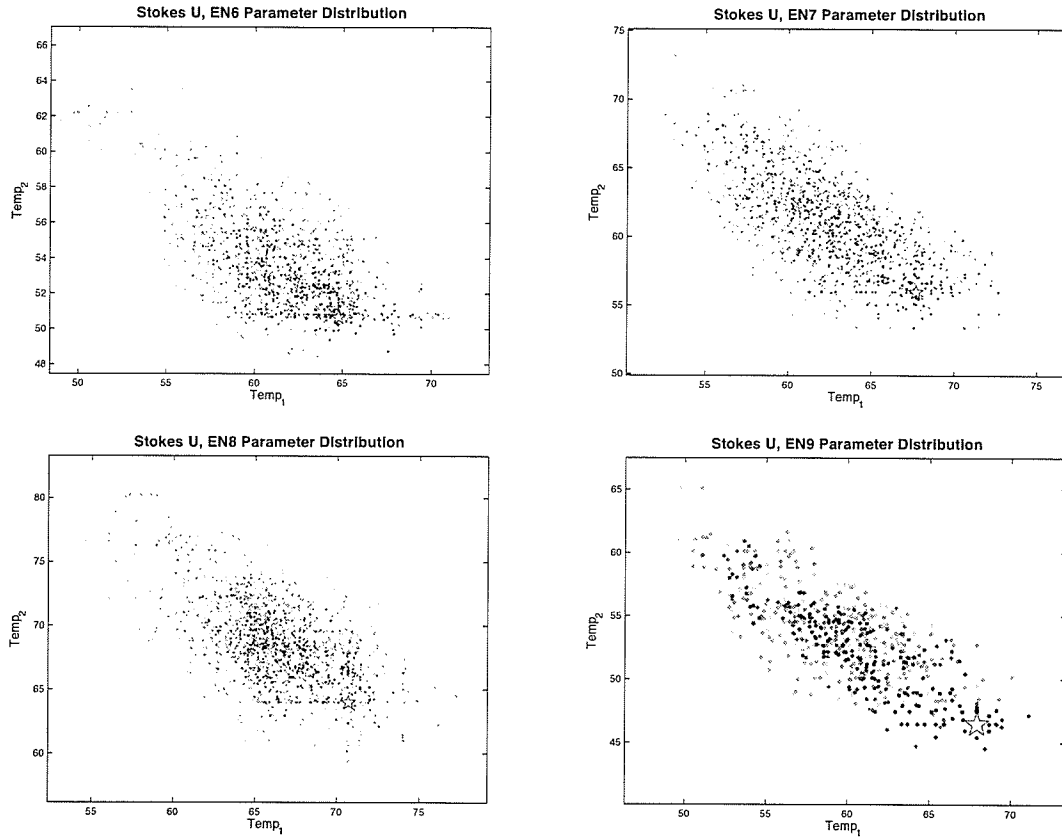


Figure 3.37: Family of solutions EN06-EN09, Stokes U.

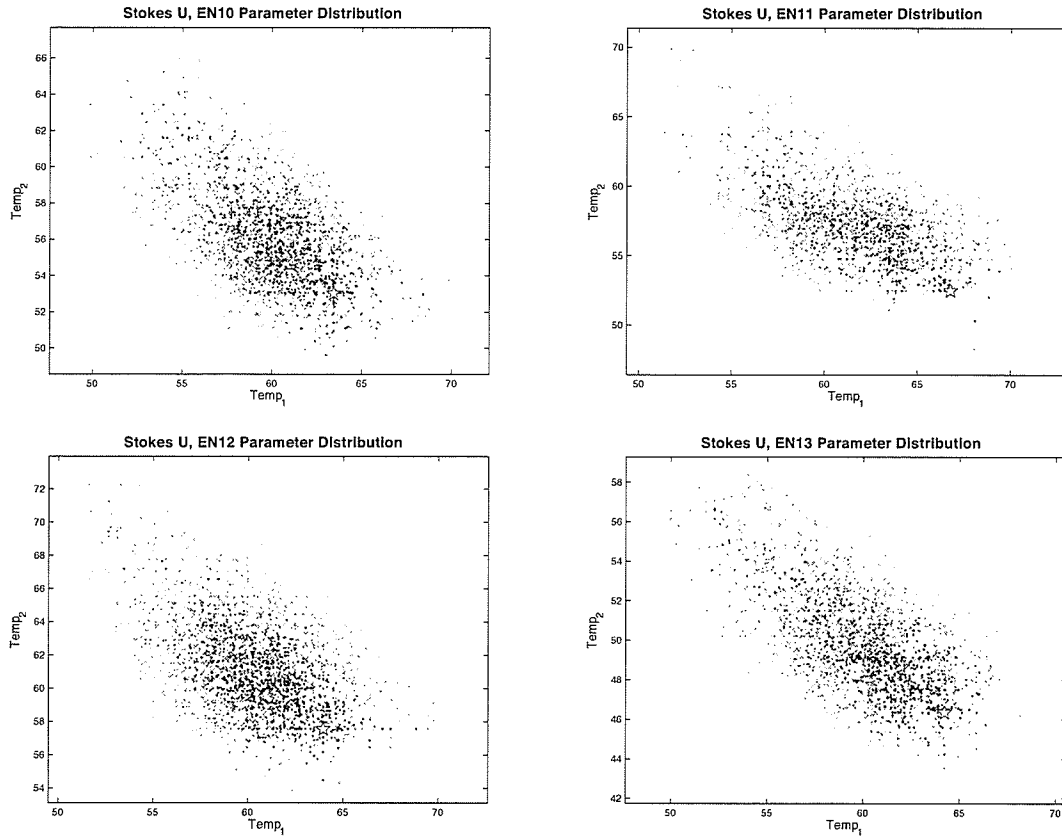


Figure 3.38: Family of solutions EN10-EN13, Stokes U.

3. RESULTS

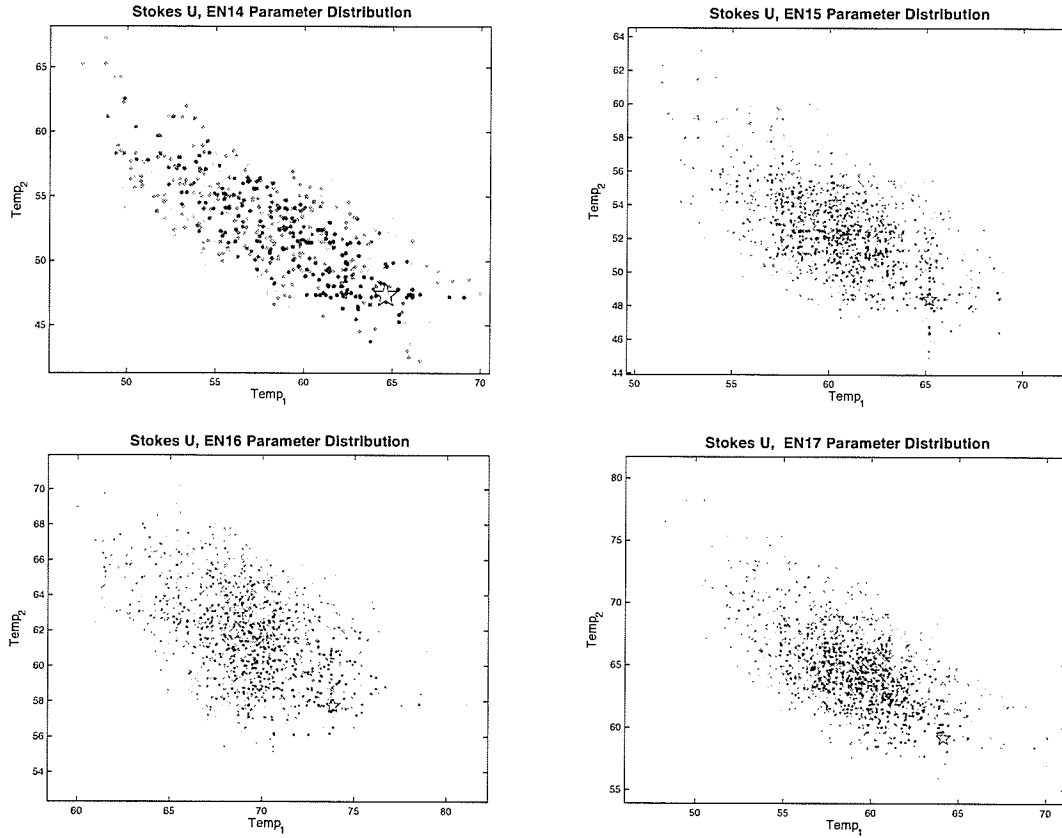


Figure 3.39: Family of solutions EN14-EN17, Stokes U.

3.7 Ferret Solution Surfaces: Stokes U

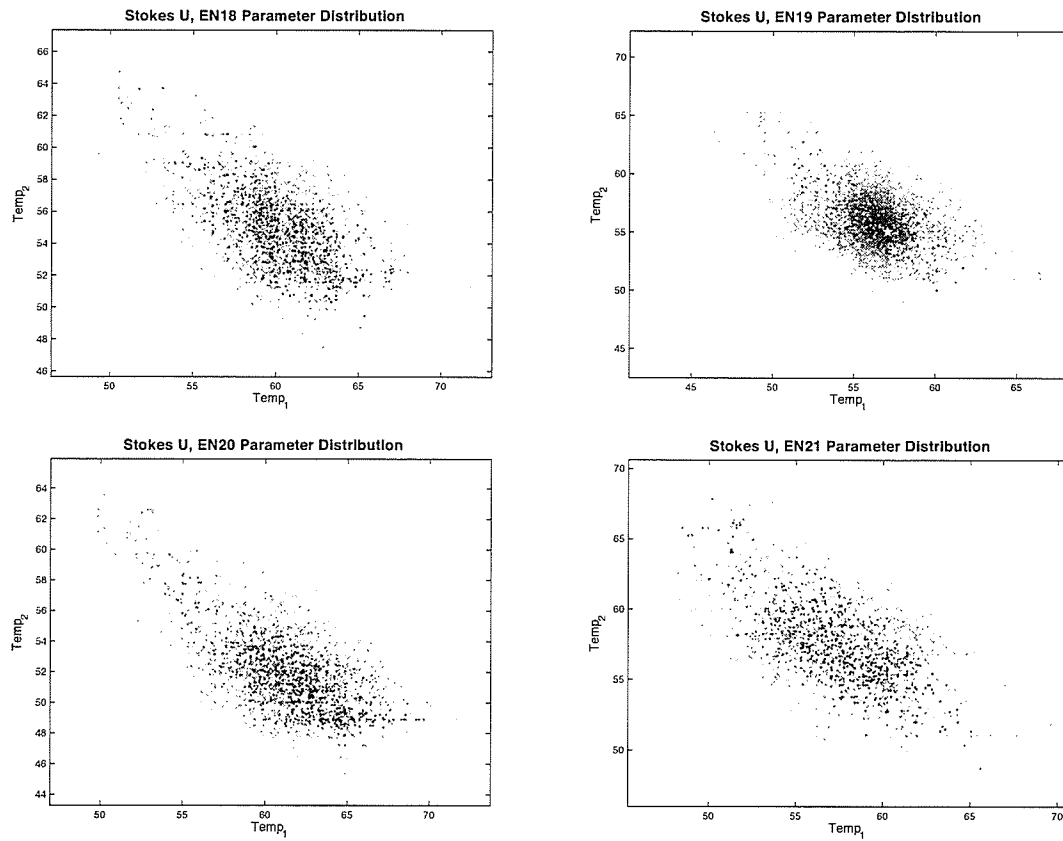


Figure 3.40: Family of solutions EN18-EN21, Stokes U.

3. RESULTS

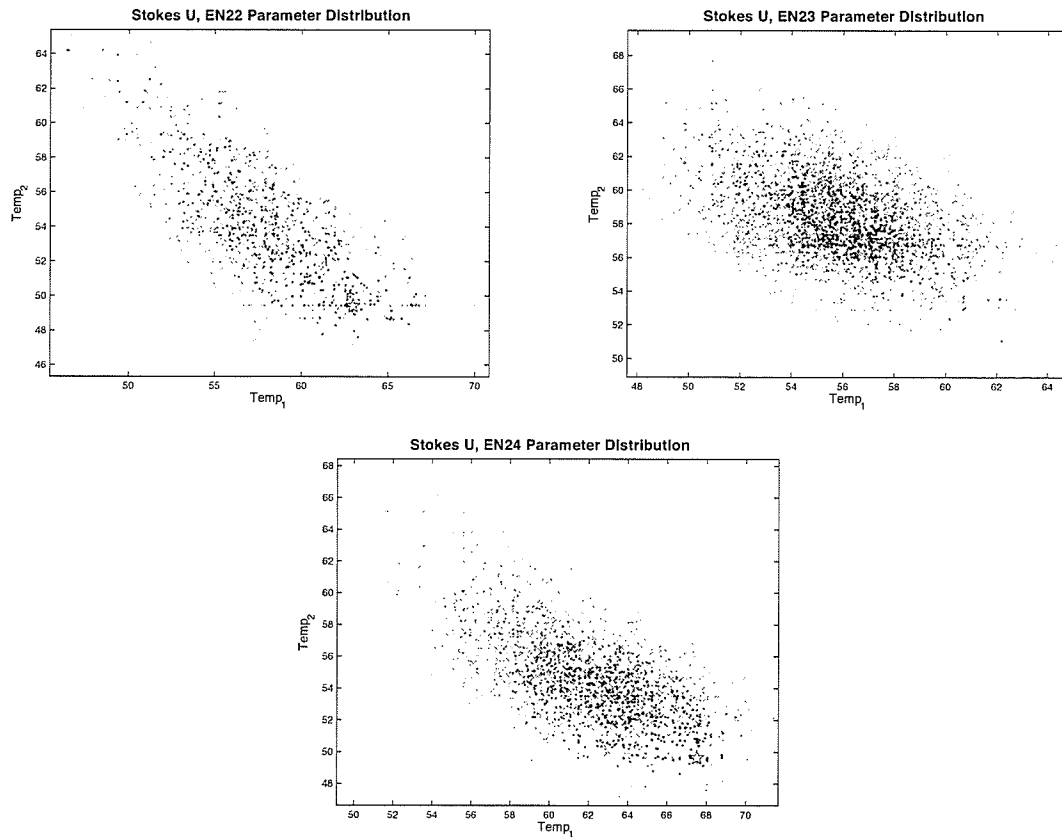


Figure 3.41: Family of solutions EN22-EN24, Stokes U.

3.7 Ferret Solution Surfaces: Stokes U

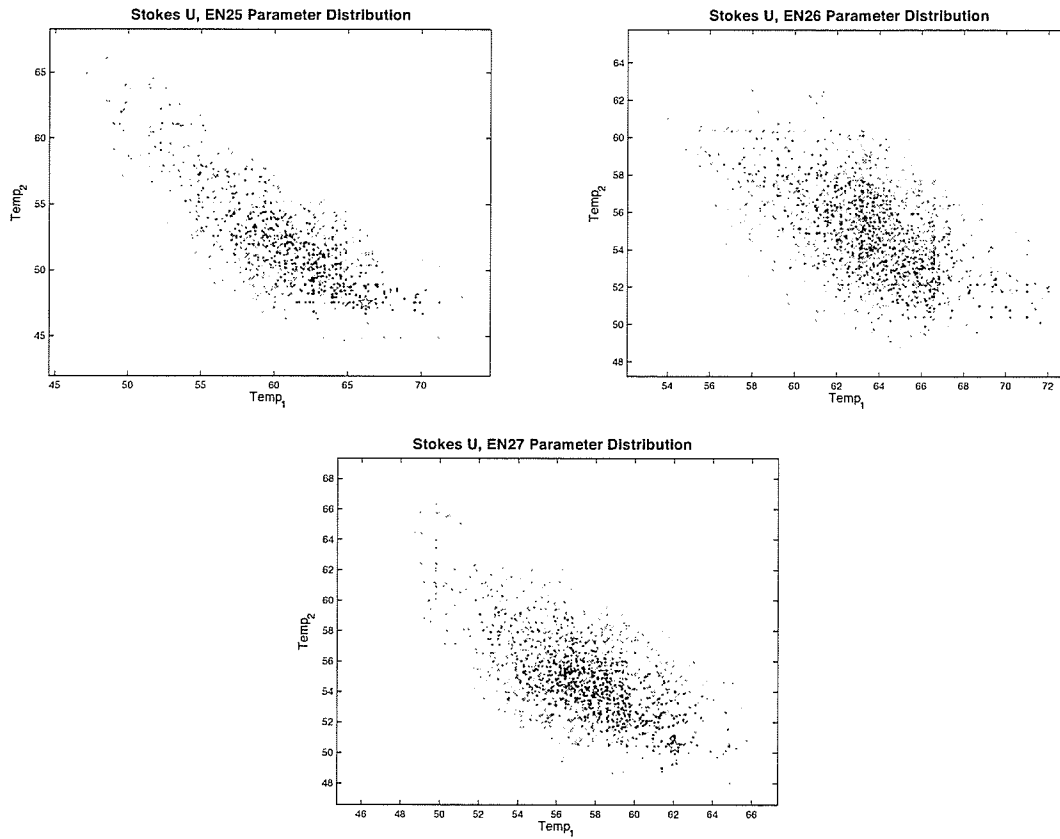


Figure 3.42: Family of solutions EN25-EN27, Stokes U.

3. RESULTS

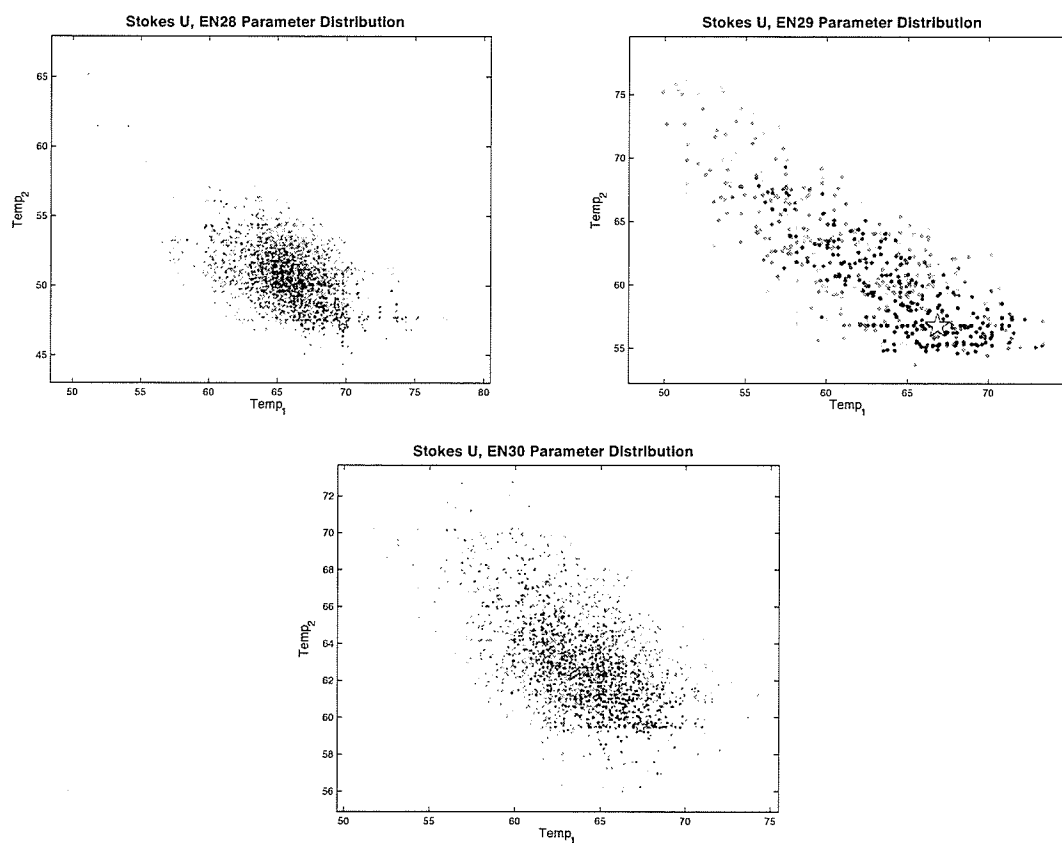


Figure 3.43: Family of solutions EN28-EN30, Stokes U.

3.8 Model Fitness Plots: Stokes Q

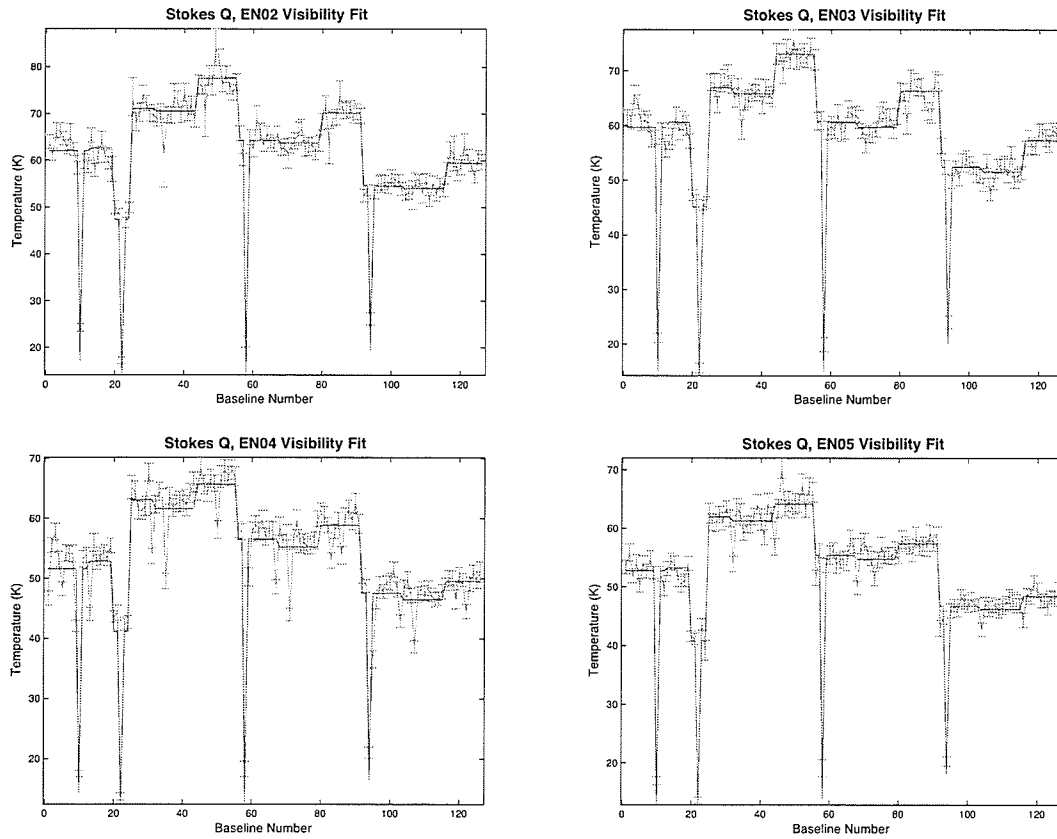


Figure 3.44: Visibility fitness plot EN02-EN05, Stokes Q. The plot shows the final result of the model (blue) fitting data (red).

3. RESULTS

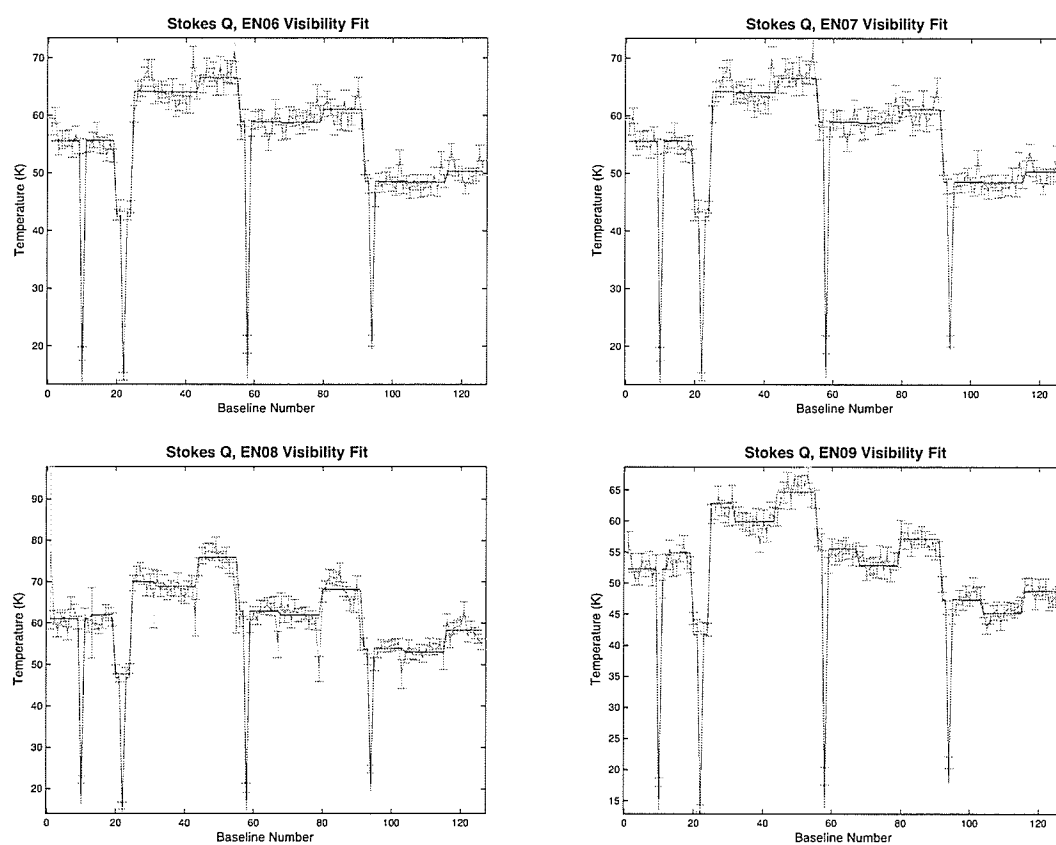


Figure 3.45: Visibility fitness plot EN06-EN09, Stokes Q.

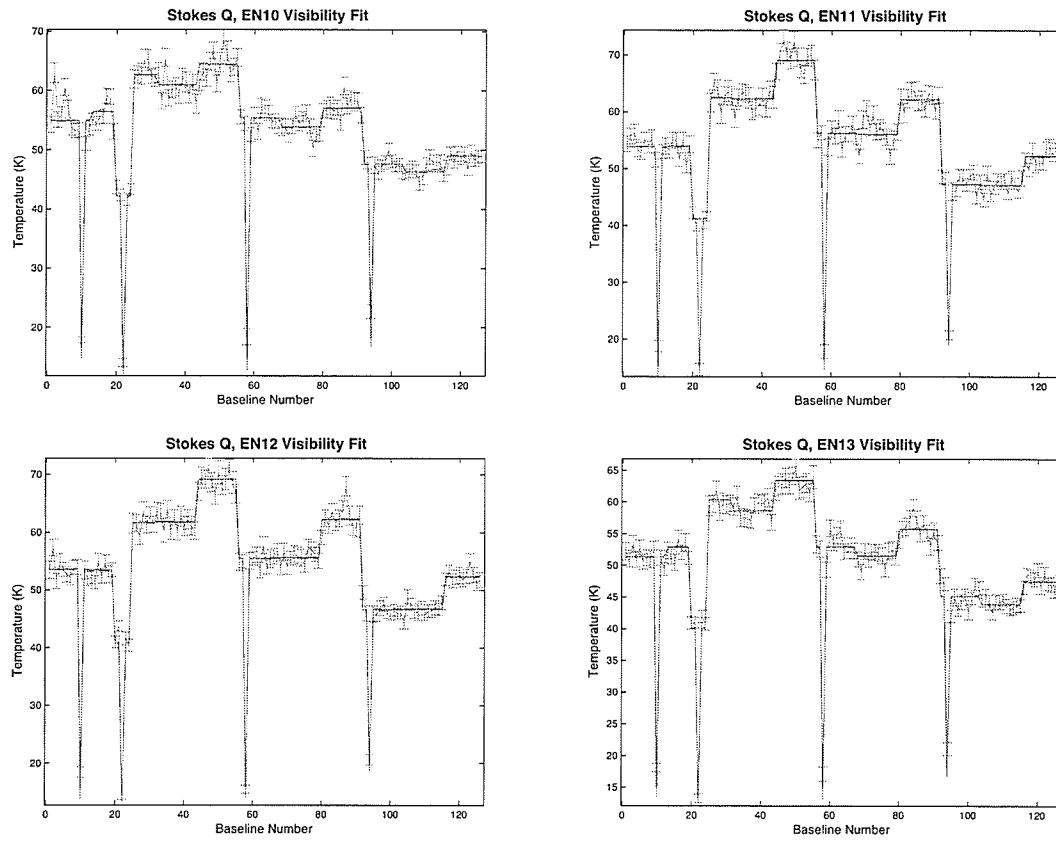


Figure 3.46: Visibility fitness plot EN10-EN13, Stokes Q.

3. RESULTS

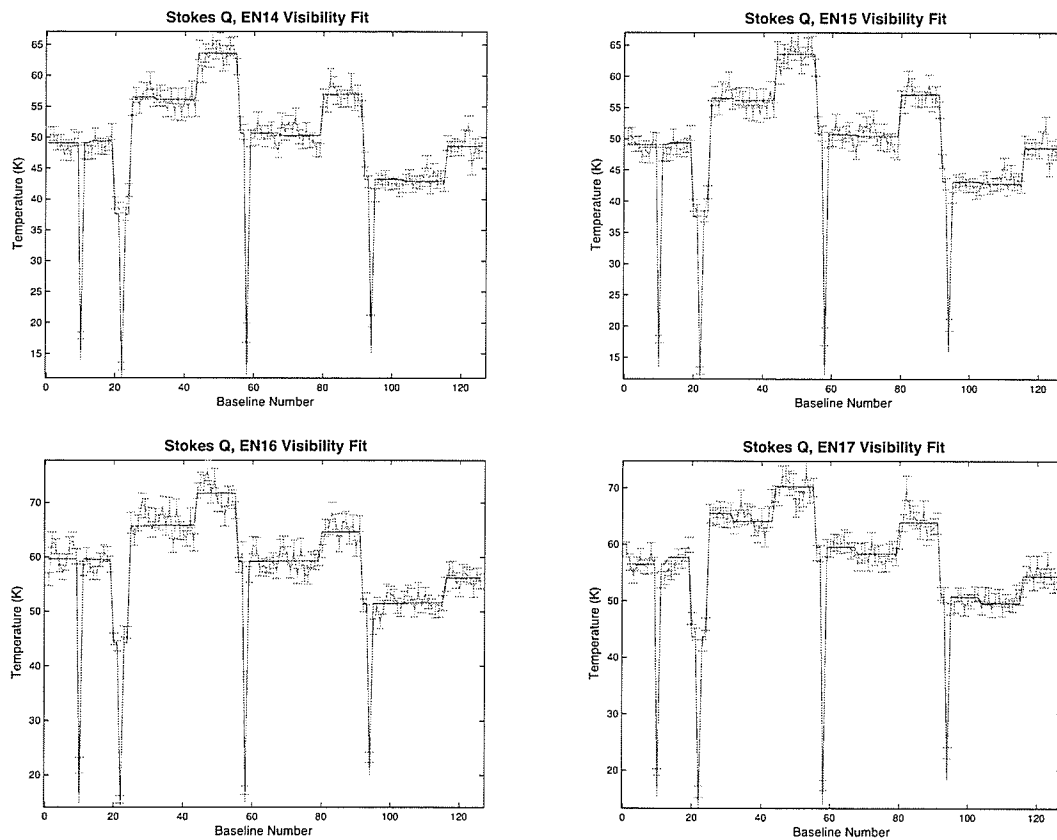


Figure 3.47: Visibility fitness plot EN14-EN17, Stokes Q.

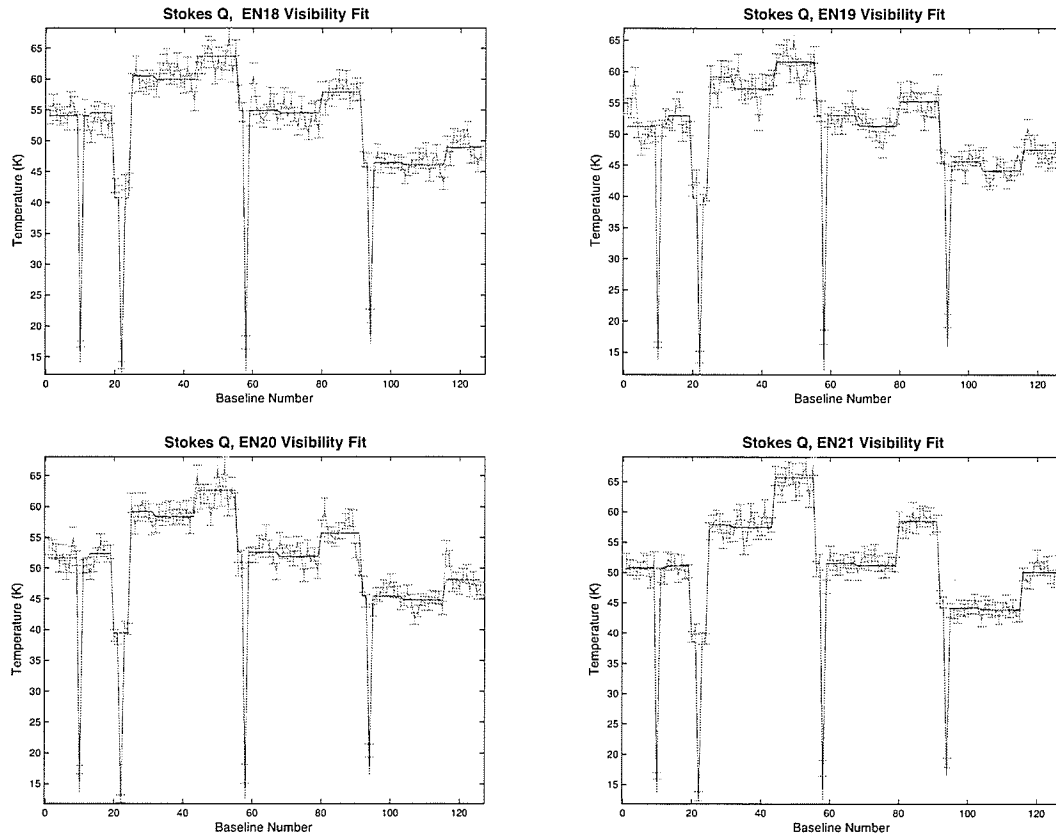


Figure 3.48: Visibility fitness plot EN18-EN21, Stokes Q.

3. RESULTS

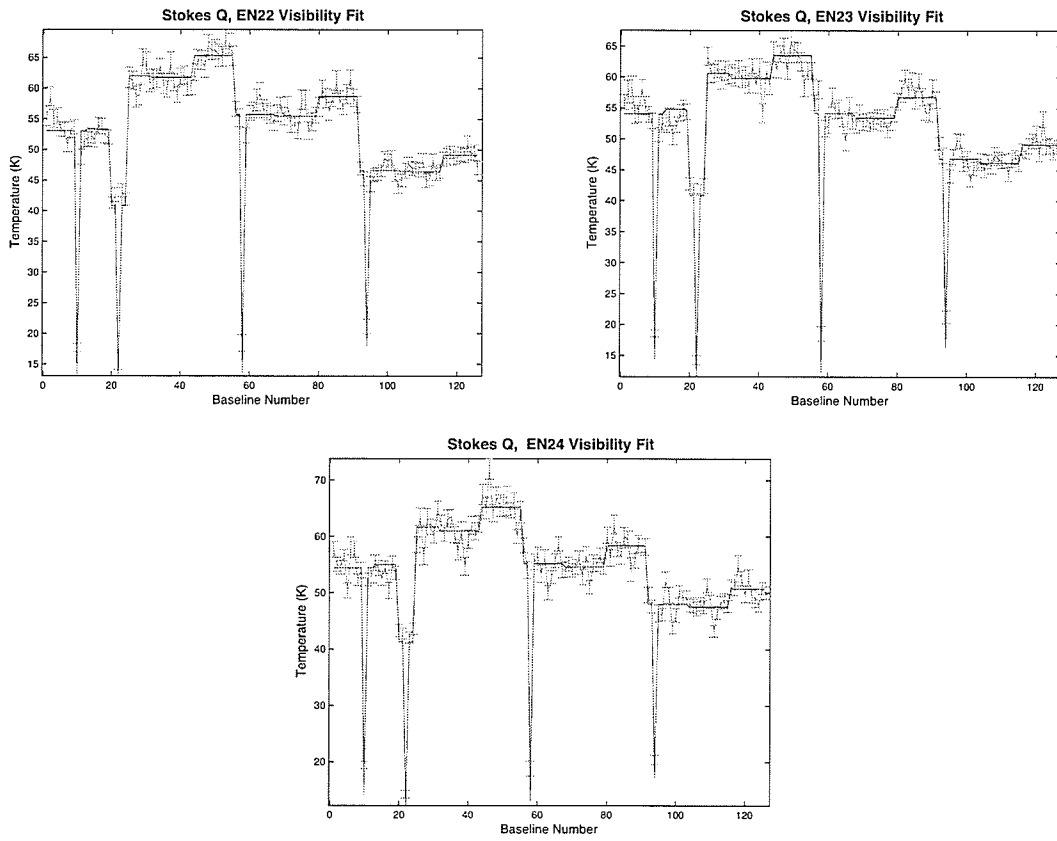


Figure 3.49: Visibility fitness plot EN22-EN24, Stokes Q.

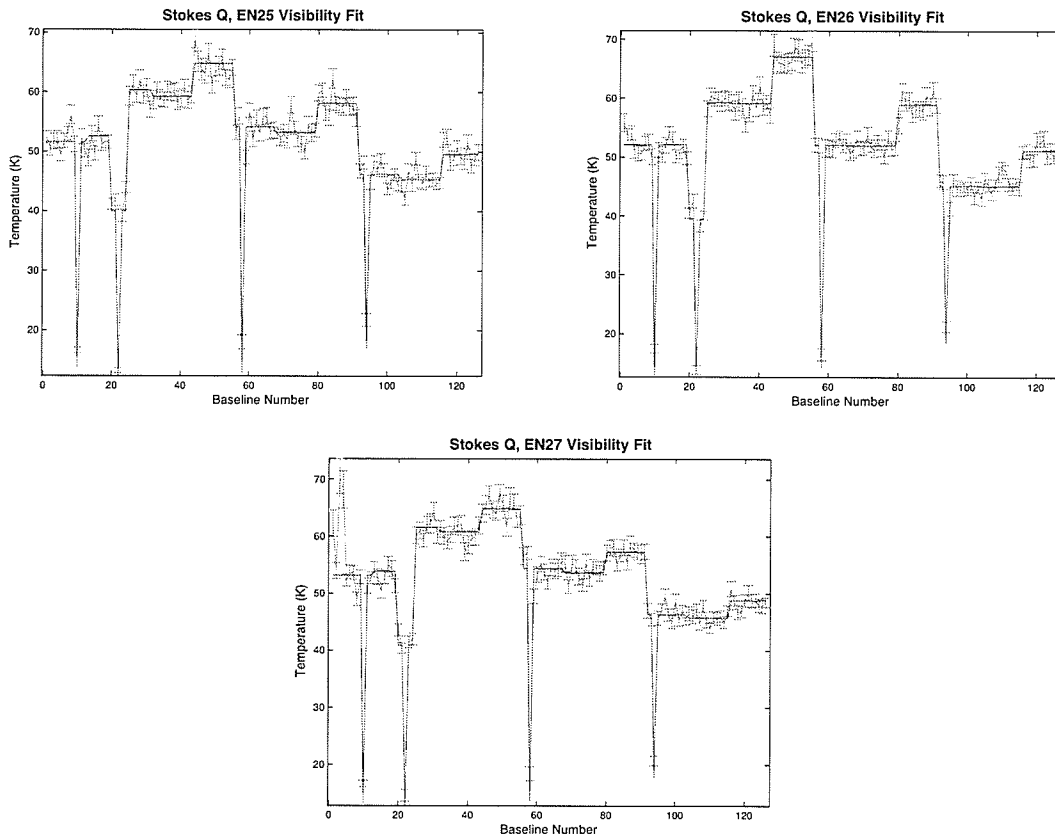


Figure 3.50: Visibility fitness plot EN25-EN27, Stokes Q.

3. RESULTS

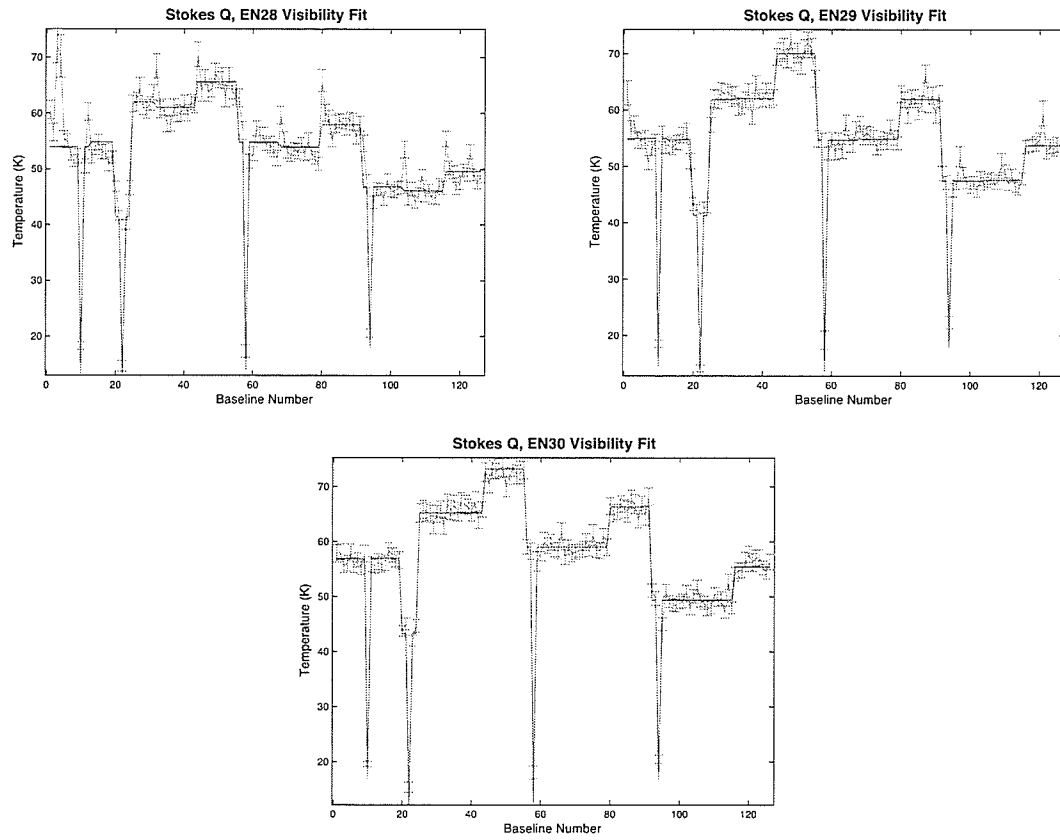


Figure 3.51: Visibility fitness plot EN28-EN30, Stokes Q.

3.9 Model Fitness Plots: Stokes U

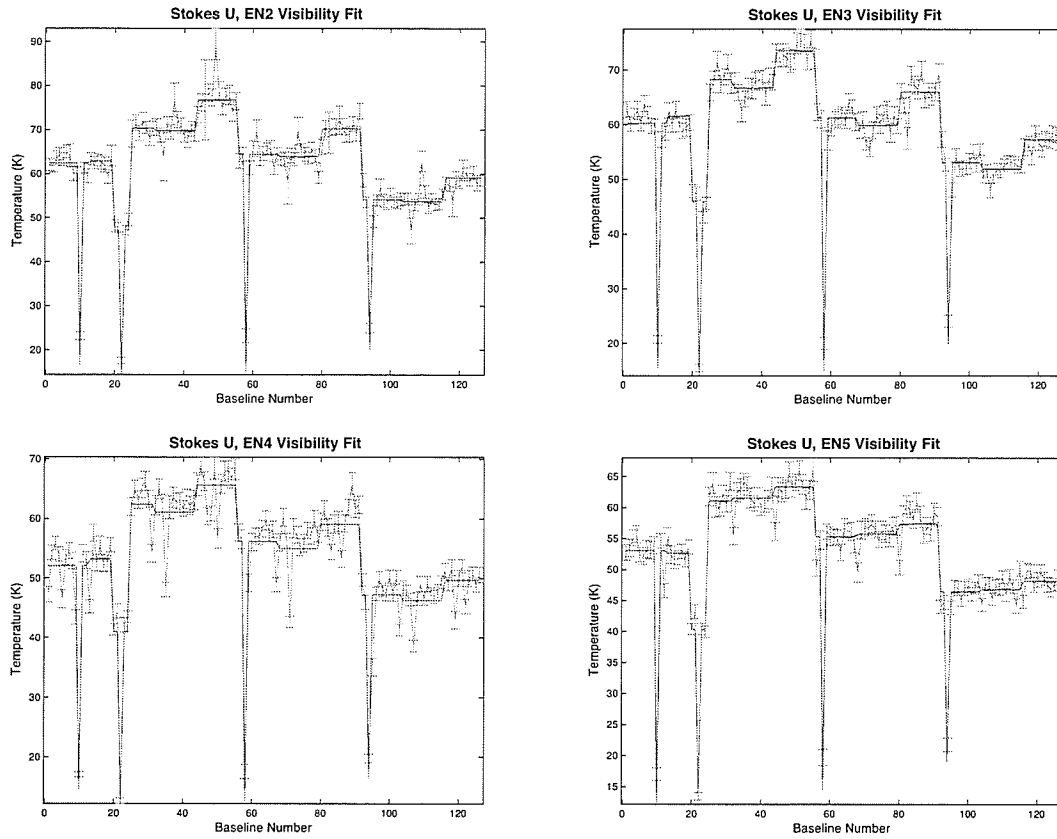


Figure 3.52: Visibility fitness plot EN02-EN05, Stokes U.

3. RESULTS

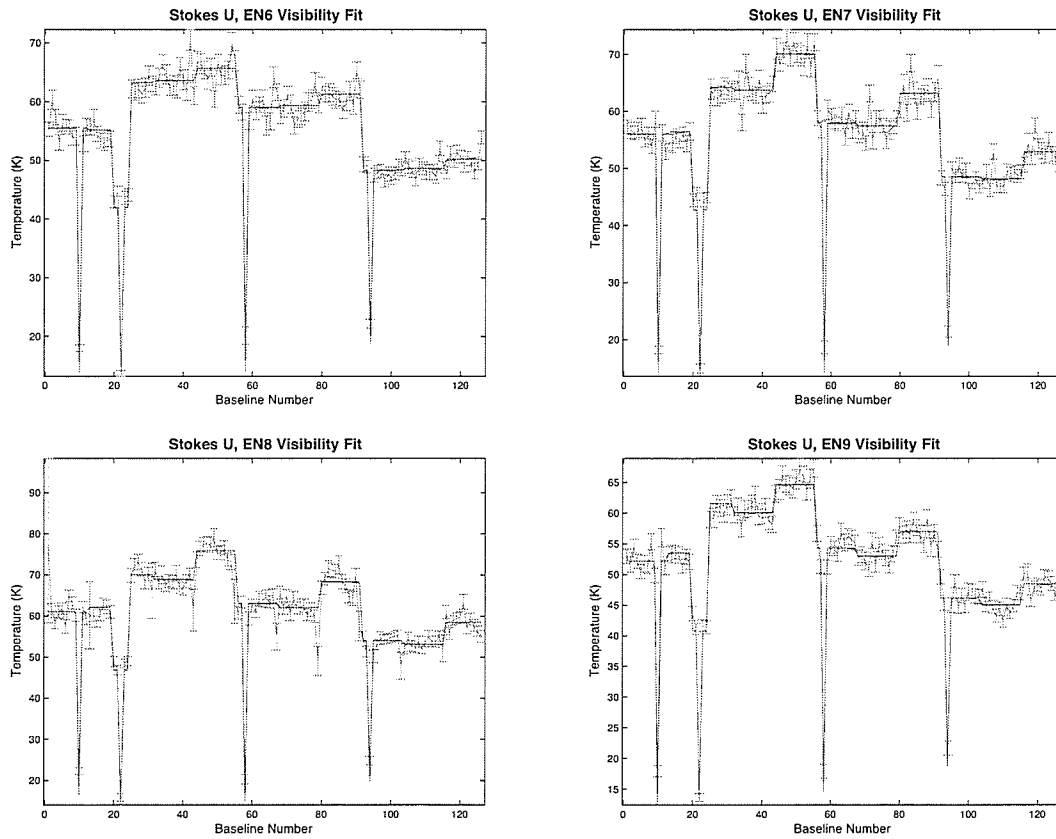


Figure 3.53: Visibility fitness plot EN06-EN09, Stokes U.

3.9 Model Fitness Plots: Stokes U

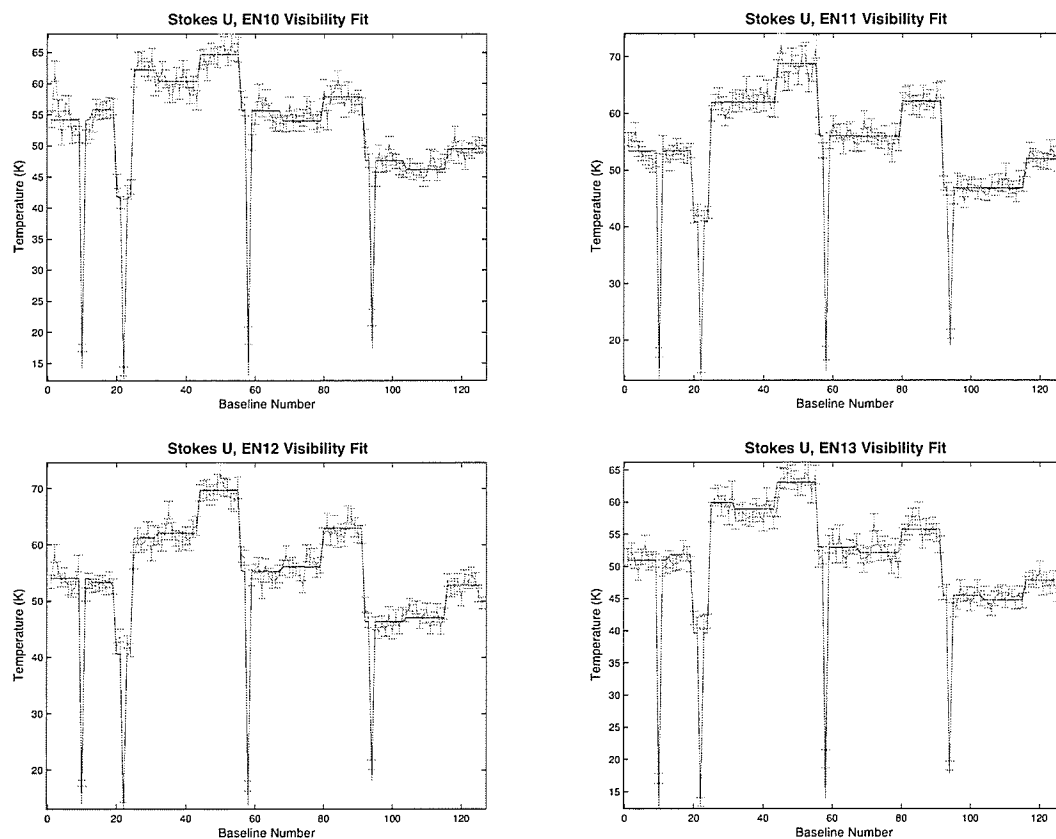


Figure 3.54: Visibility fitness plot EN10-EN13, Stokes U.

3. RESULTS

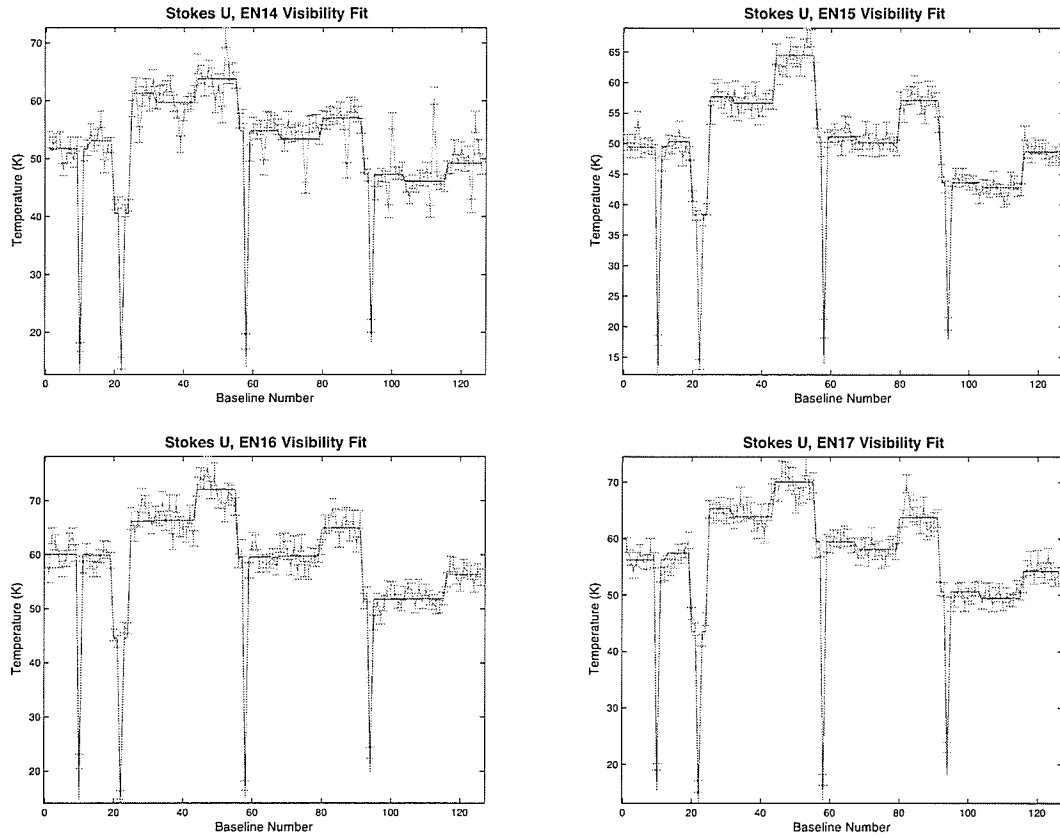


Figure 3.55: Visibility fitness plot EN14-EN17, Stokes U.

3.9 Model Fitness Plots: Stokes U

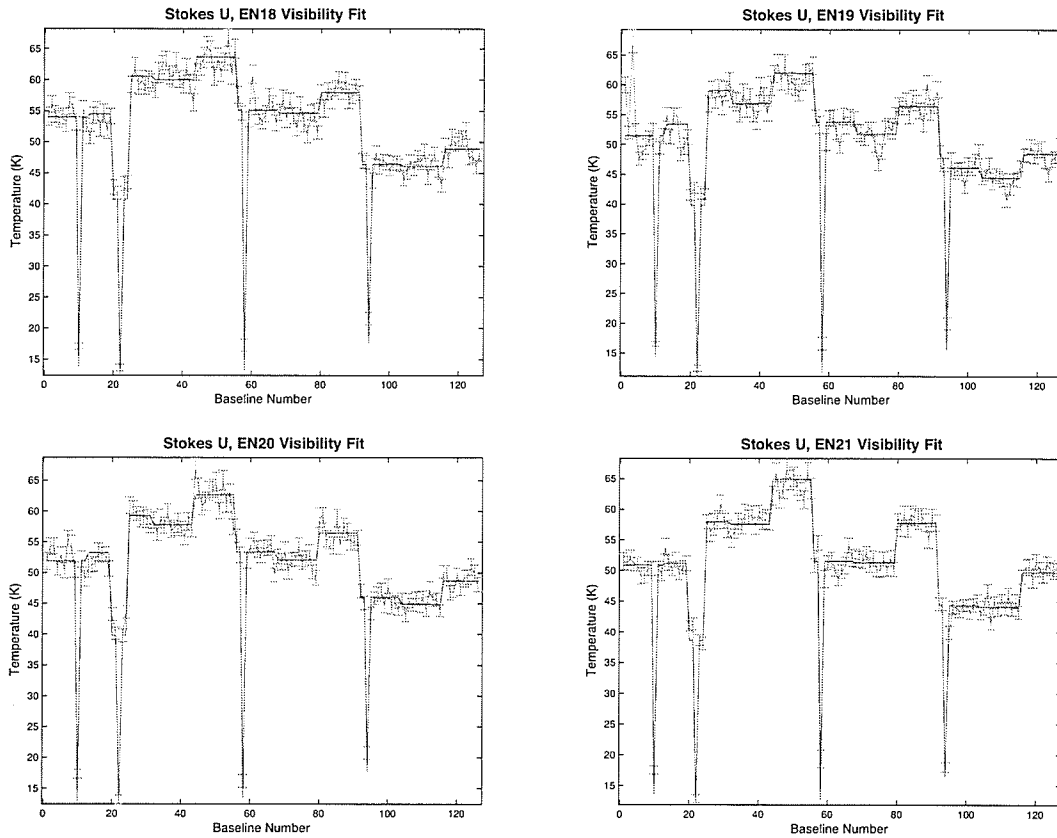


Figure 3.56: Visibility fitness plot EN18-EN21, Stokes U.

3. RESULTS

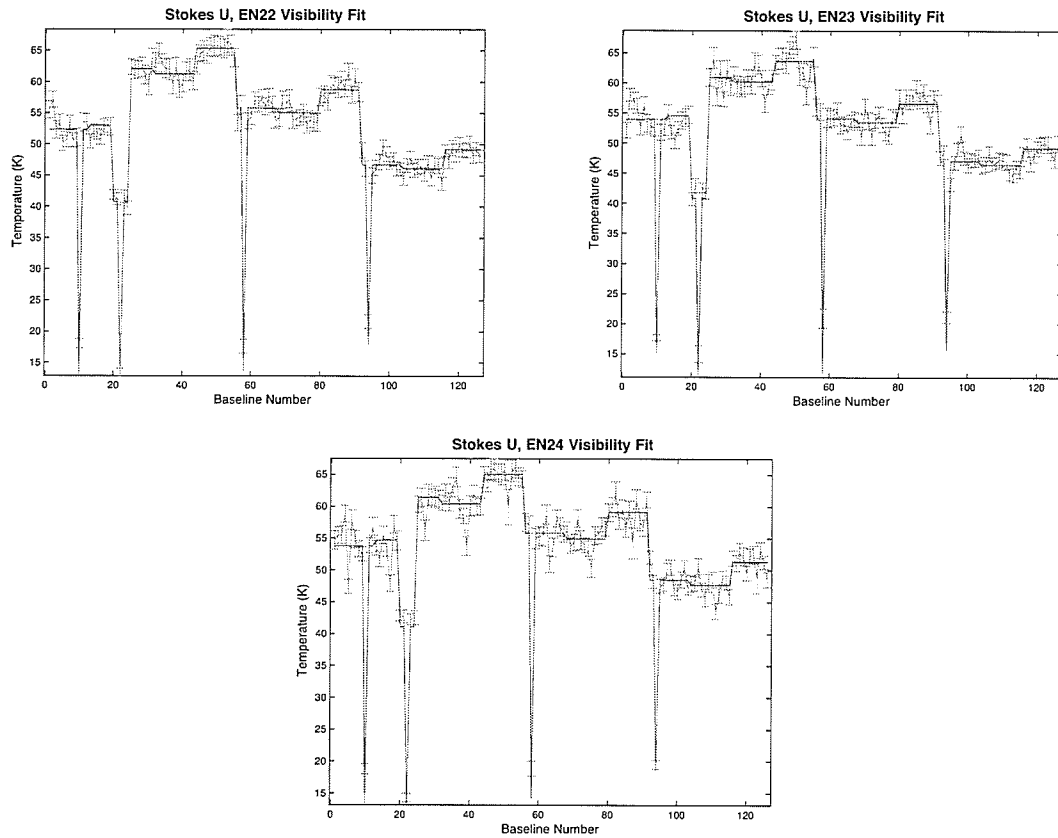


Figure 3.57: Visibility fitness plot EN22-EN24, Stokes U.

3.9 Model Fitness Plots: Stokes U

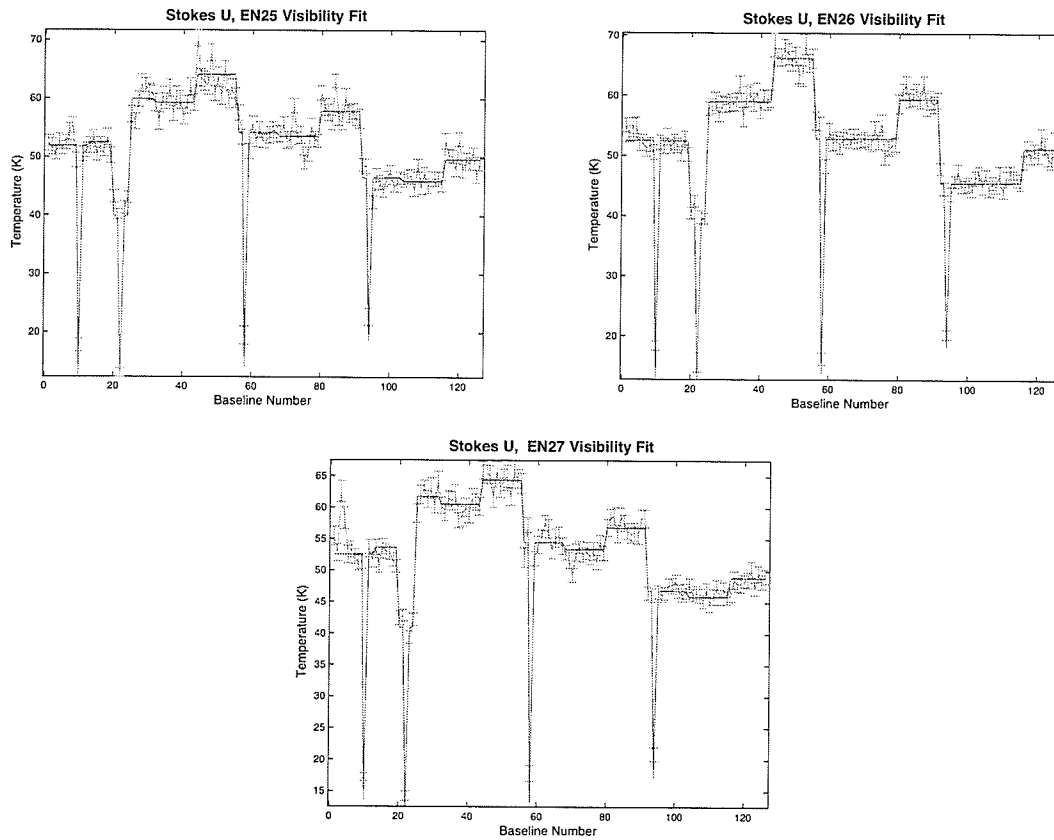


Figure 3.58: Visibility fitness plot EN25-EN27, Stokes U.

3. RESULTS

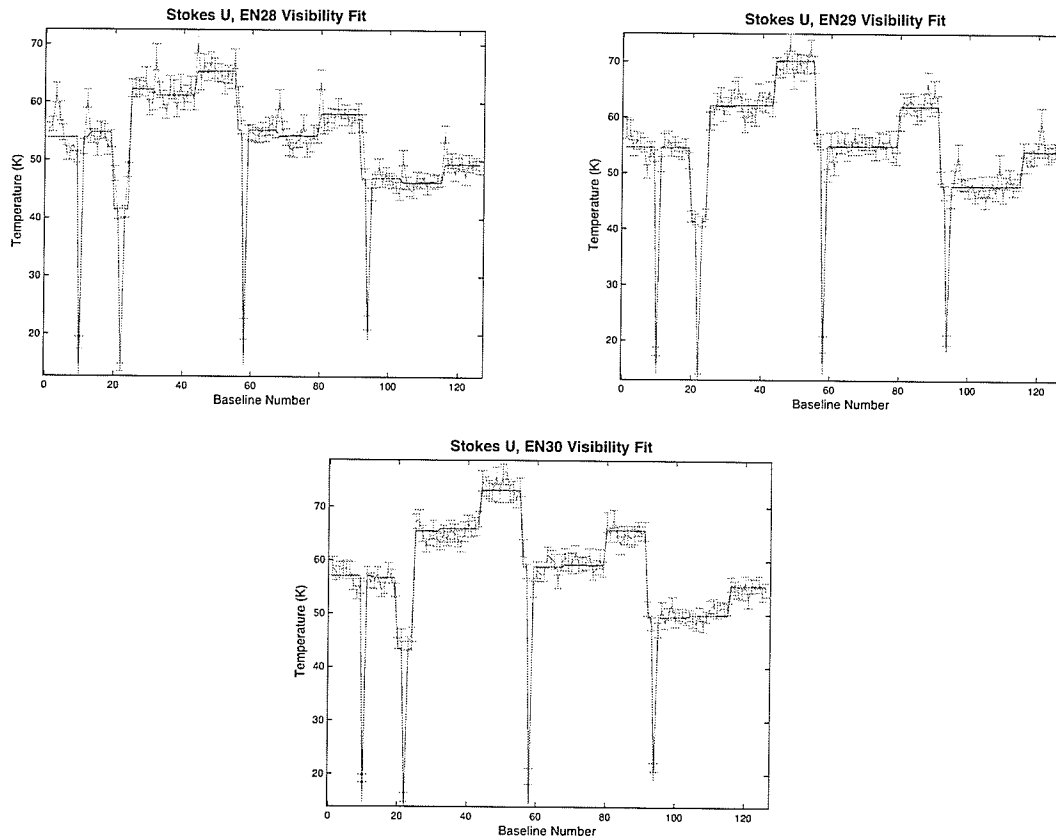


Figure 3.59: Visibility fit plot EN28-EN30, Stokes U.

4

Discussion

4.1 CMB Foregrounds in ELAIS-N1

From figures 3.4, 3.5, 3.9 and 3.10, which show power spectra from both the synthesized data and the real ELAIS-N1 data, we can conclude that significant polarized emission has been detected in all baselines in the ELAIS-N1 field. This is true for both the spectra from the individual fields, and from the mosaics. By producing these spectra we can see that the Galactic emission appears to be 2 to 3 times higher intensity than the noise, depending on the baseline. The process of mosaicing has reduced the noise level significantly in both images, and thus reduced the difference in the noise levels as well. However despite the small difference in magnitude, it is obvious where there is signal present.

Common to the power spectra of the individual fields (section 3.4 and 3.5) and of the mosaic (fig 3.4, 3.5, 3.9 and 3.10), is the presence of a large noise peak at short spacings. The possible causes for this peak have been discussed in Chapter 2. While the mosaic has reduced the peak significantly it is still obviously larger than any other signal in the spectrum. This is a difficult area to analyze, because hidden in the high level of spurious signal, are the broadest structures we would like to observe. The spectra also show that a large amount of the signal is being detected at approximately 300 meters, suggesting a characteristic size of 2 arcminutes.

Now that it has been established that there is an extended structure in the this area of the Galactic foreground two questions arise, the first, ‘what is this emission in the field?’ and the second, ‘how can this be distinguished from the CMB?’. The fact that this emission disperses itself throughout an image makes it difficult to analyze in the image plane, however, looking at it in the visibility plane proves to be an efficient method for classifying the emission. Aperture synthesis gives us an idea of the structure of the emission we are looking at.

4. DISCUSSION

4.1.1 Confidence in Results

The sensitivity of these measurements, and the consequence of their analysis means that we need to have a good handle on the accuracy of our measurements. CMB polarization is extremely sensitive to small perturbations and we need to be sure that the system temperature measurements come with reasonable errors that will not affect the results of Planck. Considering the results presented in chapter 3, we can demonstrate our errors by considering both the chi-squared values presented in tables 3.1 and 3.2 (which are supported by the fitness plots in sections 3.8 and 3.9) and the solution surfaces which are presented in sections 3.6 and 3.7.

First, considering the chi-squared values, there is a visible and quantifiable correlation between chi-squared and quality of data. For example, ELAIS-N1 fields which have the highest chi-squared are EN04, EN14. Looking at their visibility fits shows that these fields have particularly large errors in the data, which can be verified by the magnitude of their errors. Despite the fitness of the model to the data appearing near-perfect, these large uncertainties in the data mean a less reliable temperature derivation. Though, if we look at the difference in temperature values between EN04, and EN14 with a field with a chi-squared closer to one, we see very little variation in temperature. There is rarely a difference of more than 1.5K.

The family of solutions in section 3.6 and 3.7 show a sampling of possible solutions that exist within the specified tolerance. This feature in Ferret maps out a range of possible solutions. The figures show (for the first two parameters, system temperatures for antenna 1 and antenna 2) a range of solutions where most of them lie within 5K of each other, with the exception of very few outliers. This compact surface suggests a high level of precision for our temperature values, especially given the consistency across all fields and polarizations.

Also, in considering errors, recall that in order to optimize system temperature determination, noise peaks at short spacings were removed. Because it is somewhat uncertain where this phenomenon comes from, it is difficult to assess how far this peak might travel down the visibility plane. In an effort to quantify how this removal may be affecting the system temperature results baselines were removed one by one and the temperatures were derived after each removal. Figure 4.1, is a plot showing by how much each antenna (T1-T7) is affected by each baseline removal up to 43. We see large dips in temperature when we approach an area where a particular baseline ends. That is, for example, when all the baselines containing T1, T2 and T3 are removed, we see a drop in their temperature because they are contributing less to the complete spectrum of data. For the results presented, baselines were not removed up to or beyond the first major dip in the results, which occurs after removing ten baselines. For this experiment only 8 baselines have been removed, which suggests, given the plot, an adequately

stable data set. However, the fact that T1, T2, and T3 vary so much across this plot, suggest that they are large contributors to the data, and thus are highly sensitive to baseline removal.

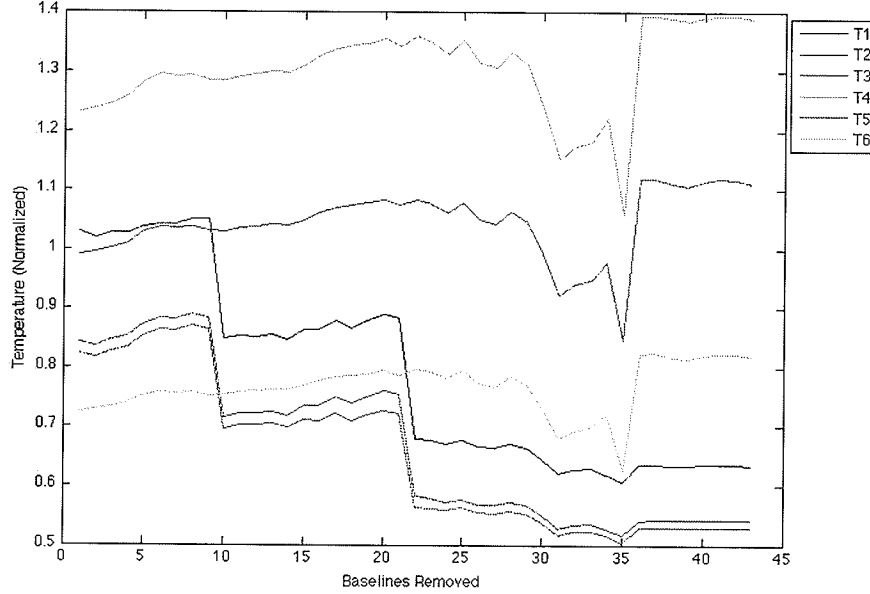


Figure 4.1: Removing baselines - Removing baselines and optimizing system temperature changes the values as removals get farther down the telescope line. The figure shows how the temperature values change throughout that process. We see large variations, particularly at value ten which corresponds to baseline 12, because this highly redundant baseline is removed. The antenna temperatures here have been normalized to T7.

Another demonstration of confidence in our methods is table 4.1. This table shows the variation in system temperature from one run to another. As shown, the variation in both temperature and χ^2 are minimal, meaning that Ferret is consistent between trials and it is not expected that optimization errors have occurred.

4.2 Versatility of Software and Future Work

The result of this project and the methods described in the previous chapters have shown that a method has been developed that can accurately measure the system temperature of the DRAO synthesis telescope. Knowing system temperatures is a common endeavour of astronomers and engineers as it provides them with both information on how efficient a telescope is and tells them the accuracy of the data it collects. This result of this method is not only useful for

4. DISCUSSION

Field Name	Antenna Temperatures (K)	Chi-squared
EN02 trial 1	71.39, 65.36, 53.87, 55.11, 92.26, 75.39, 54.16	3.09
EN02 trial 2	71.37, 65.49, 54.03, 55.29, 92.06, 75.11, 54.21	2.94
EN02 trial 3	73.65, 63.32, 52.28, 53.43, 95.21, 77.51, 55.79	3.02
EN02 trial 4	75.57, 60.05, 49.68, 50.56, 99.83, 81.80, 58.79	2.74
EN02 trial 5	76.41, 61.78, 50.91, 52.00, 97.95, 80.11, 57.58	2.98
EN03 trial 1	70.03, 62.91, 50.93, 52.65, 85.00, 70.17, 52.18	2.48
EN03 trial 2	68.24, 64.11, 51.84, 53.69, 83.50, 68.98, 51.46	2.73
EN03 trial 3	71.27, 61.52, 49.82, 51.52, 86.89, 71.60, 53.40	2.64
EN03 trial 4	73.50, 59.32, 47.97, 49.69, 89.85, 74.11, 55.05	2.61
EN03 trial 5	73.91, 59.39, 48.20, 49.79, 89.98, 74.08, 55.21	2.51
EN04 trial 1	57.40, 53.24, 46.64, 48.58, 80.79, 65.29, 46.35	8.94
EN04 trial 2	61.16, 49.87, 43.96, 45.81, 85.87, 69.71, 49.26	8.53
EN04 trial 3	58.92, 50.78, 44.99, 46.52, 84.23, 68.19, 48.18	8.73
EN04 trial 4	55.79, 55.76, 48.72, 51.00, 77.38, 63.10, 44.40	8.30
EN04 trial 5	56.68, 53.40, 47.02, 49.29, 80.76, 64.97, 45.98	8.54
EN05 trial 1	65.97, 46.19, 42.25, 42.86, 88.78, 71.02, 50.74	2.62
EN05 trial 2	67.31, 45.49, 41.44, 42.20, 89.99, 72.57, 51.66	2.78
EN05 trial 3	65.99, 46.47, 42.43, 42.90, 88.86, 70.85, 50.69	2.57
EN05 trial 4	65.98, 46.74, 42.89, 43.42, 89.25, 71.42, 50.76	2.48
EN05 trial 5	64.18, 47.49, 43.33, 44.23, 86.57, 69.25, 49.41	2.69
EN06 trial 1	70.75, 46.87, 43.56, 43.65, 94.38, 79.31, 53.93	1.94
EN06 trial 2	69.76, 47.39, 43.96, 44.07, 92.99, 77.92, 52.65	1.94
EN06 trial 3	70.68, 46.84, 43.37, 43.56, 94.70, 79.11, 53.84	2.01
EN06 trial 4	69.62, 47.53, 43.99, 44.08, 93.28, 78.28, 53.09	1.91
EN06 trial 5	67.63, 49.21, 45.62, 45.78, 89.01, 75.78, 51.43	1.90

Table 4.1: Temperature and fitness values obtained by using the Ferret genetic algorithm for 5 trials of each of 5 fields. The results demonstrate consistency in the fitting method. Results show are for Stokes Q.

determining the accuracy of data collected by the DRAO synthesis telescope, but it also has applications to other telescopes and projects.

4.2.1 Other Synthesis Telescopes

The basis of this software is a fairly simple equation, 2.2, which relates the variance of antenna pairs. In the immediate example we are dealing with a seven-element linear array, which is also geometrically uncomplicated. Despite being developed for the purpose of evaluating this particular problem, the software can easily be extended to more complex situations. Most synthesis telescopes are unique and possess different geometries and number of antennas.

For example, the addition of more telescopes to the linear array can be accomplished by simply increasing the number of parameters sent to Ferret. This would allow us to apply the code to other linear arrays. Changing the geometry of the telescope to something like a VLA-style Y-shaped pattern or a log spiral, could easily be accomplished, but the change would mean more variability per telescope (as there would be a larger number of redundant baselines in the visibility plane) and could increase the run time. Regardless, the ability to make these changes means that the noise temperature determination method could be applied to any synthesis telescope, making it a very useful tool for radio astronomy.

4.2.2 DRAO Data

In addition to the ELAIS-N1 deep field, DRAO carried out another deep field survey, the Spider deep field (named after the appearance of an infrared feature of the field). Our software can easily be applied to the Planck field visibility data to compare noise properties to diffuse emission. The parameters of the problem are identical so this task may be carried out as future work, as both of the deep fields contain information useful to cosmologists.

4.2.3 Square Kilometer Array

The noise properties of an interferometer are highly dependent on its components. This means that any change in the electronics of the telescope would manifest itself in the noise. Thanks to this property, the software can now be used to accurately measure differences in noise contribution of low noise amplifiers inexpensively and accurately. Because DRAO is now being used as a test bed for Square Kilometer Array technology, the techniques used in this project could be directly applicable to the future of radio astronomy.

4.3 Conclusions and Summary

We have emerged from this research having developed a new method for characterizing the system noise in a synthesis telescope, in particular, the DRAO interferometer. This method, uses a model interferometer and fits its visibility output to visibility data from the ELAIS-N1 deep field survey, using the Ferret genetic algorithm. The robustness of genetic algorithms and sophistication of Ferret have provided particularly accurate results (as represented by the chi-squared of the fit) and a good grasp on the accuracy to which we know these temperatures, as is shown by the solution surfaces.

Though it was developed for the purpose of aiding cosmologists in improving the accuracy of CMB measurements, the software is also extremely versatile and can be beneficial to other areas of radio astronomy. It can be easily modified to include different geometries, so although this project focused on a linear array, it would be easy to use this method on an array such as the Very Large Array (VLA) or upcoming configurations such as the Australian Square Kilometer Array Pathfinder (ASKAP), allowing system temperature measurements for these instruments.

At the forefront of this research is its benefit to cosmologists and in particular those using and obtaining data with the Planck CMB satellite. The system temperatures that were derived were used to create images of the noise they produce on the sky, and were used to show that in the ELAIS-N1 field, there is a diffuse signal which can be detected slightly above the range of system noise. The knowledge of this diffuse emission will allow those using the Planck data to assess their polarization measurements in relation to the foreground in hopes of producing a sufficiently accurate map of the CMB to obtain knowledge of the early universe that was not previously accessible.

References

- [1] THE PLANCK COLLABORATION. **The Scientific Programme of Planck.** *astro-ph/0604069*, 2006. 1, 3
- [2] D BAUMAN. ET AL. **Probing Inflation with CMB Polarization.** *American Institute of Physics Conference Series, 1141, 10-120*, 2000. 1, 2, 3
- [3] J FIEGE. **Qubist User Guide.** *Pre-publication*, 2009. 1, 15, 39, 41
- [4] J BOCK ET AL. **Task Force on Cosmic Microwave Background Research.** *astro-ph/0604101*, 2006. 2
- [5] ROBERT CALDWELL AND MARC KAMIONKOWSKI. **Echoes From the Big Bang.** *Scientific American, The Cosmic Life Cycle: Origins of the Universe Reprint*, 2009. 2
- [6] LONSDALE ET AL. **SWIRE: The SIRTf Wide-Area Infrared Extragalactic Survey.** *PASP, 115, 897-927*, 2003. 4
- [7] NATIONAL RESEARCH COUNCIL OF CANADA. **Herzberg Institute of Astrophysics.** *www.nrc-cnrc.gc.ca*, 2009. 4
- [8] K ROHLFS AND T. L WILSON. **Tools of Radio Astronomy.** *Astronomy and Astrophysics Library, Springer-Verlag Berlin Heidelberg New York*, 1996. 5, 11
- [9] T. L. LANDECKER ET AL. **The synthesis telescope at the Dominion Radio Astrophysical Observatory.** *AASP., 145, 509524*, 2000. 6, 7
- [10] DAVID E. GOLDBERG. **Genetic Algorithms in Search, Optimization, and Machine Learning.** *Addison-Wesley*, 1989. 13
- [11] ANDREW GRAY. **srtavg.** *Private Communication and Unpublished Code*, 2007. 16
- [12] WILLIAM H. PRESS. **Numerical Recipes: The Art of Scientific Computing.** *Cambridge University Press*, 2007. 18

REFERENCES

- [13] A.R. TAYLOR ET AL. **The Canadian Galactic Plane Survey.** *AJ.*, 125, 3145-3164, 2003. 19
- [14] DAMIAN EADS. **mfitsio MATLAB package.** *<http://public.lanl.gov/eads/mfitsio>*, 2006. 19
- [15] X HU. **Particle Swarm Optimization.** *swarmintelligence.org*, 2006. 39

5

Appendix

5.1 System Temperature Derivation Code

```
function extPar=init_TotalField(FieldNumber)

BandA=['ENUA', num2str(FieldNumber)];
BandB=['ENUB', num2str(FieldNumber)];
AllBands=['ENU', num2str(FieldNumber)];

%---Loading all required data files for a batch run
%---of 30 fields
extPar.file.A=[BandA,'.dat'];
extPar.file.B=[BandB,'.dat'];
extPar.file.imgA=[BandA,'.fits'];
extPar.file.imgB=[BandB,'.fits'];
extPar.file.imgAll=[AllBands,'.fits'];
extPar.PlotSave=['Spectra_EN_U',num2str(FieldNumber)];
extPar.PlotTitle=...
['Power Spectra Noise (blue) Vs. Signal (red), Stokes U, EN',num2str(FieldNumber)];
extPar.FitsName=['expENU',num2str(FieldNumber),'_fits'];
extPar.TempName=['Temperatures_ENU',num2str(FieldNumber),'_mat'];
extPar.ImageName=['Image_ENU',num2str(FieldNumber),'_mat'];
extPar.Min=['Min',num2str(FieldNumber),'_mat'];
%
extPar.K=DRAO_constants;
extPar=calcVisData(extPar);
```

5. APPENDIX

```
%-----  
  
function K=DRAO_constants  
  
%---All constants relevant to the synthesis  
%---telescope and ELAIS-N1 field  
K.minaxis=59;  
K.majaxis=73;  
K.lambda=.21;  
K.Jy_per_beam_to_K=1.3597834E7*K.lambda^2/K.majaxis/K.minaxis;  
K.ant=1:7;  
K.base=5:144;  
K.NBase=length(K.base);  
K.NAnt=length(K.ant);  
K.NVis=480;  
K.startBaseline=12;  
K.lastBaseline=140;  
K.emptybasedata=127:128;  
K.lambda=0.21;  
K.degree=pi/180;  
K.arcmin=K.degree/60;  
K.longestBaseline=617.18;  
K.beam.a=K.arcmin;  
K.beam.b=K.arcmin;  
K.pixPerBeam=3;  
K.radPerPix=K.beam.a/K.pixPerBeam;  
K.increment=4.286;  
K.baseline=K.increment*K.base;  
K.dec=55*pi/180;  
K.decspectra=pi/180;  
K.gauss_taper=false;  
K.NPix=1024;  
K.ang=linspace(0,pi/2,10000);  
K.NStack=10;  
K.dtheta=K.arcmin/K.pixPerBeam;  
K.dx=K.lambda/K.NPix/K.dtheta; % ~4.286; %Size of a UV plane pixel in m.  
K.dU=K.dx/K.lambda;
```

5.1 System Temperature Derivation Code

```
K.dV=K.dU;
K.NumberSample=100;

if mod(K.NPix,2)
    K.NPix=K.NPix+1;
end

g=zeros(K.NAnt,K.NAnt,K.NBase);

% ;The list of antennas used for each baseline
%(without including the redundancies):
% ; Baselines:                Interferometer:
% ; 3 to 14                    1 x 2
% ; 15 to 26                   1 x 3
% ; 27 to 38                   1 x 4
% ; 39 to 45                   5 x 4
% ; 46 to 57                   5 x 3
% ; 58 to 69                   5 x 2
% ; 70 to 81                   6 x 4
% ; 82 to 93                   6 x 3
% ; 94 to 105                  6 x 2
% ; 106 to 117                 7 x 4
% ; 118 to 129                 7 x 3
% ; 130 to 141                 7 x 2

% ; 144                        7 x 1

g(1,2,3:14)=1;
g(1,3,15:26)=1;
g(1,4,27:38)=1;
g(4,5,39:45)=1;
g(3,5,46:57)=1;
g(2,5,58:69)=1;
g(4,6,70:81)=1;
g(3,6,82:93)=1;
g(2,6,94:105)=1;
g(4,7,106:117)=1;
g(3,7,118:129)=1;
```

5. APPENDIX

g(2,7,130:141)=1;

g(1,7,144)=1;

% ; Baseline (*4.286m):	# of observations and antennas	total # times observed
% ; 12	1(1x2), 12(2x3), 12(3x4)	25
% ; 24	1(1x3), 12(2x4)	13
% ; 34	1(1x4), 1(4x5)	2
% ; 35	1(1x4), 1(4x5)	2
% ; 36	1(1x4), 1(4x5), 12(5x6), 12(6x7)	26
% ; 37	1(1x4), 1(4x5)	2
% ; 38	1(1x4), 1(4x5)	2
% ; 72	1(4x6), 12(5x7), 12(1x5)	25
% ; 108	1(4x7), 12(1x6)	13
% ; 144	12(1x7)	12

% Format: g(ant1,ant2,baseline #)=redundancy

g(1,2,12)=1;

g(2,3,12)=12;

g(3,4,12)=12;

%

g(1,3,24)=1;

g(2,4,24)=12;

%

g(1,4,34)=1;

g(4,5,34)=1;

%

g(1,4,35)=1;

g(4,5,35)=1;

%

g(1,4,36)=1;

g(4,5,36)=1;

g(5,6,36)=12;

g(6,7,36)=12;

%

g(1,4,37)=1;

g(4,5,37)=1;

%

g(1,4,38)=1;

5.1 System Temperature Derivation Code

```
g(4,5,38)=1;
%
g(4,6,72)=1;
g(5,7,72)=12;
g(1,5,72)=12;
%
g(4,7,108)=1;
g(1,6,108)=12;
%
g(1,7,144)=12;
%
% Store g
K.g=g;

%-----
function extPar=calcVisData(extPar)

% Calc variances.
%----Reading binary outputs of visibilities
fid=fopen(extPar.file.A,'r');
fid1=fopen(extPar.file.B,'r');
databandA=fread(fid,'float32')/1000*extPar.K.Jy_per_beam_to_K;
databandB=fread(fid1,'float32')/1000*extPar.K.Jy_per_beam_to_K;
% This is in K - NOT K^2.

%----Removing flagged data points
%----which are large and nagative (-1E38)
databandA(databandA < -1E37)=NaN;
databandB(databandB < -1E37)=NaN;
%----Subtraction of freq bands for noise
response=(databandA)-(databandB)/sqrt(2);
% N=databandA;
N=length(response);
M=length(databandA);
%----Data is sorted in real then complex
response=response(1:2:N-1)+sqrt(-1)*response(2:2:N);
databandA=databandA(1:2:M-1)+sqrt(-1)*databandA(2:2:M);
%----Taking an average over 90 visibilities
```

5. APPENDIX

```
%----(Variance is constant over hour angle)
extPar.baseline=1:extPar.K.lastBaseline;
extPar.sigma=NaN(1,extPar.K.lastBaseline);
extPar.sigmaErr=NaN(1,extPar.K.lastBaseline);
%
baseline.a=(extPar.K.baseline/extPar.K.lambda)/extPar.K.dU;
baseline.b=baseline.a*sin(extPar.K.dec);
NAng=length(extPar.K.ang);
grid.sigma=[];
for q=4:-1:1 % 4 quadrants
    grid.grid.UV_noise_quadrants{q}=zeros(extPar.K.NPix/2);
end
%
for b=extPar.K.lastBaseline:-1:extPar.K.startBaseline;
    j=(b-1)*extPar.K.NVis+1;
    response1=response(j:j+extPar.K.NVis-1);
    response1(isnan(response1))=[];
    extPar.sigma(b)=std(response1); % sqrt(2) higher than std(real(TNoise1)). [K^2]
    NR1=length(response1);
    databandA1=databandA(j:j+extPar.K.NVis-1);
    databandA1(isnan(databandA1))=[];
    extPar.sigma(b)=std(response1); % sqrt(2) higher than std(real(TNoise1)). [K^2]
    NR1=length(response1);
    if ~isempty(response1)
        response1_MC=response1(ceil(NR1*rand(extPar.K.NumberSample, NR1)));
        sigma1=std(response1_MC,0,2);
        extPar.sigmaErr(b)=std(sigma1);
        %
        % Create an image by Monte Carlo'ing the actual distribution in
        % response1.
        ix=1./sqrt(1./baseline.a(b).^2+tan(extPar.K.ang).^2./baseline.b(b).^2);
        iy=ix.*tan(extPar.K.ang);
        i=max(1,ceil(ix));
        j=max(1,ceil(iy));
        for q=4:-1:1
            grid.grid.UV_noise_quadrants{q}(i+extPar.K.NPix/2*j)...
                =response1(ceil(NR1*rand(1, NAng)));
        end
    end
end
```

```

    end
end
grid.UV_noise=[[grid.grid.UV_noise_quadrants{1},...
fliplr(grid.grid.UV_noise_quadrants{2})];...
    flipud([grid.grid.UV_noise_quadrants{3},...
fliplr(grid.grid.UV_noise_quadrants{4})])]];

    img_data=(fitsread(extPar.file.imgA)-fitsread(extPar.file.imgB))...
    *1000*extPar.K.Jy_per_beam_to_K/sqrt(2);
data_std=std(img_data(:));
index=find(grid.UV_noise);
model_std=std(grid.UV_noise(index));
extPar.factor=data_std/model_std;
extPar.sigma=extPar.factor*extPar.sigma;
extPar.TEST=(grid.UV_noise)*extPar.factor;
extPar.sigmaErr=extPar.factor*extPar.sigmaErr;
extPar.sigmaErr(1:extPar.K.startBaseline)=[];
extPar.sigma(1:extPar.K.startBaseline)=[];
extPar.baseline(1:extPar.K.startBaseline)=[];
extPar.sigmaErr(extPar.K.emptybasedata)=[];
extPar.sigma(extPar.K.emptybasedata)=[];
extPar.baseline(extPar.K.emptybasedata)=[];

%-----

function TEMP=computePower(X1, extPar)

T=X1';
% X --> 1 column from the X matrix that Ferret receives.

Ti= repmat(T,extPar.K.NAnt,1);
Tj=Ti';
TEMP=zeros(1,extPar.K.NBase);
for n=extPar.K.NBase:-1:1;
    gNorm=(sum(sum(extPar.K.g(:, :, n))));
    if gNorm == 0
        TEMP(n)=0;
    else

```

5. APPENDIX

```
% Calculate the Variance
NoiseTemp=sqrt(sum(sum( extPar.K.g(:, :, n).*Ti.*Tj ))/gNorm^2);
TEMP(n)=NoiseTemp;

end

end

%-----

function F=fitness(X,extPar)

%--calculate the fitness of each generation
NSol=size(X,2);
for soln=NSol:-1:1
    X1=X(:,soln);
    TEMP=computePower(X1, extPar);
    F(soln)=(sum(((TEMP(:)-extPar.sigma(:)).^2./extPar.sigmaErr(:).^2)))...
        /(length(extPar.sigma)-length(X1));
    pause(0.001);
end

%-----

function makeImage(OptimalSolutions)

[FMin, index]=min(OptimalSolutions.F);
X=OptimalSolutions.X(:,index);
extPar=OptimalSolutions.par.user.extPar;
save(extPar.TempName, 'X');
TEMP=computePower(X,extPar);
%TEMP=extPar.sigma;
% Do facor of 2 stuff..
% write image.
```


5.1 System Temperature Derivation Code

```
baseline.a=(extPar.K.baseline/extPar.K.lambda)/extPar.K.dU;
baseline.b=baseline.a*sin(extPar.K.dec);
extPar.K.ang=linspace(0,pi/2,480/2);
NAng=length(extPar.K.ang);
grid.sigma=[];
TEMP_ALL=zeros(1,length(TEMP)+extPar.K.startBaseline);
TEMP_ALL(1,extPar.K.startBaseline:length(TEMP)+extPar.K.startBaseline-1)=TEMP;
for q=4:-1:1 % 4 quadrants
    grid.grid.UV_TEMP_quadrants{q}=zeros(extPar.K.NPix/2);
end
TEMP1=zeros(1,extPar.K.NVis/2*length(TEMP_ALL));
for b=1:length(TEMP_ALL);
    j=(b-1)*extPar.K.NVis/2+1;
    TEMP1(j:j+extPar.K.NVis/2-1)=TEMP_ALL(b);
    if ~isempty(TEMP1)
        ix=1./sqrt(1./baseline.a(b).^2+tan(extPar.K.ang).^2./baseline.b(b).^2);
        iy=ix.*tan(extPar.K.ang);
        i=max(1,ceil(ix));
        j=max(1,ceil(iy));
        for q=4:-1:1
            index=i+extPar.K.NPix/2*j;
% normalized sampling
            grid.grid.UV_TEMP_quadrants{q}(index)=TEMP_ALL(b)*ones(1,NAng);
        end
    end
end
end

grid.UV_TEMP=[[grid.grid.UV_TEMP_quadrants{1},fliplr(grid.grid.UV_TEMP_quadrants{2})];...
    flipud([grid.grid.UV_TEMP_quadrants{3},fliplr(grid.grid.UV_TEMP_quadrants{4})])];

N=complex(randn(extPar.K.NPix),randn(extPar.K.NPix))/sqrt(2);
grid.UV_TEMP=fftshift(grid.UV_TEMP.*N/extPar.K.Jy_per_beam_to_K);

% read in data
data=((fitsread(extPar.file.imgAll)))*1000;
UV_data=fftshift( ifft2(data')*extPar.K.NPix );
```

5. APPENDIX

```
IX=-extPar.K.NPix/2+0.5:extPar.K.NPix/2; IY=IX;
[IX,IY]=ndgrid(IX,IY);
R=sqrt(IX.^2+IY.^2);
RMax=min(extPar.K.NPix/2, extPar.K.NPix/2);

%--take a power spectrum
NRBins=round(RMax/4); % ARBITRARY.
REdges=linspace(0,RMax,NRBins+1);
dR=REdges(2)-REdges(1);
dist=(REdges(1:end-1)+dR/2)*extPar.K.dx;

PBase=[];
PBaseS=[];
for n=NRBins:-1:1
    index=R > REdges(n) & R < REdges(n+1);
    PBaseS(n)=std(grid.UV_TEMP(index));
    PBase(n)=std(UV_data(index));
end

spectra=figure(3); plot(dist,PBaseS);
hold on
plot(dist, PBase,'r')
hold off
xlabel('Baseline (meters)')
ylabel('Power (mJy)')
title(extPar.PlotTitle)
print(spectra, '-depsc', extPar.PlotSave)

%--Create a synthetic image
Temp_Image=fft2(grid.UV_TEMP);
save(extPar.ImageName,'Temp_Image');
```